POLITECNICO DI MILANO
Dipartimento di Elettronica, Informazione e Bioingegneria
Dottorato di Ricerca in Bioingegneria

Development of computational tools for the quantitative characterization of the mitral valve using three-dimensional ultrasound data

Ph.D. Dissertation of:
Miguel Sotaquirá

Tutor:
Prof. Sergio Cerutti

Advisor:
Prof. Enrico Caiani

The Chair of the Doctoral Program:
Proff.ssa. Maria Gabriella Signorini

2013 – Cycle XXV

Acknowledgments

I thank my advisor Enrico Caiani for his continuous guidance and support. During these three and a half years he has always been available and keen to discuss every aspect of my research; his involvement and interest on my work were always encouraging. Working with him allowed me to develop new skills that have shaped me as a researcher and scientist. Thanks again Enrico.

I'm also grateful to Dr. Mauro Pepi, Francesco Maffessanti, Laura Fusini and Gloria Tamborini at Centro Cardiologico Monzino, and to Dr. Roberto Lang, at University of Chicago Medical Center; they were always available to answer my questions and provide me with the data and feedback when it was necessary.

Finally, I would also thank my tutor Sergio Cerutti, for his scientific advice and knowledge that help me during my research.

Abstract

Valvular heart disease is a growing public health issue, and mitral valve (MV) disease is one of the most common disorders in the industrialized countries, with mitral regurgitation (MR) being one of the most common pathologies. To establish the severity of the disease, the quantification of the MV morphology and function is a key step in the clinical assessment of patients with MV disease. Conventionally, this assessment has been performed using ultrasound, in particular two-dimensional echocardiography.

The recent advent of three-dimensional echocardiography (3DE) potentially allows a more accurate and reliable assessment of MV disease. In spite of these developments, proper image processing and computational geometry methods are necessary to fully exploit the information contained in the 3DE ultrasound datasets, to allow the detailed morphological characterization of the MV and the quantitative assessment of patients with MR.

In this work, new computational tools for the detailed morphological characterization of the MV from 3DE datasets have been developed and validated with manual tracings. Moreover, their clinical applicability in terms of evaluation of patients with different pathologies has been preliminary explored. By applying novel image processing and computational geometry techniques, the developed algorithms allow a more repeatable and reliable quantitative assessment of the MV morphology, and at the same time they reduce the time required for user interaction. Their potential applicability to the evaluation of the tricuspid and aortic valves will also be discussed.

Contents

Chapter 1

Introduction

1.1 Motivation

Valvular heart disease, the damage or alteration in morphology and function of any of the four heart valves, is an important public health issue. Epidemiologic studies both in the United States and Europe[1], [2] show that more than one in eight patients aged 75 and older have moderate or severe valvular disease, a proportion that tends to increase with the projected shift to an older and larger population[1]. Differences between the prevalence of such diseases and the percentage of people effectively diagnosed (2.5% vs. 1.8%) have also been reported[1]; such studies stress the importance of early identification and quantification of severity, which in turn may lead to a better prognosis in these patients. The study of Nkomo et al. [1] also showed that in the observed population, mitral valve (MV) disease was the most common disorder, followed by aortic valve disease, with mitral regurgitation (MR) being a growing public health problem[3].

The clinical assessment of valvular diseases aims at delineating and quantifying the valves morphology and function to establish the severity of the pathology. To this aim, different imaging modalities (magnetic resonance, computer tomography and ultrasound) have been used in day to day practice. Among these modalities, computed tomography and magnetic resonance are the more appealing, but their clinical use in the assessment of valvular heart diseases remains limited owed to the constant motion of the beating heart and the reduced dimensions of the heart valves when compared with the available spatial resolutions. On the contrary, echocardiography, which uses ultrasound technology, is currently the most extended diagnostic tool used in clinical practice[4], owed to both its low cost and adequate temporal and spatial sub-millimeter resolutions, capable of imaging thin structures (such as the valves' leaflets) and following their dynamic changes during the cardiac cycle, thus allowing a thorough analysis of the valves morphology and function. Moreover, very recently the central role of valve morphology has emerged in clinical decision making in patients undergoing valve surgery. In fact, nowadays a large majority of patients with degenerative diseases and severe MR may undergo reconstructive procedures with different levels of complexity based on different degrees of MV morphologies. Thus new echo modalities (mainly three-dimensional) may facilitate the prediction of the complexity of such procedures (including the risk for MV replacement or the recurrence of regurgitation) and also facilitate the clinical decision and correct timing (early surgery vs. delayed procedures).

Conventionally, the assessment of the MV has been performed using 2-dimensional (2D) echocardiography (including Doppler) with standard 2D tomographic planes of the valve. However this approach is limited since it relies on careful adjustments of the probe position and mental integration of a limited number of 2D tomographic planes, which in turn requires a high degree of expertise[5], thus implying a low rate of reproducibility and reduced diagnostic accuracy. The relatively recent advent of three-dimensional echocardiography (3DE) has allowed to confirm that, instead of a planar configuration as previously thought, the mitral annulus (MA) exhibits a three-dimensional (3D) saddle shape[6]. In addition, 3DE has overcome many of the difficulties posed by 2D ultrasound imaging:

- Quantification of morphological parameters exhibits lower intra- and inter-observer variability[4] than 2D. The accurate quantification of parameters such as area, circumference and planarity index helps in the assessment of the MV and in the planning of repair strategies, as well as in the follow-up after surgery[7];
- The increasing quality of the images ensures a more realistic imaging of the valves and their corresponding anatomical and functional relationship with adjacent cardiac structures (i.e., the aortic valve[8]);
- Since a more realistic anatomic display of MV disease can be achieved, 3DE can be the modality of choice for guidance of percutaneous interventions[5];
- This accurate analysis of both the MV morphology and function, and of the severity of MV disease, allows an adequate planning and timing of MV repair if required, thus reducing the probability of postoperative left ventricular disfunction[5], in agreement with recent guidelines[9] for the management of patients with valve diseases;
- In intraoperative stages, 3DE can be useful for determining the suitability of customized prosthesis or the viability of repair strategies aimed at restoring the MV functionality[10];
- Advances in the miniaturization of electronic devices have also led to the development of new transesophageal echocardiographic probes, that when compared with the conventional transthoracic approach, allow a higher spatial resolution thus allowing a more detailed characterization of the morphology of the valves[4], [7], [11]. The successful use of novel transnasal probes recently reported[12] is an example of these advances, and has the potential of changing the current imaging practice in clinical settings.

Although not as extended as the MV studies, recent attention has also been devoted to the quantification of morphology and function of the aortic and tricuspid valves[13-19]. A growing interest in the incorporation of 3DE in clinical practice for the assessment of these valves can be expected, as well as improvements both in hardware and custom made software to allow a more objective and quantitative evaluation of their anatomy and function, thus reducing the subjectivity in the interpretation of the images.

The continuous advances in 3D ultrasound transducer technology and the increasing amount of available data has also lead to the development of custom and commercial computational tools for off-line quantification of the MV and aortic valves[8], [20-34]. Although many of these packages allow manual or user-guided tracing and measurement of MA and mitral leaflets (ML) geometric parameters, many of these approaches are still time consuming, which limits their applicability in clinical settings. In addition, none of the existing approaches fully exploits the available information present in the 3DE datasets, such as regional characterization of leaflets morphology, thus limiting the quantitative assessment of MV to only global parameters that may not depict a complete picture of the MV pathophysiological condition.

The availability of such regional information could have the potential to improve diagnosis and follow-up of patients with MV disease, as well as of giving additional insights into the structural changes and remodeling undergoing in the diseased MV or after surgical procedures. These aspects have been already pointed out by 2D and 3D ultrasound studies, together with biochemical and histological findings of the ML in patients with different pathologies[31], [35-47].

Mitral regurgitation is the most common MV disease[1] and, as stated previously, 2D and 3D ultrasound and Doppler echochardiography are the modalities of choice for the assessment of such patients. In particular 2D and 3D Color Doppler echocardiography allow the visualization of the regurgitant flow, as well as the quantification of the

effective regurgitant orifice area (EROA) and the vena contracta (VC) diameter, which provide crucial information about mitral regurgitation severity[3].

Several studies[48-50] aiming at testing the reproducibility of such measures have concluded that these parameters have a low level of inter-observer agreement, and consequently are modestly reliable[48]. This fact makes difficult the distinction between severe and non severe mitral regurgitation.

Although a few semi-automatic approaches have been suggested for computing the anatomical regurgitant orifice area from 3DE and 3D Color Doppler datasets[51], [52],[53], they still rely on heavy user interaction, custom-made hardware or careful setting of acquisition parameters to ensure an accurate quantification of the regurgitant orifice geometry.

In current clinical practice, the estimation of VC and EROA parameters is still highly user dependent, and common pitfalls in its quantification are:

- The VC diameter is a 1-dimensional measure of a 3D structure, besides it is obtained from 2D Color Doppler echocardiographic images, and thus it is highly dependent on the location of the corresponding cut-plane during acquisition. In fact, it has been demonstrated that this approach under- or over-estimates the anatomical orifice size given its non circumferential shape[1].
- The computation of the EROA relies in the proximal isosurface velocity area method which is based on the assumption that the regurgitant orifice has a circumferential geometry, a strong assumption that do not hold on most of the cases[7], [50], [54].

The inaccurate nature of these measurements may affect the diagnosis and course of treatment in patients with mitral regurgitation; a more precise delineation of the 3D shape of both VC and the regurgitant orifice, by exploiting the available information in the 3DE datasets, may lead to a more accurate assessment of these patients.

1.2 Aims and outline of the work

This work addresses the problem of quantitative characterization of the MV by fully exploiting the information contained in 3DE datasets. The aim is to provide a set of computational tools, based on image processing and computational geometry techniques, capable of providing a more accurate and repeatable assessment of MV disease, and at the same time reducing time-consuming user interaction.

In particular, the proposed methods focus on two of the issues introduced in the previous section: the detailed morphological characterization of the MV both in normal and diseased valves, as well as a novel method for the quantitative assessment of patients with MR. In both cases, systolic frames from the 3DE datasets have been used, since it is during this phase of the cardiac cycle that the MV is subject to the highest ventricular pressure, and also because it allows the visualization of ML malcoaptation in patients with MR. In addition, the application of the proposed methodologies for the assessment of diseased aortic and tricuspid valves will be also explored.

The thesis is organized as follows:

- In Chapter 2, a brief overview of the anatomy of the heart valves is presented, followed by current clinical approaches for the assessment of valve disease, giving particular emphasis to the MV and to patients with MR. Next, a description of advanced concepts of image processing and computational geometry is given, which lays the framework for understanding the implemented algorithms. In particular, a brief explanation of block matching, graph theory, mathematical morphology, graph-based segmentation

algorithms, marching cubes and surface mesh shape and curvature descriptors is included in this section.

- In Chapter 3 a new semi-automated algorithm for the segmentation and quantification of MA and ML is described. First, a revision of the literature related with the implementation of semi-automatic procedures for the segmentation and quantification of MA and ML is presented, stressing on each case its contributions, advantages and current limitations. Next, the different methodological approaches considered are described and compared, followed by the detailed description of the new segmentation and quantification tool.
- Chapter 4 presents the validations results of the semi-automated algorithm for the segmentation and quantification of MA and ML. The algorithm was tested both in normal and diseased human populations as well as in porcine specimens. Results are presented in terms of accuracy and repeatability of the method, followed by a thorough discussion of the results and a comparison with existing approaches.
- In Chapter 5, two clinical applications of the developed algorithms, described in Chapter 3, are presented. These applications are focused on the regional characterization of the ML surface, and were tested on patients with different diseases as well as in patients who underwent MV repair with annuloplasty. The chapter ends with the discussion of the clinical implications of these findings.
- Chapter 6 presents a new algorithm for the semi-automatic detection and quantification of the anatomic regurgitant orifice in patients with MR. Current existent methods are first discussed, followed by the preliminary solutions considered. Finally, the implementation of the proposed algorithm, that makes use of both image processing and computational geometry methods, is described in detail.
- In Chapter 7, the validation of the algorithm for the segmentation and quantification of the regurgitant orifice is presented. This validation was carried on by performing comparisons with 2D planimetry of the orifice, performed by an expert. These results, as well as the discussion and comparison with other approaches, stressing the advantages of the new proposed methodology, are also presented in this chapter.
- In Chapter 8 the applicability of the methods described in chapters 3 and 6 is explored for the characterization of diseased tricuspid and aortic valves. In particular, the feasibility of the semi-automated quantitative assessment of the tricuspid and aortic valves is discussed in light of the algorithms described in chapters 3 and 6 for the segmentation and quantification of the MA, ML and of the regurgitant orifice. In addition, a discussion regarding the use of the MA and ML segmentation algorithm for the dynamic analysis of the MV is presented.
- Finally, in Chapter 9 the original contributions brought by this work are summarized, along with some concluding remarks.

Chapter 2

Background

In the following sections much of the emphasis will be given to the MV, the core of this work. When necessary, references to other valves will be briefly mentioned.

2.1 Basic concepts of anatomy and physiology

2.1.1 The chambers of the heart and the cardiac cycle

The heart has four hollow chambers: two superior (left and right) atria and two inferior (also left and right) ventricles. Blood flow to and from heart cavities is controlled by the four heart valves: the mitral and tricuspid (atrio-ventricular) valves and the pulmonary and aortic (semilunar) valves. The first two control blood flow from the atria to the ventricles, whereas the semilunar valves control the blood flow from the heart cavities to the arteries (Fig. 2.1).

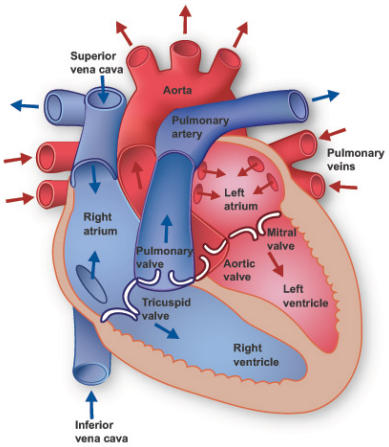

Figure 2.1. Internal anatomy of the heart displaying the four cavities as well as the atrio-ventricular (mitral and tricuspid) and semilunar (pulmonary and aortic) valves. Arrows depict the direction of blood flow. (Image taken from: http://www.texasheartinstitute.org/HIC/Anatomy/anatomy2.cfm)

A single cycle (one heartbeat) of cardiac activity comprises four main stages:

i. *Ventricular filling:* during this stage both mitral and tricuspid valves are open, whereas the semilunar valves are closed, thus ensuring ventricular filling as a result of atrial musculature contraction.
ii. *Isovolumetric contraction:* in this stage the atrio-ventricular valves start closing and the semilunar valves begin opening, with the ventricular pressure rapidly changing. Ventricular volume remains the same during this phase (i.e. there is no ejection) and the ventricular contraction also triggers the contraction of the papillary muscles attached to the chordae tendinae of the atrio-ventricular valves, thus ensuring their correct closure. When valves are leaky, or don't close properly, there is a backflow of blood known as regurgitation.

iii. *Ejection phase:* the ventricles experiment contraction and the aortic and pulmonary valves are open, whereas at the same time the mitral and tricuspid valves remain closed thus ensuring a period of atrial filling.
iv. *Isovolumetric relaxation:* aortic and pulmonary valves abruptly close as the result of the reduction in intraventricular pressures. Thus, with all valves closed, ventricular volumes remain constant.

2.1.2 The mitral valve: anatomy and function

The MV is located on the left side of the heart and prevents systolic backflow from the left ventricle to the left atrium. This MV complex is composed by the mitral annulus (MA), the mitral leaflets (ML) the chordae tendinae and the papillary muscles.

The MA is a fibroelastic ring with a 3D saddle shape to which the anterior and posterior ML attach[55]; the dynamic structure of the MA requires 3D deformation during the cardiac cycle, thus experiencing changes in circumference, excursion, curvature, shape and size, which in turn makes it susceptible to ventricular remodeling[56].

The geometry of the MA can be divided into two zones: the anterior portion (a fibrous region of continuity with the aortic root, in the vicinity of the aortic valve) and the posterior portion (which has a larger perimeter than the anterior) (Fig. 2.2, left). In this work two additional regions will also be mentioned: the Antero-lateral (located near the anterior commissure, Fig. 2.2, right) and the Postero-medial (located near the posterior commissure, Fig. 2.2, right).

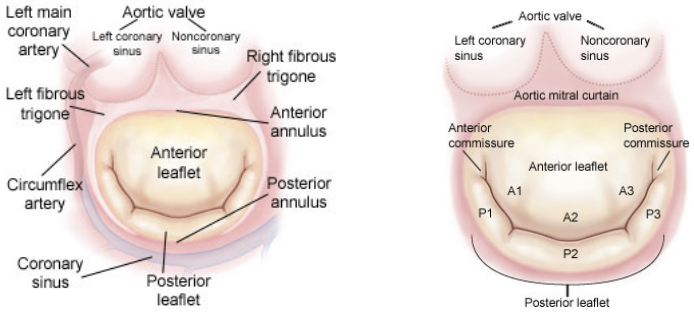

Figure 2.2. Illustration of the atrial surgical view of the mitral valve. Left: the mitral annulus and the anterior and posterior leaflets; Right: standard nomenclature for each segment/scallop in the mitral leaflets (image taken from http://www.mitralvalverepair.org)

The MV has two leaflets, namely anterior and posterior (Fig. 2.2). The first has a semi-circular shape and is attached to approximately two-fifths of the annular circumference; the second has a quadrangular shape and is attached to approximately three-fifths of the annular circumference[57]. Each leaflet presents a series of segments, leading to the standard nomenclature for the A1 (anterior), A2 (middle) and A3 (posterior) segments and an analogous set of scallops (P1, P2, P3) for the posterior leaflet (Fig. 2.2, right).

The remaining structures in the subvalvular apparatus are the two papillary muscles, originating from the left ventricular wall in the apical region, and the chordae tendinae, attached on one end to the papillary muscles and on the other to the ventricular surface of the anterior and posterior ML[55]. Both structures determine the position and tension of each leaflet at end-systole.

During MV closure, apposition of both anterior and posterior ML results in a zone of coaptation or "coaptation line"; the quantification of the height and length of this line is of diagnostic importance for the assessment of normalization of valve's morphology and dynamics after annuloplasty procedures[7].

2.1.3 The tricuspid valve: anatomy and function

The tricuspid valve (Fig. 2.3) is located on the right side of the heart and allows blood flow from the right atrium to the right ventricle. Its complex is composed by the tricuspid annulus, leaflet tissue, papillary muscles and chordae tendinae. The tricuspid annulus is a nonplanar structure with a saddle-shaped pattern[17]; three leaflets compose this valve: the anterior leaflet (being the largest and most mobile of the three leaflets) with a semi-circular shape, the septal leaflet (the least mobile) with a semi-oval shape and the posterior leaflet (the smallest one) with a variable shape[19]. As with the MV, the chordae tendinae are attached on one end to the papillary muscles and on the other to the ventricular leaflet surface, and ensure proper closure of the leaflets at end-systole.

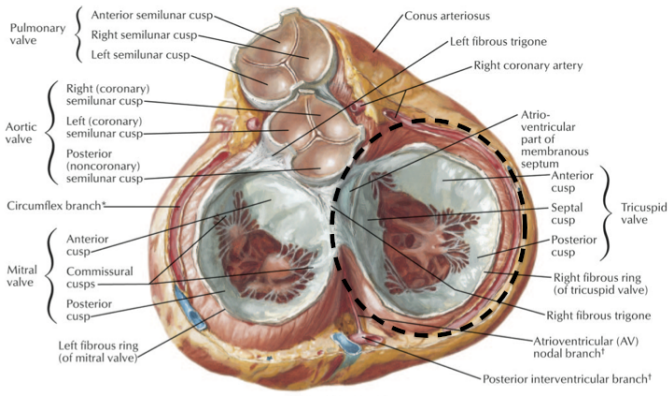

Figure 2.3. Illustration representing the position and anatomy of the tricuspid valve (black dashed contour) (image taken from: http://www.netterimages.com)

2.1.4 Aortic and pulmonary valves: anatomy and function

These valves separate the ventricles from the aorta and the pulmonary artery, respectively. As with the atrio-ventricular valves, they exhibit a passive mechanism of opening and closure, controlled by the pressure differences between the left ventricle and the aorta (in the case of the aortic valve) or between the right ventricle and the pulmonary artery (in the case of the pulmonary valve).

The aortic valve is part of the aortic valve complex (Fig. 2.4, left)[58], [59], composed by the sinuses of Valsalva, the interleaflet triangles and three valvular leaflets, the latter originating from the supporting left ventricular structures, which makes difficult the definition of an aortic "annulus" since there is not such discrete anatomic structure[59]. However, a practical surgical definition of the aortic valve annulus is the semi-lunar crown-like structure delimited by the hinges of the leaflets.

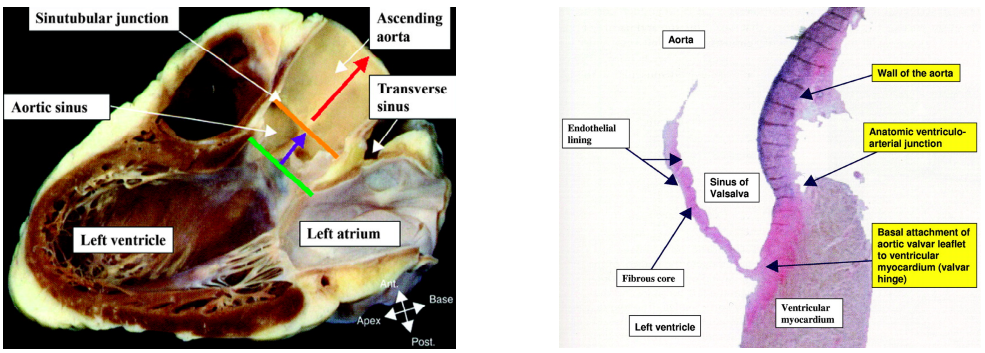

Fig. 2.4. Left: the aortic valve (in the middle of the green and orange bars) as part of the aortic valve complex; right: histology image of the aortic root complex (notice that the leaflet attachment and the ventricular myocardium form a continuous structure) (with permission from Piazza et al.,[59])

The pulmonary valve exhibits an anatomy similar to that of the aortic valve. In this case, the valve lies within the pulmonary root, which in turn is part of the right ventricular outflow to which the three valve's leaflets are attached (Fig. 2.5, left). In addition to these valvular leaflets, the pulmonary root is composed of the sinuses of Valsalva and the interleaflet triangles[7]. Also as with the aortic valve, there is no presence of an annulus since the attachment points of the leaflets and the pulmonary root form a continuum.

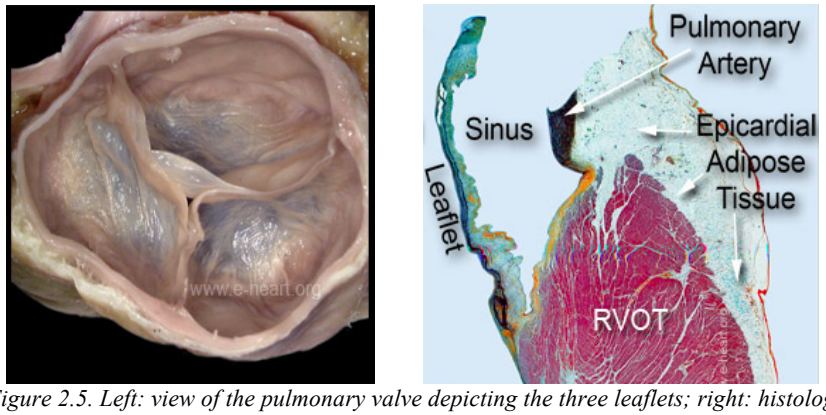

Figure 2.5. Left: view of the pulmonary valve depicting the three leaflets; right: histology image of the right ventricular outflow complex (notice the similar constitution of the tissue near the attachment of the leaflet) (image taken from: http:// http://www.e-heart.org)

2.2 Imaging of the mitral valve using ultrasound

Echocardiography is currently the imaging modality of choice for the assessment of patients with valvular disease[60]. Given the dynamic nature of the heart as well as the reduced dimensions of the valvular structures (of the order of a few millimeters or in the sub-millimeter range), with imaging modalities such as cardiac magnetic resonance or computer tomography it is not possible to achieve the required spatial and temporal resolutions available in ultrasound systems, thus limiting the application of such techniques for the adequate assessment of the valves.

Conventionally, the assessment of the MV has been performed with 2D transthoracic echochardiography; however diagnosis with this modality is limited since the leaflet-annular relationship of the 3D MV structure cannot be easily interpreted from 2D tomographic views[7]. In addition, poor acoustic windows affect the quality of this imaging modality and limit the possibility of extracting reliable morphological and functional parameters. Furthermore 2D measurements exhibit a relatively high inter- and intra-observer variability, making this modality highly user dependent[4].

On the contrary, the recent development of 3D transesophageal echocardiography (3DTEE) probes offers higher spatial resolution than that obtained using current 3D transthoracic echocardiography (3DTTE) probes, and allows the detailed evaluation of the valve morphology[61]. This modality is now emerging as the best tool to assess the MV, providing views similar to what a surgeon would see in the operating room[4], thus allowing a more comprehensive assessment of the diseased MV. In MV with prolapse and in presence of regurgitation, the topography and size of the prolapsed tissue can be measured and direct imaging of the regurgitant orifice is possible[60](Fig. 2.6).

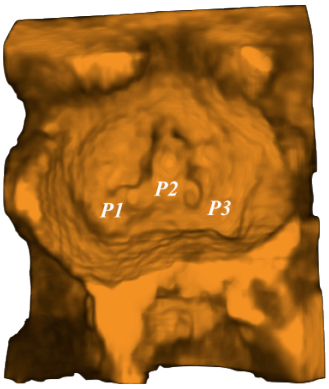

Figure 2.6. A rendered view, from the atrial side, of a mitral valve with a prolapsed P2 scallop.

It is expected that advances in technology and miniaturization will allow larger scanning volumes in 3DTEE probes, as well as higher spatial (currently of the order of 0.3 mm) and temporal resolutions, thus increasing the possibility of more sophisticated methods of quantification of the valvular complex.

2.3 Mitral valve disease

There are two main conditions that affect the MV: mitral stenosis and MR. Mitral stenosis is an obstruction of the left-ventricular inflow at the level of the MV as a result of a structural abnormality of the MV apparatus, which prevents proper opening of the valve during diastole[9]. It is the less common MV disease, with a prevalence of 1% in developed countries[1]. In patients with mild degree of stenosis, medical management is the preferred treatment option, with avoidance of physical stress being the preferred choice in presence of atrial fibrillation; however, in symptomatic patients with moderate to severe mitral stenosis, percutaneous mitral balloon valvotomy (the valve is dilated using an expandable balloon) is the most common procedure[9].

The second condition that affects the MV is the MR, the more frequent MV disease, and one of the most prevalent valvular diseases in developed countries[2], [9]. It is defined as a systolic retrograde flow from the left ventricle into the left atrium[3].

The causes of MR can be organic (resulting from valve lesions) or functional (resulting from remodeling of the left ventricle which deforms a structurally normal MV)[3]. The most common cause of organic MR is the MV prolapse, defined as an abnormal systolic valve movement into the left atrium (≥2 mm beyond the saddle-shaped annular level)[6].

Two-dimensional color Doppler echocardiography is the imaging technique of choice for the assessment of patients with MR, since it allows the visualization of the MV apparatus and of the regurgitant jet (Fig. 2.7) from which several parameters can be quantified.

In particular:

i. The diameter of the cross-section of the vena contracta (VC), defined as the narrowest portion of the regurgitant jet (Fig. 2.7). Although it actually corresponds to a 3D surface, current guidelines[62] use the width of the VC (measured from 2D Color Doppler acquisitions) as one of the parameters that define severity of MR;
ii. The effective regurgitant orifice area (EROA) which is a 2D indirect measure of the actual size of the regurgitant orifice. The estimation of the EROA is based on the proximal isovelocity surface area (PISA) method, which assumes that the regurgitant blood flow converges in a hemispherical shape. By

estimating the radius of this hemisphere and applying the continuity equation, it is possible to estimate the EROA from 2D color Doppler acquisitions using the equation:

$$EROA = 2\pi r_{hem}^2 \frac{V_r}{V_0} \quad [cm^2] \tag{2.1}$$

where r_{hem} is the estimated radius of the hemisphere, V_r is the velocity of the regurgitant flow at a distance r_{hem} from the orifice, and V_o is the flow velocity at the orifice, all measurements obtained directly from the acquired Doppler images. Along with the VC, the EROA is another measure currently used in the assessment of mitral regurgitation severity[3], [62];

iii. The regurgitant volume (in ml), corresponding to the estimated backflow volume from the left ventricle to the left atrium. This method also relies in 2D color Doppler acquisitions and depends on the previous estimation of the EROA.

The main drawback of the current approaches for the estimation of VC and EROA is the assumption that the anatomical regurgitant orifice has a circular cross-section, an assumption that is not valid in many patients with MR. Currently, 3D color Doppler and 3D PISA methods have been proposed[50], [63], [64], however the application of these approaches involves a prolonged user interaction, as well as a careful setting of system parameters during acquisition, which limits their clinical acceptance[4].

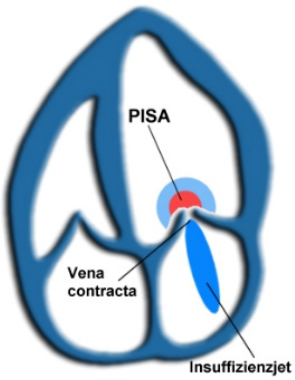

Figure 2.7. Illustration of a regurgitant jet flowing from the left ventricle (on top) to the left atrium (bottom). The vena contracta corresponds to the narrowest portion of the jet, whereas in red is depicted the proximal isosurface area (an hemispherical shape is assumed) (image taken from: http:// http://www.echobasics.de)

Surgical valve repair is the only treatment with defined clinical success[3]. This approach encompasses several valvular, subvalvular and annular procedures aimed at eliminating MR by restoring leaflets coaptation. Typical repair procedures in MV prolapse include resection of the prolapsed leaflet areas and implantation of annuloplasty rings.

2.4 Advanced concepts of image processing and computational geometry

This section gives a brief introduction to essential advanced concepts in the image processing and computational geometry fields. The new methods for the

quantification of MA, ML and MR (described in the next chapters) make use of the techniques that will be described in the following sections.

2.4.1 Block matching

This technique determines the relative displacement of a point in a sequence of images. Let *R* and *T* denote the reference and target 2D images, respectively, where the point to be tracked is initially selected in the *R* image. Let *f(x,y)* be a region-of-interest (ROI) selected from *R* and centered at the point of interest, and *t(x,y)* be a region of search located within the *T* image and larger than *f(x,y)*. The similarity of gray patterns between the *f(x,y)* and *t(x,y)* images can be measured using the weighted normalized cross-correlation (WNCC), defined as:

$$WNCC(u,v) = \frac{\sum_{x\in N}\sum_{y\in M}\left[(f(x,y)-\bar{f}).W(x,y)\right]\left[(t(x-u,y-v)-\bar{t}\right]W(x,y)}{\sqrt{\sum_{j\in N}\sum_{i\in M}\left[(f(x,y)-\bar{f}).W(x,y)\right]^2\sum_{j\in N}\sum_{i\in M}\left[\left[(t(x-u,y-v)-\bar{t}\right].W(x,y)\right]^2}} \quad (2.2)$$

where $\bar{f}$ and $\bar{t}$ denote the mean values of *f(x,y)* and *t(x,y)* and *W(x,y)* is a weighting kernel that gives high relevance to central pixels.

The displacement of the point between the *R* and *T* images can then be estimated by searching for the global maximum in the WNCC image. The use of the weighted normalized cross-correlation has the advantage of being insensitive to local variations in the mean and standard deviation of the image gray level[65].

2.4.2 Graphs

A graph *G=(V,E)* is a general structure consisting of a set of nodes *V* and a set of edges *E* between connective pairs of nodes, usually having a cost (i.e., being numerically weighted). In addition, graphs can be directed or undirected: in the first case the edges have an associated direction, whereas in the second the edges don't have orientation. Usually in directed graphs, the cost of the edge between nodes *p* and *q* differs from that of the reverse edge *p, q*. Fig. 2.8 illustrates an example of a directed graph.

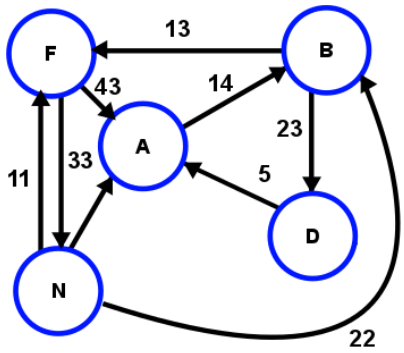

Figure 2.8. A directed graph with 5 nodes (A, B, D, F, N) and 9 directed edges. Notice that the cost of the edge F,N is different from that of the edge N,F. (image taken from http://commons.wikimedia.org)

2.4.3 Minimum-cost paths on graphs

Two optimal graph path search algorithms, applied to images, are used in this work: the computation of optimal paths using dynamic programming[66] and the shortest path Dijkstra algorithm[67].

Dynamic programming allows the computation of a global optimal path in a graph. To do so, the algorithm sweeps the *N-layers* graph from layer *0* to layer *N-1* and on each iteration[68]:

- it computes the minimum cumulative cost of going from layer *i* to each node in layer *i+1* ($0 \leq i \leq N-2$);
- it then stores the value of this minimum cost and the id of the node in layer *i* from which this cost was obtained.

The optimal path is then found by back-tracking from layer *N-1* to layer *0* and on each step following the path traced by the minimum cumulative costs.

The algorithm is exemplified in the Fig. 2.9: in Fig. 2.9(a), a directed graph consisting of nine nodes (labeled from *A* to *I*), 14 edges and three layers is depicted. The goal is to find the global optimal path, with the minimum cost, that connects *layer 0* with *layer 2*. Each iteration of the algorithm is described below:

- *Iteration 1* (Fig. 2.9b): the minimum cost path for arriving to node *D* is from node *B* and the corresponding cumulative cost is 2 (this information is displayed in blue above the corresponding node). In the same way, the paths *A-E* and *B-F*, with cumulative costs 2 and 1, represent the minimum cost paths for arriving to nodes *E* and *F*.
- *Iteration 2* (Fig. 2.9c): the pairs of paths and minimum costs of going from *layer 1* to *layer 2* are: *D-G* (cumulative cost = 7); *F-H* (cumulative cost = 3); *E-I* (cumulative cost = 7).
- *Iteration 3* (Fig. 2.9d): back-tracking is performed in this step. The node *H* represents the end of the path with the minimum cumulative cost; following the corresponding path traced in previous iterations, it can be observed that the path with the minimum cost that connects *layer 0* with *layer 2* is given by *B-F-H*.

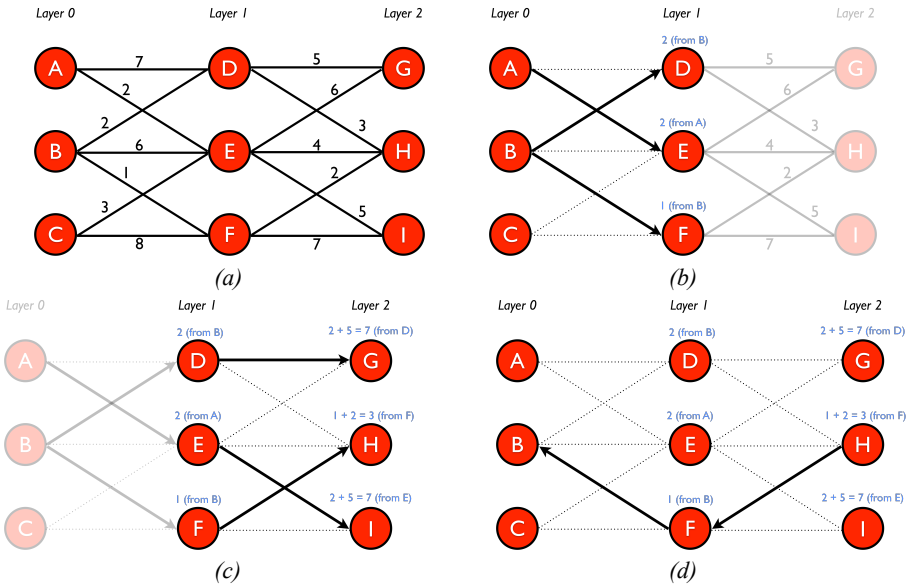

Figure 2.9. An example of dynamic programming. (a) A graph with 9 nodes (in red) and 14 edges is shown; edge costs are displayed in black; (b) First iteration of the algorithm, the corresponding cumulative cost and node ids are displayed in blue, the partial paths are displayed with arrow lines; (c) Second iteration of the algorithm: again, partial paths are displayed with arrow lines; (d) Back-tracking of computed cumulative weights and paths allows the computation of the global minimum cost path (B-F-H)

Dijkstra's algorithm solves a similar problem, but instead of finding a global path it computes a local minimum cost path from a particular "source" node in the graph to each of its remaining nodes; for this reason, the algorithm is also known as the solution to

the one-to-all shortest path problem. The inputs to the algorithm are the graph *G*, with each edge having a weight *w(e)*, and a source node *s*. For a target node *t*, which can be any node in the graph, the algorithm operates in a similar manner to the dynamic programming approach: starting at node *s* the algorithm iterates through its neighbors and on each case computes and stores both the cumulative cost and the id of the node with the minimum cost; the process is repeated until the algorithm reaches the target node *t* thus obtaining a connected path from *s* to *t* with minimum costs.

2.4.4 Max-flow/min-cut algorithm

These algorithms work on directed weighted graphs with nodes *V*, edges *E* and edge weights *w(p,q)*. In addition, in this type of configuration two different nodes are present: the source, *s*, and the sink, *t*, nodes. Under this configuration the directed edges lead from the source to the sink node (Fig. 2.10).

It is possible to think of this type of graph as a network of pipes conducting water: edges are pipes, edge weights, or capacities, measure the pipe capacity to transport water (the higher the capacity the greater the amount of water that flows through the pipe) and nodes are the pipe junctions. In the maximum flow problem the goal is to solve the question: *what is the maximum amount of water one can send from source to sink through the pipe network without violating any capacity constraints?*[69] Equivalently, put in graph theory terms, the question to be solved is: *what is the maximum flow between nodes s and t through the graph G=(V,E)?*

The method of Ford and Fulkerson[70] solves this problem: starting with flow values equal to zero for all edges in the graph, the algorithm iteratively modify (increases or decreases) these values until the flow from *s* to *t* reaches a maximum. Ford and Fulkerson also noticed that when this maximum-flow condition is achieved, a set of edges in the graph becomes saturated, and that this set of edges divides the nodes in the graph into two disjoint parts[71]. This set of edges is known as the *minimum-cut*, since the sum of weights of edges going from *s* to *t* through the cut is the minimum of all possible cuts in the graph.

The concepts of flow, maximum flow, cuts and minimum-cut are depicted in Fig. 2.10(b). In this figure, flows on edges are in blue whereas flow capacities are in black; in addition the expressed values were obtained after applying the max-flow/min-cut algorithm.

As seen from Fig. 2.10(b), the maximum flow is the sum of the flows of the edges leaving *s* (the edges *s-1* and *s-2* in the figure); in this particular case the maximum flow equals 15+0 = 15. In addition, several cuts are depicted (from 1 to 4) and the minimum cut is drawn with the continuous green line. Notice for example the cost of the cuts 1 to 4:

- Cut 1: 20 (edge *s-1*) + 10 (edge *s-2*) = 30
- Cut 2: 15 (edge *3-t*) + 20 (edge *4-t*) = 35
- Cut 3: 10 (edge *s-2*) + 5 (edge *1-3*) + 10 (edge *1-2*) = 25
- Cut 4: 15 (edge *3-t*) + 10 (edge *2-4*) + 10 (edge *4-3*) = 35
- Min-cut: 5 (edge *1-3*) + 10 (edge *2-4*) = 15. Notice that only edges pointing in the *s-t* direction are included in the computation

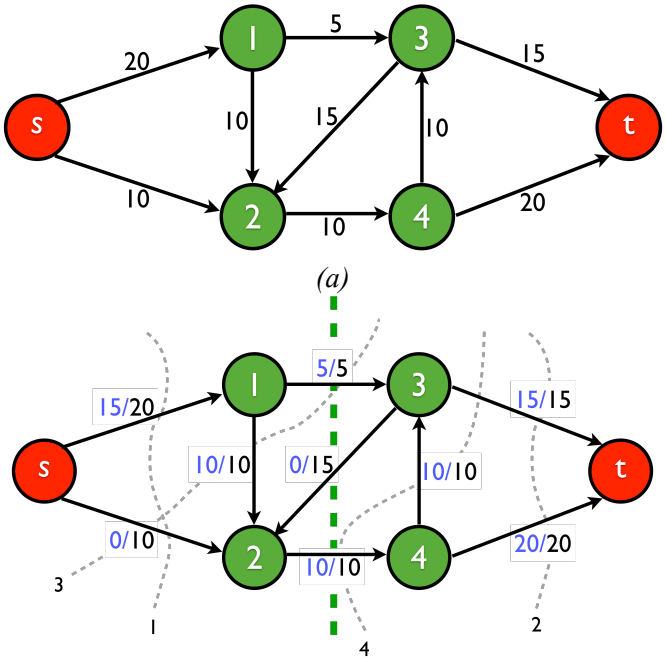

(a)

(b)

Figure 2.10. (a) A directed graph, with 4 nodes, one source node "s" and one sink node "t". Edge capacities (weights) are displayed in black. (b)Results after computation of maxflow/mincut algorithm; flow values are displayed in blue, whereas the minimum cut is the green dashed line. Several cuts (from 1 to 4) are also displayed.

As mentioned previously, the computation of the min-cut from the maxflow/mincut algorithm allows obtaining a set of edges that divides the graph in two disjoint regions. This result is useful in the image processing and computational geometry contexts, since it can be seen as a way of segmenting an image/a mesh into two different labeled regions, where the frontier or interface between both of them corresponds to the min-cut (Fig. 2.11).

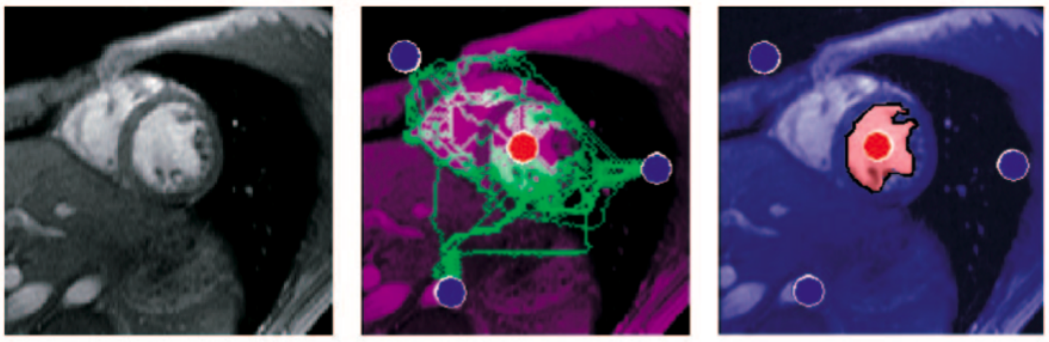

(a) *(b)* *(c)*

Figure 2.11. Example of the maxflow/mincut algorithm applied to the segmentation of a short-axis image of the left ventricle. (a) the original gray-scale image; (b) three source nodes (in blue) and one sink node (in red) are selected on the image; the green lines depict the maximum flows from source to target nodes; (c) the mincut, black contour, corresponding to the set of edges saturated by the maximum flows in (b). (image taken from Boykov et al. [71]*)*

2.4.5 Active contours

The region competition method is an active contour algorithm proposed by Zhu and Yuille[72] that combines aspects of snakes, balloons and region growing. This method allows the segmentation of 2D and 3D images where the structure of interest has

noisy edges but relatively homogeneous and well-defined intensity distributions when compared with the background, a typical characteristic of ultrasound images[23], [73].

The active contour is a 2D or 3D parametric surface *S(**r**;t)* depending on the spatial parameter **r** and time *t*. The contour evolves according to the equation[73]:

$$\frac{\partial}{\partial t} S(\mathbf{r};t) = F \frac{\nabla S(\mathbf{r};t)}{\|\nabla S(\mathbf{r};t\|} \qquad (2.3)$$

where $\nabla S(\mathbf{r};t)$ is the spatial gradient of the surface, $\nabla S(\mathbf{r};t)/\|\nabla S(\mathbf{r};t\|$ is the unit normal to the surface and F is the sum of internal an external forces acting on the contour. The internal force is defined by the mean curvature of the surface, whereas the external force is controlled by image features:

$$F = \alpha(P_{obj} - P_{bkg}) + \beta k \qquad (2.4)$$

where P_{obj} and P_{bkg} denote the probability of a pixel of belonging to the foreground or the background and $k = div\left(\nabla S(\mathbf{r};t)/|\nabla S(\mathbf{r};t)|\right)$ is the mean curvature of the surface, and α and β are user defined parameters to balance each component in Eq. 2.4. The equation is solved using the level set method proposed by Osher and Sethian [74] and it has the advantage over threshold-based or region growing-based methods of generating smooth 3D contours representing the segmented structure.

2.4.6 Isosurfaces, polygonal meshes and the marching cubes algorithm

In this section, a general introduction to the algorithms involved in the generation of 3D models from medical images is given. In this context, it is useful to define a 3D grayscale image *I(x,y,z;g)* as a function of 4 variables: the 3D spatial coordinates *x,y,z* and the intensity level *g* at each point in space.

An *isosurface* is defined as the 3D surface representing voxels in the image with the same intensity level. In terms of the previous image notation this is equivalent to $I(x,y,z;g_0)$ where g_0 is the particular intensity level at which the isosurface is computed. An example of an isosurface is given in Fig. 2.12.

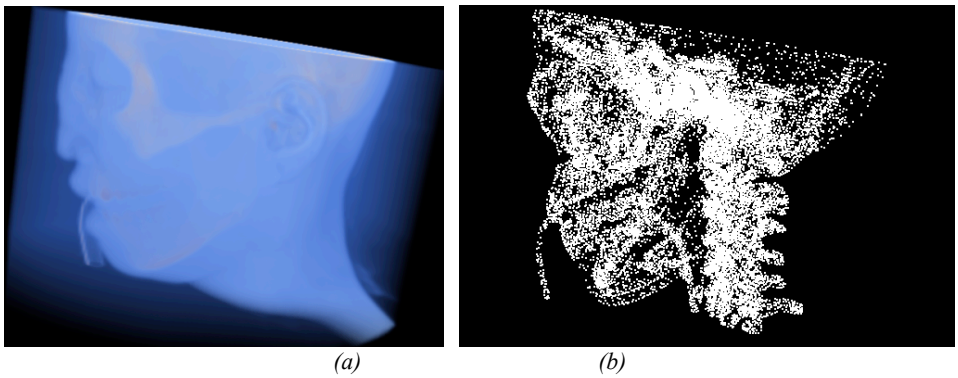

(a) *(b)*

Figure 2.12. (a) Volume rendering of a 3D computer tomography scan of a human head; (b) 3D point cloud obtained by extracting the voxels in (a) with an intensity level equal to 2000

The result depicted in Fig. 2.12(b) seems to correspond to the osseous tissue of Fig. 2.12(a). However, the representation is not clear since the computed isosurface is actually a collection of 3D points in space, instead of a 3D surface. This set of points is not connected and thus it makes difficult the interpretation of the results.

It becomes evident that to gain understanding of the anatomy represented by the set of extracted points, some additional processing aimed at "connecting" these points is

necessary. In other words, we want to obtain a 3D model representation of the anatomical structure. In the context of computational geometry, the terms 3D surface or 3D model are best known as *polygonal mesh representation*. A polygonal mesh is a collection of connected polygons that form the 3D surface of the object. Usually, in medical applications these polygons are triangles, which in turn are formed by edges and vertices. Fig. 2.13(a) illustrates a 3D polygonal (triangular) mesh representation of the point cloud in Fig. 2.12(b).

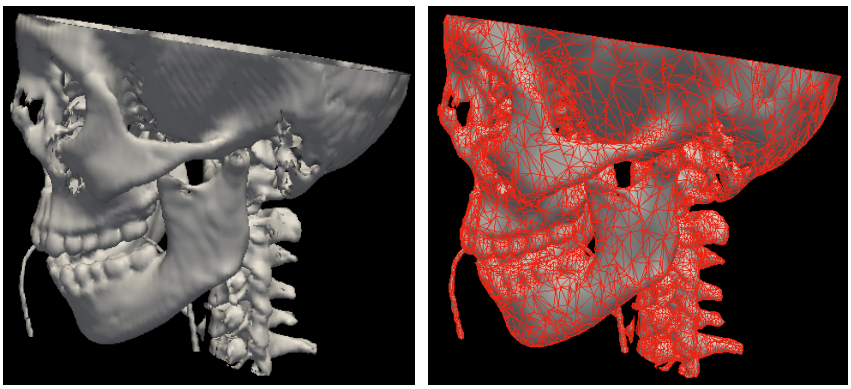

(a) *(b)*

Figure 2.13. Polygonal mesh representation, or 3D model, of the isosurface in Fig. 2.12(b). In (b) the triangles defining the 3D model are displayed.

The most extended approach for obtaining polygonal meshes from isosurfaces is the *marching cubes* algorithm[75], which allows the computation of a set of connected triangles representing the isosurface. Based on the isovalue g_0, the algorithm first labels the voxels in the original grayscale image as being *above* or *below* if their intensity value is higher or lower than g_0. It then creates a *marching cube* from eight pixels taken from two adjacent slices in the image:

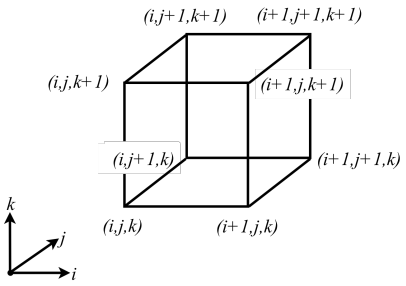

Figure 2.14. A marching cube defined from a set of 8 adjacent voxels in the image located at slices k and k+1.

The algorithm determines how the *isosurface* intersects this cube, constructs a triangle of the mesh representing this boundary, and then moves (or marches) to the next cube. To determine the intersections, the algorithm first determines which voxels in the cube are *above* and which *below* and then constructs a triangle, or a strip of triangles, with a topology with voxels *above* lying on one side of the surface and voxels *below* lying on the other side. To do so the algorithm uses an indexation scheme for vertices and edges in the *marching cube*:

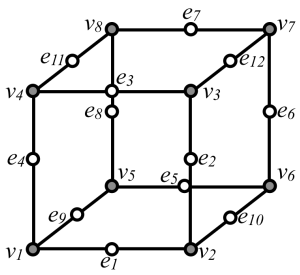

Figure 2.15. Indexation of vertices and edges in the marching cube.

For example, referring to Fig. 2.15, if the label of v_1 is *above* and all the remaining vertices are *below*, then a triangle with vertices along e_1, e_4 and e_9 must be constructed. The actual location of each triangle vertex along the edges is determined by linear interpolation, and thus the computed mesh will have a sub-voxel resolution.

Since each vertex can have one of two states, *above* and *below*, and each cube has eight vertices, there is a total of 2^8=256 possible patterns of intersections between the surface to be constructed and the cube. However, by taking advantage of different symmetries in the marching cube the large number of patterns can be reduced from 256 to only 14 (Fig. 2.16); thus the algorithm simply keeps an index for each case depending on the label of the vertex and then performs the corresponding triangulation stored on the index.

The *marching cubes* algorithm developed by Lorensen and Cline[75], which dates back to 1987, remains as the most commonly used approach in the reconstruction of 3D models, or triangular mesh representations, from medical volumetric datasets.

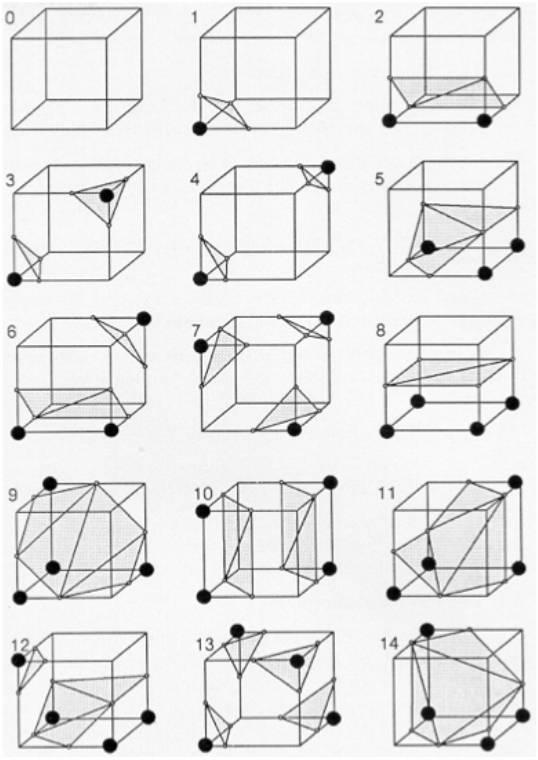

Figure 2.16. The different patterns of triangulation in the marching cubes algorithm. The black dots represent voxels marked as below the isovalue (image taken from Lorensen and Cline [75]*).*

2.4.7 Triangulation: Delaunay and constrained triangulations

A *triangulation* of a set of points *S* in 2D is the set of triangles whose vertices are in *S* and whose edges connect pairs of points in *S*[76]. Each point of *S* can occur in at least one triangle and the edges can only intersect at the vertices.

A common requirement of a triangulation is that it cannot contain deformed triangles, with internal angles being too big or to small. An example of this problem is shown in Fig. 2.17(a) for two triangulations of the same set of points: the angle α is too small when compared with the angle β, thus producing enlarged triangles; on the contrary in the triangulation of the right both angles have similar proportions, and the obtained triangles are more symmetrical.

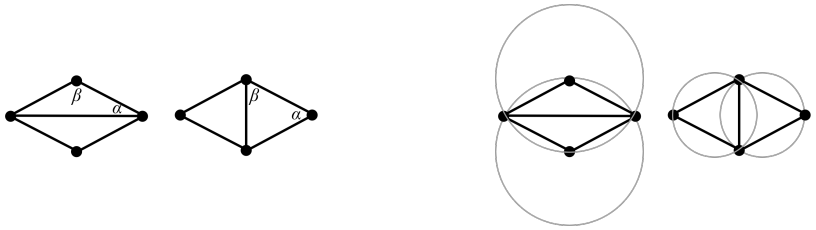

(a) *(b)*

Figure 2.17. (a) Two different triangulations of the same set of points; notice the skewed triangles obtained on the left. (b) The corresponding circumcircles containing each of the triangles in (a). The triangulation on the left of (b) is not a Delaunay triangulation, since for both circumcircles a vertex lie inside.

The problem of maximizing the minimum angle (α in Fig. 2.17(a, left)) is solved by the *Delaunay triangulation* method. The method is based on the definition of circumcircles, which is the circle containing the three vertices in the triangle. A triangulation of the set of points *S* is a Delaunay triangulation if no point in *S* lies inside the circumcircle of any of the obtained triangles. Fig. 2.17(b) shows the circumcircles corresponding to the triangulations in Fig. 2.17(a). As seen on Fig. 2.17(b, left), besides containing the three vertices of the triangles, each circumcircle also contains a fourth vertex inside; on the contrary, the circumcircles of Fig. 2.17(b, right) contain only the vertices of the triangles. In this last case, a Delaunay triangulation was obtained. As seen from this example, a Delaunay triangulation tends to avoid the presence of skewed triangles by maximizing the minimum angle of each triangle.

Another commonly used algorithm is the *constrained conforming Delaunay triangulation*, proposed by Shewchuk[77], in which some segments in the set of points are forced into the triangulation while also maintaining the Delaunay property. Consider for example the set of points in Fig. 2.18a, describing and L-shaped two dimensional object. If a conventional Delaunay triangulation is applied (Fig. 2.18b) the set of triangles obtained satisfy the Delaunay property but do not comply with the shape described by the boundary. Conversely, when applying a constrained conforming Delaunay triangulation, both the shape described by the boundary as well as Delaunay property are preserved, as in Fig. 2.18c.

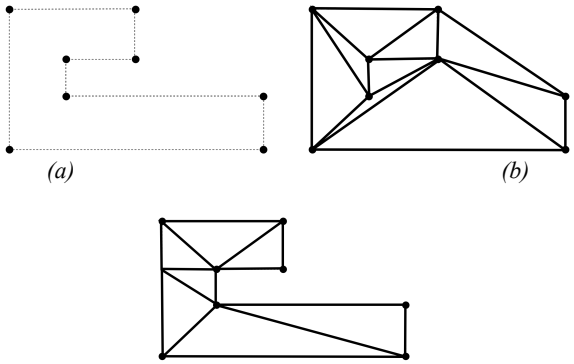

Figure 2.18. Comparison between the conventional Delaunay triangulation and the constrained conforming Delaunay triangulation. (a) The set of points to be triangulated (the dashed lines represent the boundary to be preserved. (b) Result of applying the Delaunay triangulation. (c) The results of the constrained conforming Delaunay triangulation.

The algorithm by Shewchuk[77] will be used in this work both for obtaining 3D mesh representation of the leaflets surface and of the vena contracta and anatomical regurgitant orifice 3D surfaces.

2.4.8 Neighborhood of a vertex in polygonal meshes

Several shape and curvature features that can be computed for a polygonal mesh, rely in the definition of a local set of neighbors for each vertex. In this section a definition of the *Nth* order neighborhood of a vertex in a mesh is given.

For a vertex *vi* in a triangular mesh, the *first-order,* or *1-ring* neighborhood, is the set of all vertices connected to v_i by an edge. In the same way, the *Nth-order* or *N-ring* neighbors of the vertex are the set of vertices located at a distance of *N* edges from v_i.

This concept is exemplified in Fig. 2.19, where the *1-ring* and *2-ring* neighbors of a vertex are displayed in blue and red. Notice that all the *2-ring* neighbors in Fig. 2.19 are located at a geodesic distance of exactly two edges from v_i.

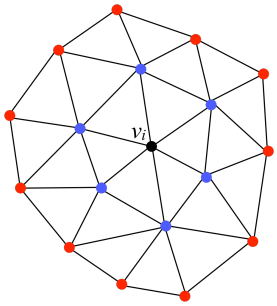

Figure 2.19. The set of 1-ring (blue) and 2-ring (red) neighbors of a vertex in a polygonal mesh.

2.4.9 Curvature features on polygonal meshes

Curvature is one of the fundamental features used in the analysis and description of a polygonal mesh. Simply speaking, the curvature measures how strongly a curve deviates from a straight line: the higher the curvature, the lower its resemblance to a line[78]. The *principal directions* are the directions in which the curvature reaches its maximum and minimum values; the values of the curvature at the principal directions are known as the *principal curvatures*, and are commonly denoted as k_1 and k_2. Other useful shape curvature descriptors are the Gaussian (*K*) and mean (*H*) curvatures:

$$K = k_1 k_2$$
$$H = \frac{k_1 + k_2}{2} \tag{2.5}$$

Different approaches have been proposed for the computation of the curvature in a discrete, polygonal mesh, including differential geometry operators, finite differences and quadric fitting[79]. The use of polynomial approximations, or quadric fitting, makes the computation of curvature more robust against noise in the reconstructed mesh, and thus it has been the preferred approach in this work.

Let v_i be the vertex on the mesh at which the curvature must be computed; let also $\boldsymbol{X}$ be the set of *N-ring* neighbors (usually *N=1*) of v_i and $\boldsymbol{n}_i$ be the unit normal at v_i. The steps of the quadric fitting algorithm are[79], [80]:

i. To obtain a local coordinate system, centered on *vi*, and with one of its axes being $\boldsymbol{n}_i$. The remaining axes $\boldsymbol{u}$, $\boldsymbol{v}$ can be easily computed using the Gram-Schmidt process;

ii. To perform a linear least-squares fit of a full quadric polynomial of the form:

$$h(\mathbf{u},\mathbf{v}) = a_{00} + a_{10}\mathbf{u} + a_{01}\mathbf{v} + a_{20}\mathbf{u}^2 + a_{11}\mathbf{u}\mathbf{v} + a_{02}\mathbf{v}^2 \tag{2.6}$$

iii. To approximate the neighborhood of v_i by defining the patch:

$$\mathbf{x} = (\mathbf{u},\mathbf{v},h(\mathbf{u},\mathbf{v})) \tag{2.7}$$

iv. To calculate the coefficients of the first and second fundamental forms of $\mathbf{x}$:

$$\begin{aligned} E &= \mathbf{x}_u \cdot \mathbf{x}_u & L &= \mathbf{n} \cdot \mathbf{x}_{uu} \\ F &= \mathbf{x}_u \cdot \mathbf{x}_v & M &= \mathbf{n} \cdot \mathbf{x}_{uv} \\ G &= \mathbf{x}_v \cdot \mathbf{x}_v & N &= \mathbf{n} \cdot \mathbf{x}_{vv} \end{aligned} \tag{2.8}$$

where $\mathbf{x}_u$, $\mathbf{x}_v$ and $\mathbf{x}_{uu}$, $\mathbf{x}_{uv}$, $\mathbf{x}_{vv}$ denote first and second derivatives evaluated at the origin, and $\mathbf{n}$ is:

$$\mathbf{n} = \frac{\mathbf{x}_u \times \mathbf{x}_b}{\left\| \mathbf{x}_u \times \mathbf{x}_b \right\|} \tag{2.9}$$

v. Finally, the values of Gaussian, mean and principal curvatures at vertex v_i are:

$$\begin{aligned} K &= \frac{LN - M^2}{EG - F^2} \\ H &= \frac{GL + EN - 2FM}{2(EG - F^2)} \\ k_1 &= H + \sqrt{H^2 - K} \\ k_2 &= H - \sqrt{H^2 - K} \end{aligned} \tag{2.10}$$

The *shape index* and *curvedness* measures, defined by Koenderink et al. [81], represent an alternative way to the quantification of curvature:

$$SI = \frac{2}{\pi} \arctan\left(\frac{k_1 + k_2}{k_1 - k_2} \right) \tag{2.11}$$

$$C = \sqrt{\frac{k_1^2 + k_2^2}{2}} \qquad (2.12)$$

where k_1 and k_2 are the principal curvatures. *SI* is a value in the range [-1,1] representing the shape the surface has: concave for $-1<SI<-½$, hyperboloid if $-½<SI<½$ and convex if $½<SI<1$. On the other hand, *C* is a positive value that measures how highly or gently curved a point is; thus, almost flat regions in the surface will exhibit near zero *C* values.

2.4.10 Concavity measures on polygonal meshes

Another useful metric in mesh segmentation approaches is the quantification of a vertex concavity or convexity, which allows the detection of prominent features of the mesh. In this work, the *concaveness* operator, defined by Chen and Georganas[82], is used to determine the degree of concavity/concaveness of each vertex in the mesh.

The same notation used for curvature computation is required in this case: v_i is the vertex on the mesh at which the concaveness must be computed; $\boldsymbol{X}$ represents the set of *N-ring* neighbors (usually $N=1$) of v_i and $\boldsymbol{n}_i$ is the unit normal at v_i.

The steps for the computation of *concaveness* at each vertex of the mesh are:

i. Compute x_c, the centroid of the *N-ring* neighbors;
ii. Compute the vector $\overrightarrow{v_i x_c}$, going from v_i to x_c;
iii. Compute the concaveness as:

$$d = \overrightarrow{v_i x_c} \cdot \mathbf{n}_i \quad [m^2] \qquad (2.13)$$

The vectors $\overrightarrow{v_i x_c}$ and $\mathbf{n}_i$ are shown in Fig. 2.20 for a concave and a convex vertex. As seen from this figure, the significance of the concaveness measure (*d*) is twofold:

- When a vertex is concave, the vectors $\overrightarrow{v_i x_c}$ and $\mathbf{n}_i$ point in nearly the same direction, and thus a positive concaveness value is obtained. On the contrary when the vertex is convex, the directions are almost opposite and the concaveness exhibits negative values;
- The magnitude of the *concaveness* is directly proportional to the distance between x_c and v_i (i.e., to the magnitude of $\overrightarrow{v_i x_c}$). A more convex or concave vertex implies a higher distance between the centroid of the neighbors and the vertex, and thus higher concaveness values are obtained. In contrast, when a vertex is on an almost flat neighborhood, both centroid and v_i are closer and the concaveness approaches to zero.

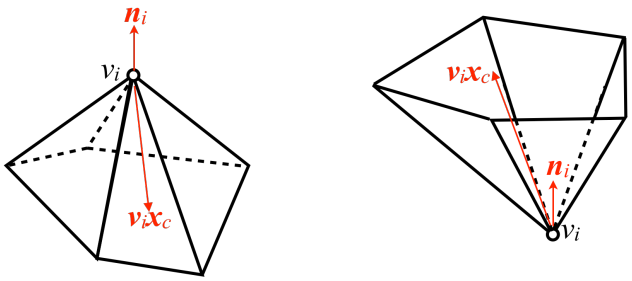

Figure 2.20. A convex (left) and a concave (right) vertex, with the corresponding directions for the unit normal and the centroid-vertex vectors used in the computation of concaveness

The advantage of the computation of concaveness, when compared with the previously described approaches for curvature computation, is that the latter is affected

by stability and convergence issues when approximating a continuous function, the polynomial, to a discrete, noisy and sparse surface given by the vertex and its neighbors. On the contrary, *concaveness* computation involves simpler operations such as the computation of the centroid and the dot product, thus conferring more stability and reliability for this approach, especially in noisy polygonal meshes.

2.4.11 Shape features of polygonal meshes

The proposed approaches for quantification of vena contracta and anatomic regurgitant orifice (described in the next chapters) rely on the extraction of shape features from 3D representations of the regurgitant back-flow and of the atrial and ventricular cavities. In particular two shape features were used in this method: the shape diameter function and the average geodesic distance.

The shape diameter function defined by Shapira et al. [83] is a scalar function defined on the mesh surface, and its computation measures the approximate diameter of the object's volume in the neighborhood of each point on the surface. The algorithm relies on a simple ray-tracing point-mesh intersection procedure: for each vertex on the surface, a cone centered on its inward unit normal is defined; then, several rays inside this cone are traced and the intersection of each ray with the polygonal mesh is established. The shape diameter function is then defined as the weighted average of all rays lengths, with the weight being the inverse of the angle between the ray to the center of the cone (since rays with larger angles are more frequent, and therefore have smaller weights). An example of this function computed on a 3D polygonal surface is shown in Fig. 2.21.

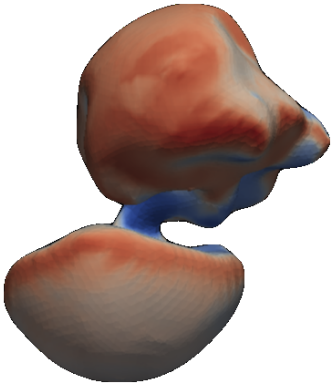

Figure 2.21. The shape diameter function computed on a 3D mesh. The color map of the function values goes from blue (narrow diameter) to red (wide diameter).

The average geodesic distance, proposed by Zhang et al. [84], is another scalar function defined on the mesh that measures the separation degree of a vertex in the surface. Thus, vertices near the center of the mesh, closer to other vertices, exhibit low average geodesic distance values, whereas vertices near the extremity of the object will have higher values. Let v_i be a vertex in the surface S for which the average geodesic distance will be computed; let v_j be any other vertex belonging to S, and $g(v_i,v_j)$ be the geodesic distance between the v_i and v_j vertices. Then, the average geodesic distance of vertex v_i, $A(v_i)$, is defined as:

$$A(v_i) = \frac{\int_{v_j \in S} g(v_i, v_j) dv_i}{Area(S)} \qquad (2.14)$$

Fig. 2.22 shows an example of the average geodesic distance function, computed on the same surface used in Fig. 2.21. Notice that regions toward the extremity of the object exhibit higher average geodesic distance values (near red).

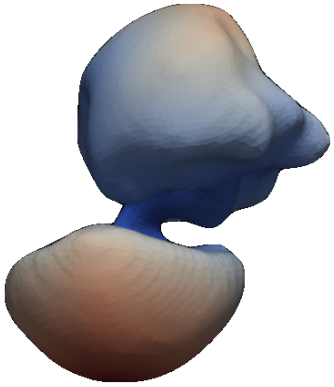

Figure 2.22. The average geodesic distance computed on a 3D mesh. The color map of the function values goes from blue (short distance) to red (long distance).

Chapter 3

Nearly-automated segmentation and quantification of mitral annulus and leaflets

This chapter presents a detailed description of the proposed method for the characterization of mitral annulus (MA) and mitral leaflets (ML) in systolic frames from 3DE datasets. After manually tracing a few MA points and the coaptation line (CL), the MA and ML (both posterior and anterior) 3D representations are automatically obtained. From these representations, several morphological parameters are computed, including novel regional ML thickness, tenting and curvedness.

First, an overview of related works and the description of the different considered approaches will be given. Next, the detailed description of the method as well as its implementation are presented.

3.1 Related works

Much of the existing approaches make use of 3DTEE datasets, given their superior resolutions compared to the 3DTTE ones, making them adequate for the implementation of automated or user-guided approaches. The methods in literature for the delineation of MA and ML, and for their morphologic quantification, can be divided in two groups: image-based and model-based. In addition, two commercial solutions for the quantification of MV morphology are available, and will be briefly discussed at the end of this section.

3.1.1 Image-based MA and ML segmentation algorithms

The works of Schneider et al. [24] and Pouch et al. [23] aim at segmenting the MA and ML in systolic frames of the 3DE by extracting image-based features that guide the process of segmentation.

In [24] a MA semi-automatic segmentation algorithm is presented, were only one point, located near the center of the MV, is defined by the user. The algorithm relies on a thin-tissue detector for the enhancement of leaflet-like structures, which, combined with the original grayscale volume, allows the segmentation of the MA using an evolving contour approach. The algorithm requires only 2 min to complete the segmentation, and it was extensively validated both on human as well as in excised porcine hearts, with errors in segmentation of the order of 1.2-1.8 mm.

In spite of this accuracy, several drawbacks still remain. The use of a fixed thickness value (2mm) for the enhancement of the leaflets assumes both a uniform distribution of regional thickness and that abnormal valves thickness lies within this range. These hypotheses are not valid since even in normal valves the regional thickness exhibits different distribution patterns, whereas in diseased valves these values may be well above this limit. In addition, it is assumed that the MA lies in the region where the thin-tissue of the ML is attached to the thicker-tissue of the ventricular walls. However, the anterior annular portion is in continuity with the aortic root (see sec. 2.1.2 and Fig. 3.1 below) and the automatic differentiation of these two anatomic portions becomes difficult

given the absence of thin-thick tissue interactions. Consequently, albeit not reported, it is expected a lower accuracy of the algorithm in this region.

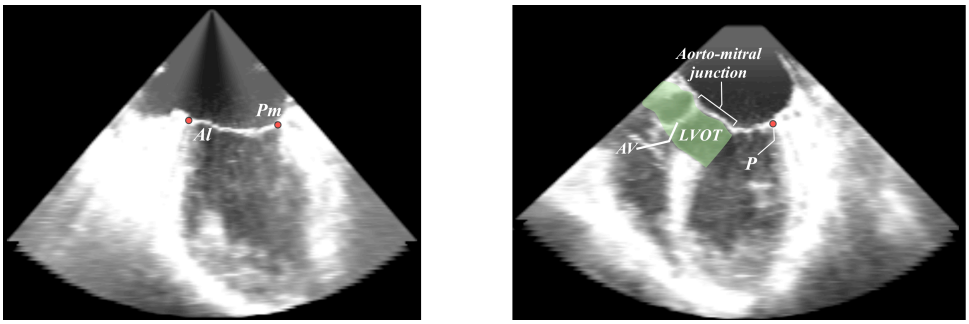

Figure 3.1. Two 2D cut-planes of a mitral valve. Left: the cut-plane contains the Antero-lateral (Al) and Postero-medial (Pm) annular points, both satisfying the criterion of thin-thick tissue interactions. Right: a cut-plane containing the anterior (A) and posterior (P) annular portions; in this case thin-thick tissue interactions are present only in the P point, whereas the A point is located in the aorto-mitral junction and cannot be easily identified.

Pouch et al. [23] proposed a semi-automated algorithm for the segmentation of both MA and ML. After computing a 2D projection of the original 3D volume, the user traces the contours for the MA and the anterior ML (between 15 and 20 points). An active contour algorithm, constrained by the traced contours, allows obtaining a 3D representation of the valve; finally, a medial surface representation of MA and ML is computed using deformable models. Approximately 1 min is required for the initialization of the algorithm, and the reported accuracy is approximately 1.3 mm. In addition, the medial surface representation allows the computation of regional thickness distribution throughout the ML surface.

Since initialization relies on a 2D projection, an adequate orientation of the MV within the 3DE dataset is required, thus constraining the algorithm to specific valve projection acquisitions. In addition to the initial contours, a user-defined threshold must also be set to ensure proper segmentation of the valve with the active contours algorithm. Finally, the use of deformable model incorporates a fixed thickness prior (as in the previous algorithm) and requires the definition of an initial template from the existing dataset, a selection that is not trivial given the wide range of MV pathologies. The template used by Pouch et al. [23] was obtained from one patient with mitral regurgitation, and thus inaccurate results are expected with valves exhibiting different morphologies (for example with implanted rings, or even in normal populations).

Except for [23], were regional leaflet thickness is obtained using deformable models, none of the approaches implemented regional characterization of the ML surface, and only global MA and ML parameters were computed.

3.1.2 Model-based MA and ML detection algorithms

Most of these methods[26], [29], [34], [28], [30] aim at modeling the dynamics of the MV complex from diastole to systole. They incorporate different geometrical, morphological or mechanical priors into the model and, as a result, the approximate location of the MA and ML on each frame can be delineated.

Several studies [26], [30] and [34] present closely related methods for the 4D detection of the MV complex. In all cases, geometrical primitives are used to define an initial raw model of the valve, followed by the incorporation of patient-specific morphological details computed from a machine learning algorithm. In [26] and [30], only end-diastole configuration is obtained with this approach, followed by a biomechanical model that infers the closed valve configuration. On the contrary, in [34] end-systole and end-diastole configurations are first computed, and then propagated to the

remaining frames in the dataset using learned motion priors. The three algorithms are completely unsupervised and have been thoroughly validated in large populations (1566 datasets in [34]). Average errors of 2.82 and 2.75 mm for ML delineation are reported in [26] and [30], whereas in [34] the accuracy is of the order of 1.36 mm but is presented only in terms of global location of the valves. Also in [30], in only 63% of the cases the simulation of the closed valve led to accurate coaptation of the ML. In addition, the use of a machine learning algorithm requires a careful selection of the training set so as to ensure that different valve pathologies are "learned" by the algorithm.

In [29], a 4D delineation of the MA and ML is proposed. In this case, a "user-in-the-loop" semi-automated approach is used for segmenting the valve in diastole, by a combination of an evolving contour and a thin-tissue detector. Next, the closed valve configuration is obtained via a finite element model, which confers the ML properties similar to those of fabric (such as tensile, compressive and bending modulus). Reported average errors were of the order of 4-5 mm.

This method presents several drawbacks. First, the thin-tissue detector, as previously observed, used thickness priors not suitable in several pathologies; second, a proper segmentation of the valve during diastole requires continuous user supervision; finally, the reported levels of accuracy (4-5 mm) are high when compared with some annular and leaflet dimensions.

Finally, Schneider et al. [28], [27] proposed two alternative approaches for segmenting the ML. In [28] the ML are detected on the end-diastolic frame and an evolving surface algorithm is used to obtain the closed valve configuration. In [27] a semiautomated algorithm, using graph-cuts and level-sets, allows the segmentation of the ML only in open valve configurations. Although reported errors are low (0.6-0.8 mm), validation is limited to a few datasets and the utility of such methods in larger and more variable populations remains to be confirmed.

In spite of computing the dynamics of the MV from diastole to systole, and of being almost completely automated, the discussed methods lack a detailed delineation of the ML surface in closed valves configuration, since in most cases this is obtained by incorporating several priors or by using learning methods that limit the accuracy of the detection to the characteristics of the training set or the versatility of the geometrical, morphological or mechanical models. In addition, and also as with the image-based approaches, none of the previous methods implements a detailed regional quantification of the ML morphology, and just a few allow the computation of some of the most clinically significant global parameters for annulus and leaflets.

In Table 3.1, a detailed summary of the main characteristics of the previous image and model-based algorithms can be found.

Method	Attributes*	Characteristics	Computation time	Testing			Drawbacks**
				Number of datasets	Pathologies	Accuracy	
Schneider et al. [24]	Image-based, static	MA segmentation using thin-tissue detector and graph-cuts	2 min	10 human 3DE, 6 excised porcine hearts	NL, MVP, MR	1.2-1.8 mm (global)	Use of fixed thickness value; not sensitive to detection of MA in aortomitral junction
Pouch et al. [23]	Image and mode-based, static	MA and ML segmentation using active contours and deformable models	1 min (initialization)	14 human 3DTEE	MR	1.3 mm for ML segmentation	Specific orientation of the MV in the dataset; manual tracing of initial contours; user-define threshold; requires a thickness prior; requires definition of a template MV from the existing dataset.
Voigt et al. [26]	Model-based, dynamic (from diastole to systole)	MA and ML detection in all frames using biomechanical models and geometrical priors; incorporate machine learning techniques; completely unsupervised	43 sec	30 3DE	NR	2.81 mm for ML detection	Lack of detailed delineation of ML during systole (low accuracy); incorporation of several priors/assumptions; requirement of training datasets;
Mansi et al. [30]			20 sec	200 3DE	MVP, MR, mitral stenosis, calcified mitral annulus	2.75 mm for ML detection	
Ionasec et al. [34]			4.8 sec	1516 3DE, 690 cardiac computer tomography.	MVP, MR, mitral stenosis	1.36 mm for global location of the valve	
Burlina et al. [29]		Semi-automatic initialization; MA and ML detection using biomechanical model	NR	NR	NR	4-5 mm for ML detection	Leaflet thickness prior; user-in-the-loop supervision; low accuracies
Schneider et al. [28]		Active contours and biomechanical model	NR	2 3DTEE	NR	0.6 mm	Limited validation
Schneider et al. [27]	Model-based	ML segmentation during systole	NR	4 3DTEE	NR	0.8 mm	Limited validation; works only on open valves

* The *static* attribute means that segmentation is performed in only 1 frame of the 3DE dataset
** None of the methods implements detailed regional quantification of the ML.

Table 3.1. Main characteristics of the current existent algorithms for the segmentation/detection of MA and ML. MVP: mitral valve prolapse; MR: mitral regurgitation; NR: not reported.

3.1.3 Commercial tools for the segmentation and quantification of MA and ML

One of the available computational tools is QLAB Quantification Software[20] (MV quantification plugin), by Philips. The software is capable of generating a 3D representation of the MA and ML structures from a frame in the 3DE dataset (transesophageal only), as well as the quantification of global morphologic parameters (such as MA circumference, area, height, antero-posterior and antero-lateral/postero-medial diameters, length of coaptation line, anterior and posterior ML surfaces and total tenting volume). The segmentation procedure is completely manual, and requires the selection of 16 annular points, from which the leaflets profile is subsequently manually traced in multiple cut-planes (between 10 to 15); this high level of user interaction requires extended times (close to 10 min) to achieve a complete characterization of the valve, which limits the use of this tool in clinical practice.

The second package is Tomtec 4D MV-Assessment [21], which allows the dynamic and morphologic analysis of the MV. The workflow requires the initial selection of the end and early systolic frames in the dataset; using anatomic landmarks and the frames of interest, the MA, ML, coaptation line and aortic valve position are dynamically tracked throughout the systolic phase[85]. The required time to execute this workflow is 5 min, and the same set of morphological parameters as in QLAB is available.

As with the previous methods, only quantification of global parameters is available, and none of these software packages performs detailed regional morphologic characterization of the ML surface.

3.2 Preliminary solutions

Given the limitations presented by the model-based methods, the aim of this thesis was to implement a method for the segmentation of MA and ML based on image features and with minimal user interaction, using 3DTEE datasets. The considered strategy was to initially segment the MA, since it would serve as spatial constrain to delimit the location of the ML. Using this approach, two methods for the MA segmentation were preliminary tested: segmentation on the mesh domain, and detection in the image domain. Both algorithms were tested on 3DTEE datasets, in particular on 9 MVs with normal dimensions, and on 6 of patients with enlarged MV dimensions.

3.2.1 MA segmentation in the mesh domain

Given the 3D saddle shape of the MA, the goal of this approach was to obtain a 3D mesh representation of the tissues containing the MV (annulus and leaflets) and other adjacent structures, and then use a mesh segmentation procedure directly on this 3D representation in order to obtain the annular contour. The next logical step would be to cut and extract only the mesh components located inside the annular contour, thus obtaining a combined ML surface representation.

To obtain a crude 3D model of the MV and the surrounding structures, the marching cubes algorithm[75](sec. 2.6.6) was applied on a binary mask. Several approaches for the computation of this binary mask were considered, ranging from simple thresholding[86] (which resulted inadequate given the non-bimodal distribution of intensity levels in the image) to region growing (which requires fine tuning of the algorithm's parameters in addition to user-guided initialization of seed points). In the end, a complete automatic approach using fuzzy c-means clustering that incorporates spatial information[87] was tested on the available datasets, giving good results. This approach takes advantage of the fact that neighboring voxels have similar intensities, and the

probability that they belong to the same cluster is higher. By incorporating this information into the membership function of the clustering algorithm, misclassified voxels from noisy regions (as the regions affected by speckle noise in the ultrasound data) are assigned to the correct cluster. In this clustering approach each pixel is labeled with a probability (in the range [0,1]) of belonging to a specific cluster.

Thus, the binary mask containing the MV and adjacent structures was automatically obtained by first clustering the voxel intensities using the modified fuzzy c-means approach of Chuang et al.[87], and then thresholding the given probabilities with a fixed threshold, equal to 0.5 and defined heuristically from the images in the dataset. Once computed the mask, the marching cubes algorithm was used and a first polygonal mesh representation of the MV and surrounding tissues was obtained. Since noise in the image affects the quality of the obtained 3D model, additional filtering, via a mesh smoothing algorithm[88], was required. Fig. 3.2(a) shows an example of the obtained mesh.

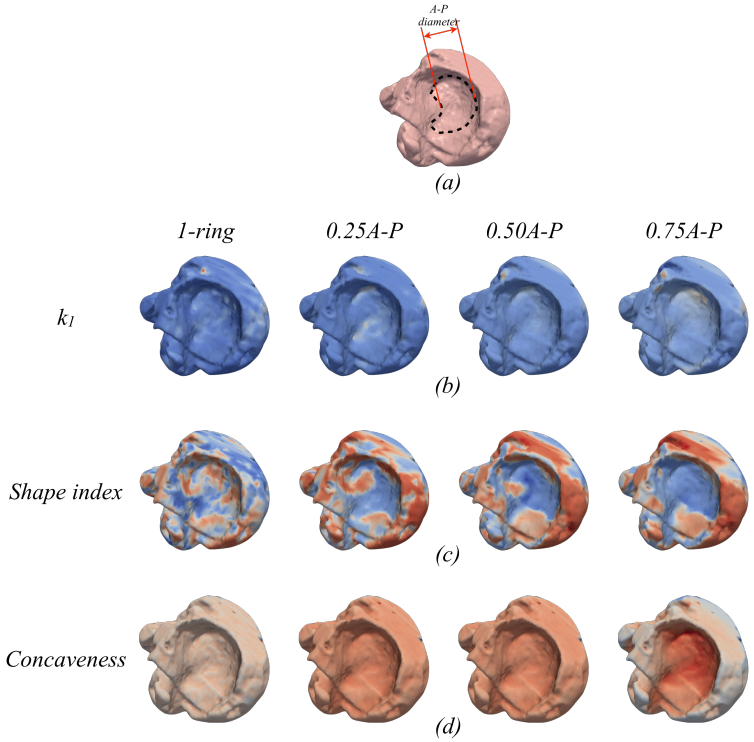

Figure 3.2. An initial mesh representation of the MV and surrounding structures (a), and representative curvature/shape/concaveness features computed on the mesh at different scales (b), (c), (d) (see text below for details).

From the model in Fig. 3.2(a), a high concavity region, manually delineated with the black dashed contour, can be visualized. This region corresponds to the approximate location of the MA. Given the presence of this concave portion of the mesh, it was expected that the computation of curvature and concaveness features would allow the enhancement of this region. However, these features are visible only at certain scales (or vertex neighborhood sizes). In particular, the ring sizes used for computation must be related with the expected dimensions of the annular contour. Taking this into account, the neighborhood sizes were defined based on the antero-posterior (A-P) diameter of a normal MV (approximately 30 mm).

Thus, several curvature and concaveness parameters (Gaussian and mean curvatures, principal – k_1 and k_2 – curvatures, curvedness, shape index and concaveness; see secs. 2.4.9 and 2.4.10) were computed at scales of 1-ring (i.e. only the first degree neighbors of each vertex were considered; sec. 2.4.8) and 25%, 50% and 75% of the A-P

diameter of a normal MV. Only the most representative results are depicted in figures 3.2(b), (c), (d), corresponding to the principal curvature k_1, Koenderink's shape index[81] (Eq. 2.11) and Chen's et al. concaveness[82](Eq. 2.13). From the previous figure it can be observed that when the ring size used for computation of features approached the A-P diameter, the concave region containing the valve became more enhanced (in particular see the last column of Fig. 3.2(c) and 3.2(d)). In addition, from the set of computed parameters, the concaveness was the most homogeneous and robust feature against noise.

Before considering any following segmentation stage using the set of computed features, several limitations of this approach were identified:

i. Given the noise in the 3DE image, and the variability between the datasets from patient to patient, the MA was not always clearly depicted on the reconstructed mesh. This prevented the correct enhancement of annular regions using any of the previously described features;
ii. Depending on the pathology, in some cases the ML surface can be flattened or bulged toward the atria. Thus, instead of an almost concave surface, a high convexity region might be present. In conclusion, it was not guaranteed that the MV would always correspond to a complete concave region in the 3D model;
iii. As seen from the last column in Fig. 3.2(b), (c) and (d), a ring-size close to the A-P diameter allowed the enhancement of most of the region containing the valve. However, the use of wide ring sizes requires extended computation times, since the estimation of the *N-ring* neighborhood of a vertex varies with $O(N.n)$, where n is the number of vertices in the mesh. As an example, for a mesh with 12000 vertices and a ring-size of 30 (corresponding to the 75% of the A-P diameter in Fig. 3.2(a)), the required time for computing the desired features was approximately 8 min on a 2GB RAM, 2.26 GHz Intel Core Duo laptop (on a C++ optimized implementation of the algorithm). This limits the applicability of the approach in the clinical setting.
iv. The computed features are not homogeneous within the MV regions. For example part of the MV contains concave regions, as depicted by the shape index in Fig. 3.2(c) (in blue) while some other portions are convex (in red). On the contrary, the concaveness is almost uniform within the valve (Fig. 3.2(d)), but also regions outside the annular contour exhibit similar values. The absence of a defined contour in the feature map made difficult the extraction of the MV. In fact, two different approaches were tested: a region growing segmentation algorithm, as proposed by Vieira et al. [80], and an active contour algorithm for the MA segmentation, as proposed by Karasev et al. [89]. In both cases, the shape index and concaveness maps were used, but results were not satisfactory. The region growing method over-segmented the MV and it was highly dependent on the smoothness of the computed maps (which in turn is dependent on the smoothness of the 3D surface). On the contrary, the active contour method required an initial contour, manually defined, that must lie close to the final MA contour. However, depending on the utilized feature (shape index or concaveness), the algorithm convergence is not guaranteed and the final contour represents an over- or under-segmented version of the desired MA (Fig. 3.3).

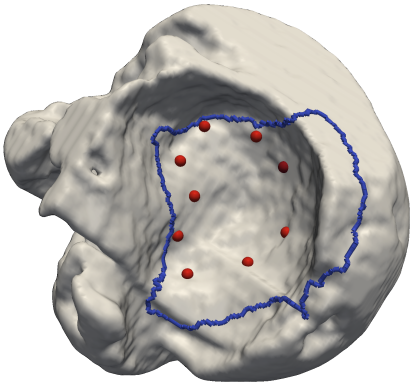

Figure 3.3. Results from the active contour segmentation proposed by Karasev et al[89]. *A set of user-defined points (in red in the figure) are located near the MA contour; the final contour after application of the algorithm is depicted in blue (notice that the MA is oversegmented, in spite of the initial user-defined points).*

Given the previous limitations a different method, acting directly in the image domain, was considered.

3.2.2 Methods in the image domain

To operate directly on the 3DE volume, first a similar approach to that proposed by Schneider et al. [24] was considered (i.e., the use of a thin-tissue detector followed by a graph-cut and active contour algorithm to segment the MA). However, given the limitations related to the use of a thin-tissue detector with a fixed thickness value (as discussed in Sec. 3.1.1), a multiscale approach, similar to that proposed by Frangi et al. [90] for the *veselness* filter, was considered.

Briefly, the 3DE volume $V(x,y,z)$ was convolved with several Gaussian kernels with different standard deviations σ_i. A total of 10 standard deviations, from 1 mm to 5 mm, was used, thus covering the expected range of thickness values both in normal and diseased valves. For each scale σ_i, the Hessian and eigenvalues (λ_1, λ_2 and λ_3) of each voxel were computed. Given that in sheet-like structures such as the leaflets $\lambda_3 >> 0$, only this value was used for the enhancement of leaflets. Fig. 3.4 shows a 2D cut-plane of a 3DE dataset and the result of applying the leaflet enhancement filter defined previously. As noticed from this figure, good isolation of the leaflet structure from the surrounding tissue is achieved with this filter, with the advantage, when compared with [24], that no fixed thickness value was predetermined.

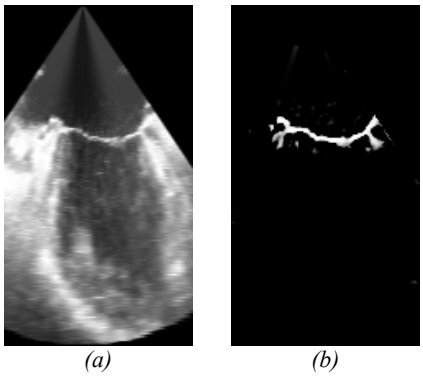

(a) *(b)*

Figure 3.4. Results of the multiscale enhancement of ML. (a) A 2D cut-plane of the original grayscale volume; (b) The resulting leaflet-enhanced image. The multiscale enhancement is performed on the 3D dataset.

In spite of the good results obtained with the multiscale filter, the main drawback of the global segmentation of the MA proposed by Schneider et al. [24] still remains: the leaflet-enhancement filter is not capable of differentiating the leaflets from the aortic root in the anterior annular portion. Both leaflets and aorto-mitral junction are enhanced by the filter, and thus inaccurate results are obtained in this region when using the evolving contour for segmenting the MA.

Thus, the use of 2D skeletons from corresponding 2D cut-planes taken from the original 3DE volume was also considered. The hypothesis was that most of the annular locations correspond to branch points in the 2D skeleton, with the exception of the aorto-mitral junction. Fig. 3.5 shows the result of computing the 2D skeleton from a binary mask obtained from the leaflet-enhanced image of Fig. 3.4(b).

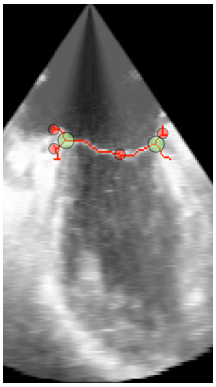

Figure 3.5. The 2D skeleton (in red) computed from the image in Fig. 3(b). Skeleton's branch points corresponding to the annular locations are marked with green circles, while spurious branch points are marked with red circles.

Two problems were observed in this approach:

i. Noise in the image affects the computation of the skeleton. The result is that branches are not only present in the annular locations, and thus an additional step is required to remove spurious branch points. Given the unpredictable behavior of the skeleton's shape, this step might not always ensure adequate results.
ii. Even if spurious branch points were correctly removed, the approach fails in the aorto-mitral junction given the continuity between the leaflets and the aortic root. In this region there is no presence of branches indicating the annular location.

All the previous approaches fail to correctly detect the anterior annular portion, given the non-uniform morphology of the MA. Thus, the segmentation algorithm must deal with these local differences to ensure the correct detection of the MA. In addition, the segmentation of the ML remains to be answered.

The next section presents the proposed algorithm which takes into account the previous morphological constrains.

3.3 Detailed description of the proposed algorithm

The proposed algorithm operates on 2D radial cut-planes obtained from the original 3DE volume. This choice takes into account the local differences existing between the anterior and the remaining portions of the annulus. User guidance is required

given the lack of prominent features that allow the differentiation of annular locations from the surrounding tissue.

The idea behind the MA segmentation algorithm is to track in space a set of initialized points, defined on some of the radial cut-planes, using a modified block-matching technique. This results in the detection of a total of 72 points belonging to the annular contour in 3D space. Once segmented the MA, each radial cut-plane will contain two annular points: the ML surface can then be found by constructing a connected path between each pair, using a graph-based algorithm driven by the intensity levels of the leaflets.

A morphological prior is that the coaptation line corresponds to the most tented regions of the ML surface, i.e. located at a higher distance from the MA plane. Thus, if the regional distribution of tenting is computed from the MA and ML 3D representations, it is expected that its local maxima will be distributed along the CL. Using this information, the CL can be detected on the ML surface, allowing subsequent differentiation of anterior and posterior ML.

Fig. 3.6 depicts the main steps involved in the proposed algorithm. Such steps are described in detail below.

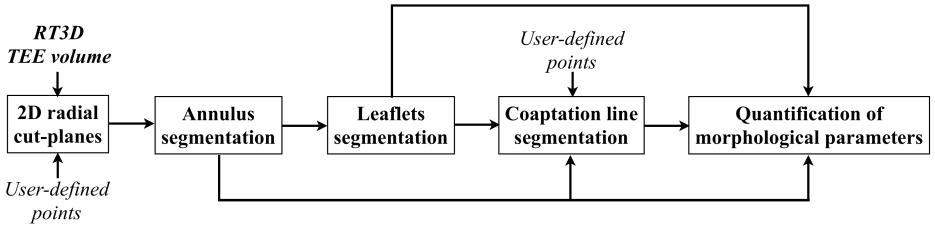

Figure 3.6. Flow chart for the MA, ML and CL segmentation algorithm.

3.3.1 Initialization

After selecting a frame at closed valve (systole), the user navigates the 3D volume and selects three points: one at the anterior (A) and posterior (P) annular locations and one in the left atrium (LA) (Fig. 3.7(a)). The mid-point between A and P defines the origin of the coordinate system. The axis in the longitudinal direction, perpendicular to the axis connecting A and P and pointing in the atrial direction, is then used to obtain a stack of 36 rotational cut-planes (inter-plane angular spacing of 5º). The LA point ensures that each plane in the stack is correctly oriented in 2D space (i.e., with the LA lying on top of the valvular plane and the LV on the bottom), regardless of the orientation of the MV within the acquired 3D volume.

A set of 6 additional annular points is subsequently initialized:

- Antero-lateral (Al) and Postero-medial (Pm) points, selected from a cut-plane orthogonal to that containing the A and P points and passing through the origin of the coordinate system (Fig. 3.7(b))
- Four points on the anterior portion of the MA on four cut-planes in the stack, symmetrically positioned (at ±15° and ±30°) around A (Fig. 3.7(c)).

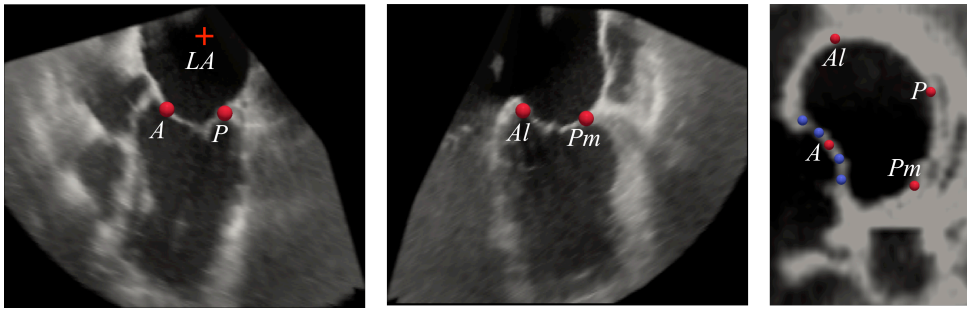

(a) (b) (c)

Figure 3.7. Location of the initialization points required for the MA segmentation algorithm. (a) A, P and LA points; (b) Al and Pm points; (c) An atrial view of the MA depicting the denser initialization (blue points) of the anterior region.

3.3.2 Mitral annulus segmentation

Given the stack of 36 rotational cut-planes and the 8 initialized points, the task is to locate the remaining 64 annular points P_i (i = 1…64) on the non-initialized cut-planes. To do so, a modified spatial tracking algorithm, based on block matching and on the enhancement of annular locations is proposed. When using this approach, a cost image for each cut-plane is defined, representing the probability of a pixel of being an annular location. By tracing a connective path between consecutive cost images, corresponding to adjacent spatial positions, a 3D representation of the annular contour using a graph-based approach can be obtained.

In the first step, the algorithm automatically selects a region-of-interest (ROI) for each of the initialized planes (Fig. 3.8a). A region-of-search (ROS) is automatically defined on P_i (Fig. 3.8b) and two complementary image features are then computed: the weighted normalized cross-correlation (WNNC)[91] between both images (Fig. 3.8c) using ROI as template, and a junction-enhanced (JE) image computed from ROS. Then, both WNNC and the JE image are combined to obtain the cost-function for each plane.

Both ROI and ROS sizes were defined heuristically from a set of 9 valves with normal dimensions: the ROI size was chosen to ensure that the tracked region (the annular location) was unique, whereas ROS size was set based on the maximum expected spatial displacement (in vertical and horizontal directions) of the annular points. The dimensions of each region in the implemented algorithm were then set to 24x28 mm for the ROI and 30x40 mm for the ROS. As will be shown in the results section, these parameters were adequate not only for the segmentation of MA with normal dimensions, but also for enlarged diseased valves and for valves with implanted rings (presenting reduced annular dimensions).

3.3.2.1 Junction-enhanced (JE) image

This step enhances the regions in ROS (Fig. 3.8b) that satisfy the thin-thick criterion. First, the average leaflet thickness from initialized planes is automatically estimated. To do so, for each user-defined point an inner region of the ROI containing a portion of the leaflet is automatically extracted from the corresponding cut-plane, and used to compute two feature images:

- Leaflet medial axis: obtained by using the gray-level intensities of the selected portion as costs in a 2D graph, and then applying a dynamic programming algorithm[66], [68], [92] (sec. 2.4.3). This algorithm finds a connective path within the selected region and corresponding to the leaflet medial axis.
- Leaflet binary mask: obtained using the modified fuzzy c-means approach of Chuang et al.[87]. Briefly in this algorithm a probability image is obtained using the conventional fuzzy c-means method but incorporating a spatial

filtering kernel, thus reducing the presence of spurious blobs and noisy spots in the probability map. Once obtained that map, a simple threshold is applied resulting in the binary leaflet mask. From this mask, the Euclidean distances (from mask's inner points to its boundary) are computed.

From these images, the leaflet thickness is obtained by averaging the Euclidean distances along the medial axis of each of the leaflet sections.

The second step in the JE image computation is to apply a morphology-based approach to enhance the MA points locations, on the assumption that they correspond to regions where objects with a thickness similar to that of the leaflets attach to thicker objects. To this aim, a binary mask $\mathbf{M}_{ROS}$ (Fig. 3.8d), is obtained from ROS (using the same fuzzy segmentation algorithm previously mentioned), from which two additional binary images are computed:

$$\mathbf{M}_{THICK} = \mathbf{M}_{ROS} \circ \mathbf{L} \qquad \text{(Eq. 1)}$$

$$\mathbf{M}_{THIN} = \mathbf{M}_{ROS} \veebar \mathbf{M}_{THICK} \qquad \text{(Eq. 2)}$$

$\mathbf{M}_{THICK}$ (Fig. 3.8e) contains only the thick tissue, and is the result of applying a morphological opening operation on $\mathbf{M}_{ROS}$ using a disk-shaped structuring element, $\mathbf{L}$, with its diameter equal to the average leaflet thickness previously computed.

$\mathbf{M}_{THIN}$, contains only the thin tissue and is the result of an *XOR* logical operation between $\mathbf{M}_{THICK}$ and $\mathbf{M}_{ROS}$ (Fig. 3.8f).

Finally, for each binary object in $\mathbf{M}_{THIN}$, the centroid of the set of points closer to $\mathbf{M}_{THICK}$ (in the Euclidean sense) is computed. The centroids *A*, *B* and *C* in Fig. 3.8g are an example of this computation, where it is worth noting that, despite being artifacts owed to the local tissue morphology, also *B* and *C* satisfy the thin-thick tissue junction criterion. To remove these false annular locations, the orientation of each of the corresponding binary object in $\mathbf{M}_{\mathrm{THIN}}$ is computed, and only the structure with the most horizontal orientation is kept (i.e., only *A* in Fig. 3.8g remains).

This criterion can be applied since the initialized LA point ensures that in the cut-planes the ML exhibit an almost-horizontal orientation. The remaining point is then convolved with a 2D Gaussian kernel that emulates the uncertainty in the position of the detected junction, thus resulting in the JE image (Fig. 3.8h) where pixels values closer to 1 denote higher probability of belonging to the annulus.

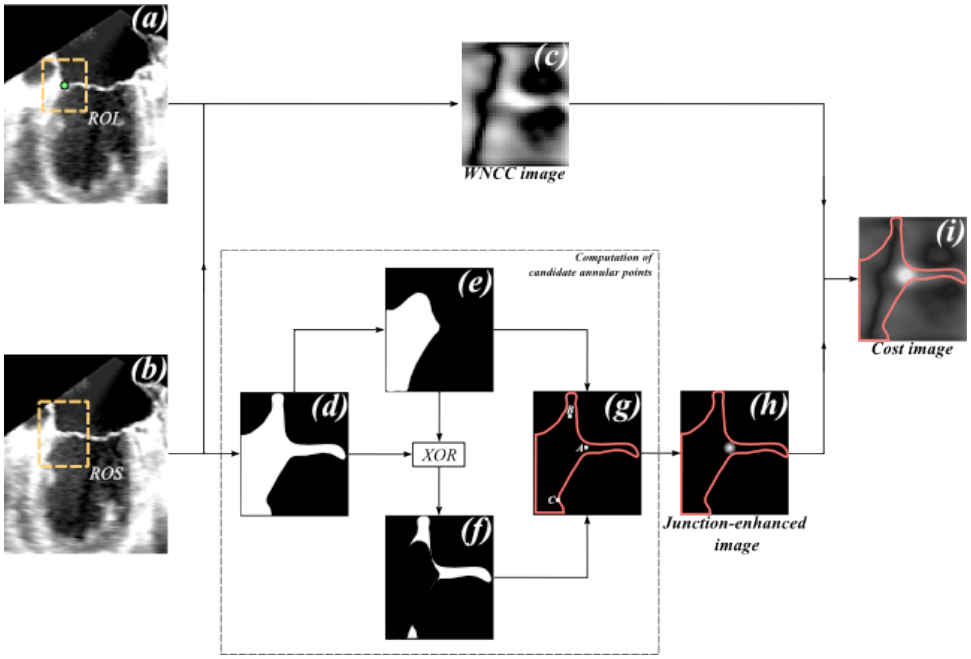

Figure 3.8. Computation of cost-image on a non-initialized cut-plane. ROI and ROS images (a, b); (c) computed WNCC image; (d) $\mathbf{M}_{ROS}$: binary mask of ROS image; (e) $\mathbf{M}_{THICK}$: thick-tissue mask; (f) $\mathbf{M}_{THIN}$: thin-tissue mask; (g) resulting candidate annular locations (A, B, and C); (h) junction-enhanced image; (i) computed cost image.

3.3.2.2 Cost image computation and mitral annulus detection

The WNCC and JE images are averaged together, thus resulting in the cost image C (Fig. 3.8i). This procedure, along with the use of 9 initialization points, adds robustness to the detection of MA points even in the anterior annular portion.

After repeating this procedure on each of the P_i planes, a set of 64 cost images is obtained. This set is further divided into 8 different subsets $\mathbf{s}_m$ (of M rows, N columns and O slices each), each of them delimited by a pair of initialized cut-planes. Both $\mathbf{s}_m$ and the corresponding position of the initialized pair of points are then used to construct a directed weighted graph on which a Dijkstra shortest path[67] (sec. 2.4.3) algorithm is applied, thus automatically computing the remaining annular locations.

In the proposed implementation, each graph (Fig. 3.9) has a set of O layers (corresponding to each of the slices in $\mathbf{s}_m$) delimited by a pair of start and end nodes (corresponding to the 2D locations of the pair of points in adjacent initialized cut-planes). The voxels, v_{ijk}, in $\mathbf{s}_m$ act as the n_{ijk} nodes in the directed graph, whereas their corresponding intensity-transformed values, $1\text{-}v_{ijk}$, define the corresponding edge costs, thus ensuring that annular locations will be associated with non-negative edge values closer to zero.

The directional edges in the graph are defined by using a radial connectivity constraint applied both to start and end nodes, as well as to internal nodes:

- Assuming that the 2D locations, in cost image coordinates, of the pair of initialized points are (x_s,y_s) and (x_e,y_e), the start and end nodes will be connected to nodes in the first and O-th layers within a circular neighborhood of radius r, and centered on the locations (x_s,y_s) and (x_e,y_e) of the corresponding first and O-th slices in $\mathbf{s}_m$. As with ROI and ROS sizes, this radial connectivity was determined heuristically from the set of 9 normal valves and it was set to 5 mm, corresponding to the maximum expected displacement (horizontal and vertical) of the annular point between consecutive slices.

- In the same way, internal edges between consecutive layers in the graph are defined by connecting each node n_{ijk} ($k = 1 \ldots O\text{-}1$) on the k-th layer with the corresponding set of nodes in the $k+1$-th layer that lies within a neighborhood of radius r of the corresponding slices in $\mathbf{s}_m$.

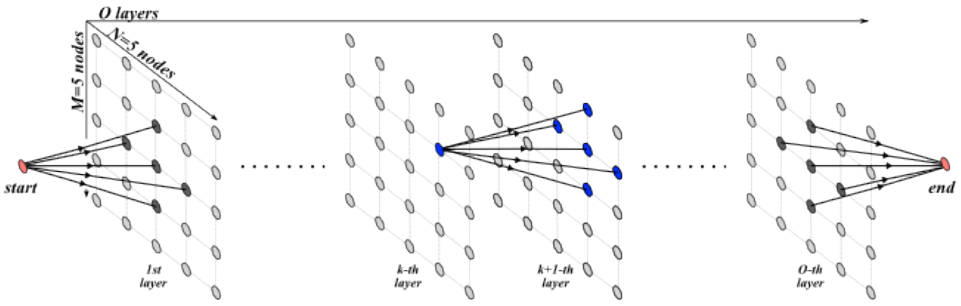

Figure 3.9. A 3D graph used for computing annular points using Dijkstra algorithm. A simple structure of O layers and 5x5 nodes/layer and a radial connectivity constraint of 1 pixel is assumed in this example. The directed edges for the "start" and "end" nodes, as well as for a node in the k-th layer, are depicted as continuous black lines with arrows.

Once applied the Dijkstra algorithm on the corresponding graphs, the set of 64 unknown annular locations is obtained and then transformed from 2D cost function coordinates into the corresponding 3D coordinates which, along with the 8 initialized points, represent the segmented MA.

The utilization of this graph-based algorithm to construct the MA, instead of the global maximum of individual cost-images, ensures spatial smoothness and continuity between the detected points.

3.3.3 Segmentation of mitral leaflets and computation of regional thickness

This step is fully-automated, and takes as input the set of 3D annular locations (72 points) previously computed, along with the corresponding stack of 36 radial cut-planes. It exploits the fact that, on each plane, the gray-level intensity distribution along the leaflet cross-section exhibits a Gaussian pattern, with higher values near the center of the leaflet.

First, the algorithm computes the negative image of each cut-plane, thus ensuring that pixels near the center of the leaflet will have lower intensity values (Fig. 3.10, left). Then, a 2D directed weighted graph is constructed using as edge weight the corresponding intensity values. Finally, the minimum cost path between the corresponding set of annular points is computed using the Dijkstra algorithm, resulting in the combined leaflets medial-axis (continuous line in Fig. 3.10, left). The set of computed medial-axes (one for each radial cut-plane) constitutes the output of the algorithm, and corresponds to a 3D point cloud that closely follows the 3D medial surface of the mitral leaflets.

In addition, as shown in the right panel of Fig. 3.10, regional thickness can be computed on each cut-plane by first obtaining a binary mask of the ML, using the spatial fuzzy c-means segmentation approach mentioned previously, and then computing the distance transform from each point in the mask to its boundary. The regional thickness is simply twice the value of the distance transform through the leaflets medial axis on each ML point.

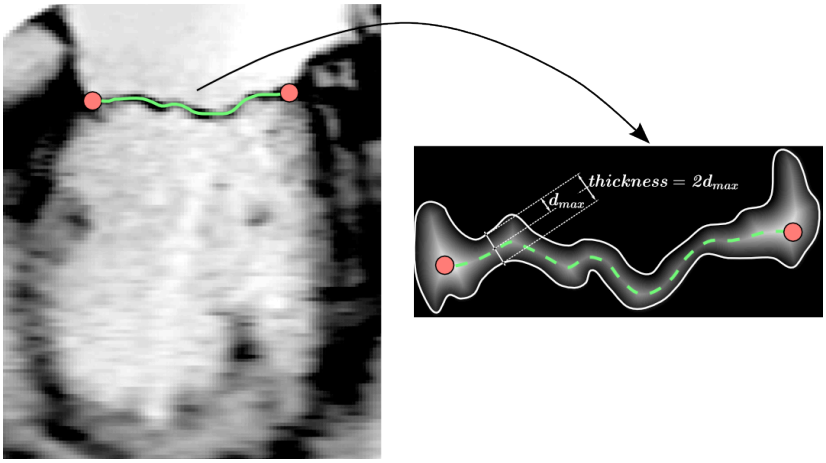

Figure 3.10. Left: detection of the ML medial axis (green continuous line) from the set of detected annular points (in red); right: obtention of the leaflet regional thickness from the computed medial axis.

3.3.4 Computation of MA and ML 3D representations and regional tenting

First, the 3D MA points cloud is fitted using a 4th order Fourier approximation to remove noise, thus obtaining the 3D MA contour (Fig. 3.11a). Then, principal component analysis is applied on the set of fitted points, with the resulting eigenvectors representing the principal directions of the fitted annular contour.

Both point clouds, for MA and ML, are then projected onto this local coordinate system, which allows the computation of a constrained conforming Delaunay triangulation [77], bounded by the 3D annular contour. After triangulation and smoothing[88] of the 3D ML surface, owed to the noise in the original 3DE dataset, the 3D mesh representations of the MA and ML are obtained (Fig. 3.11 a and b).

Since MA and ML models are aligned with the main axes of the local coordinate system, the x and y locations of each vertex will be the same, differing only in the z coordinate. This allows the computation of regional tenting, defined as the absolute difference in the z coordinate between corresponding vertices in the MA and ML meshes (Fig. 3.11b).

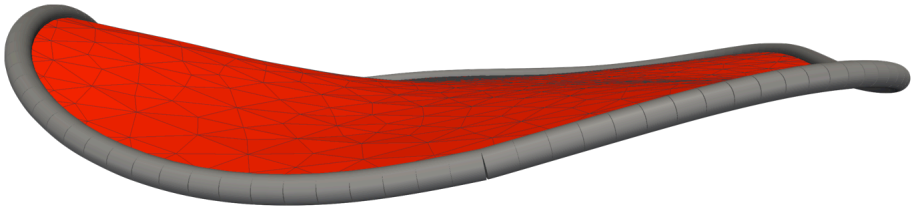

(a)

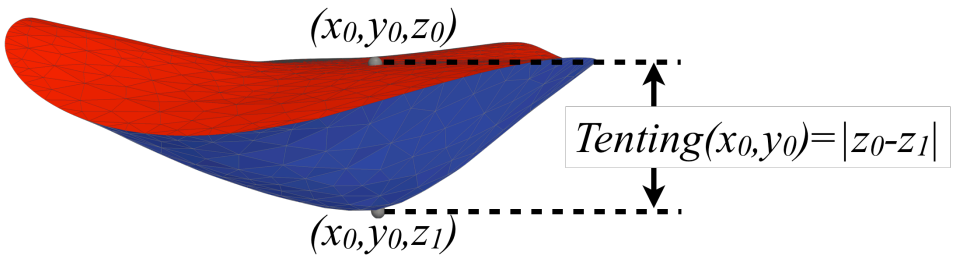

(b)

Figure 3.11. (a) The computed 3D annular contour (gray) and the 3D MA surface obtained via conforming constrained Delaunay triangulation. (b) The ML 3D surface (blue) and the computation of tenting as the z distance between MA (red) and ML surfaces.

3.3.5 Computation of regional curvedness from the ML combined surface

The heterogeneity in the ML surface shape is quantified using curvature measurements. In particular, a modified version of the procedure described in [93] for the LV endocardial curvature was implemented.

A multiscale curvedness feature is computed for each vertex on the ML surface, with the scale defined as the size of the *N-ring* neighborhood. For each node, $\boldsymbol{x}_i$, on the mesh representing the ML surface, a set of *N-ring* neighbors ($N=1...5$) was defined; for each of these neighborhoods, a quadric polynomial function was locally fitted and maximum (k_1) and minimum (k_2) curvature values were obtained[80].

Local 3D surface curvedness[81] for each vertex $\boldsymbol{x}_i$ and at each scale, $c_s(\boldsymbol{x}_i;N)$ ($N=1...5$), was computed using the Eq. 3:

$$c_s(x_i;N) = \sqrt{\frac{k_1^2(x_i;N) + k_2^2(x_i;N)}{2}} \quad [m^{-1}] \qquad \text{(Eq. 3)}$$

Each of the $c_s(\boldsymbol{x}_i;N)$ computed values was then normalized by the average curvedness of all vertices at scale N, and then in the range [0,1]. Finally, the curvedness for each node of the leaflet mesh was set as the maximum of all computed normalized curvedness values at different scales (Fig. 3.12). The use of multiple scales, instead of only a simple *1-ring* neighborhood, reduces the effect that noise has in the computation of curvature values (which is more relevant for reduced ring sizes).

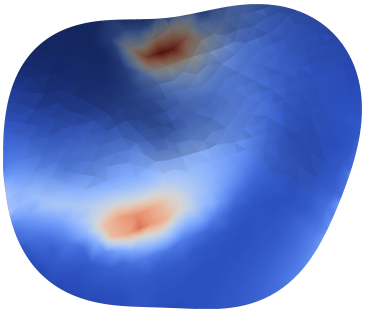

Figure 3.12. Atrial view of a 3D representation of the ML surface depicting the computed multi-scale curvedness, with the red spots corresponding to more curved regions.

3.3.6 Detection of coaptation line and segmentation of anterior and posterior ML

The semi-automated delineation of the coaptation line is based on the fact that this line corresponds to the regions on the ML mesh that exhibit high local tenting values. Once the regional tenting distribution is computed (see previous section), the corresponding ML combined surface and regional tenting pattern are visualized on a 3D rendered view and superimposed on the original 3DE volume (Fig. 3.13a). On this 3D rendered view, the user initializes some points (between 4 and 6) on the ML mesh along the visible coaptation line, where the local tenting height color information simplifies the selection.

The location of each of the user selected-points, $\boldsymbol{x}_i$, is subsequently refined to ensure that they correspond to regional tenting local maxima. To do so, for each point the *1-ring* set of neighbors, $\mathbf{X}$, is computed. Then, the following criterion is applied:

- If *Tenting*($\boldsymbol{x}_i$) is higher than the tenting value at any of its neighbors, then the location of $\boldsymbol{x}_i$ is kept, otherwise
- the original location of $\boldsymbol{x}_i$ is replaced by that of the vertex in $\mathbf{X}$ with the higher tenting.

The resulting set of points serves as initialization for a graph-based procedure: a weighted graph is constructed using the 1-ring connectivity of each vertex on the ML mesh, and with the edge weights defined by the corresponding vertex tenting height. Then, the Dijkstra algorithm is applied between consecutive pairs of initialized points, thus obtaining a complete delineation of the CL. The A and P ML representations are then obtained by cutting the ML mesh through the computed CL (Fig. 3.13b).

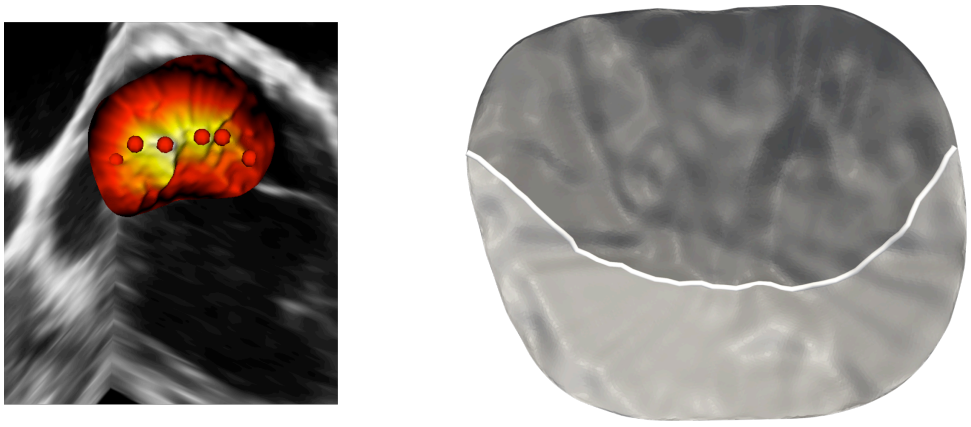

(a) (b)

Figure 3.13. Overview of the method for detecting the coaptation line. (a) Original grayscale volume with the ML combined surface superimposed; the color map represents the regional tenting (with yellow regions corresponding to higher values), whereas the user-defined points are colored in red. (b) An atrial view of the segmented A (dark gray) and P (light gray) ML; the white line corresponds to the computed coaptation line.

3.3.7 Quantification of morphological parameters

In addition to the novel regional parameters of thickness, tenting and curvedness, a set of conventional global morphological parameters was also obtained from the 3D MA contour and the 3D mesh representations of MA and ML:

1) MA perimeter;
2) A-P diameter, defined as the axis starting from the saddle horn – the highest point in the MA measured in the orthogonal direction to the MV plane – and passing through the MA centroid (Fig. 11 (a))
3) Al-Pm diameter, perpendicular to the A-P axis and passing through MA centroid (Fig. 3.14a);
4) MA height, computed as the height of the MA bounding box (Fig. 3.14a);
5) MA 3D surface area and projected MA 2D area, both computed from the 3D MA mesh representation (Fig. 3.14b);
6) A and P ML surface areas;
7) Tenting volume, defined as the volume enclosed by MA and ML meshes.

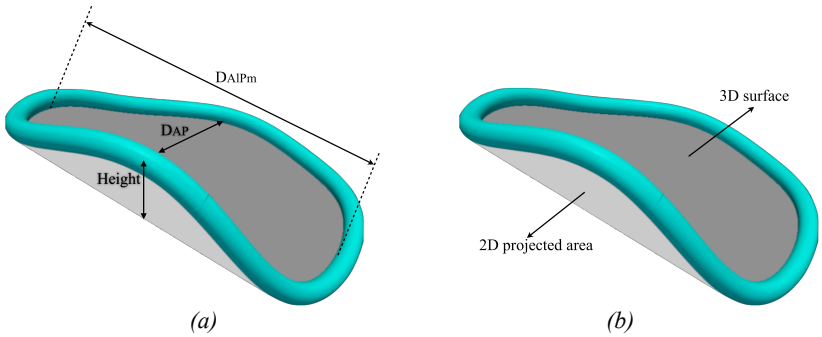

(a) (b)

Figure 3.14. Definition of MA morphological parameters. (a) A-P and Al-Pm diameters and MA height; (b) MA 3D surface and 2D projected areas.

3.3.8 Current limitations

The current implementation is not fully sensitive to prolapsed valves, and in these pathologies further manual interaction would be necessary to allow ML segmentation. In addition, the method is focused on the static configuration of the MV (performed on one systolic frame), thus ignoring the dynamic changes in the MV apparatus.

3.3.9 Algorithms' implementation

The graphical user interface for the initialization of the MA and CL segmentation algorithms was implemented in C++ using the open source programming libraries *VTK* (Visualization Toolkit) [94] and Qt[95]. This interface allows the user to navigate the 3DE volume and to perform, step-by-step, the initialization of the 8 annular points and of the left-atrial point for the segmentation of the MA.

The initialization of the coaptation line segmentation algorithm was implemented in Python and using the *VTK* wrappings. Finally, the MA and ML segmentation and quantification algorithms were implemented in Matlab[96].

On average the initialization procedure (i.e. the selection 9 points for initialization of the MA segmentation procedure, and of between 4 and 6 points for the detection of the coaptation line) required 1.5 min, whereas computation time in Matlab required 1 min approximately. This means that a complete characterization of MA and ML during systole requires roughly 2.5 min.

Chapter 4

Validation of the algorithm for the morphological quantification of MA and ML

This chapter presents a detailed validation of the proposed method for the characterization of mitral annulus (MA) and mitral leaflets (ML) in systolic frames from 3DE datasets. This validation has been carried on both in human and porcine specimens, and the protocols along with the corresponding results are presented in the next sections, followed by a final discussion and comparison with state of the art algorithms.

4.1 Population and validation protocols in humans

Ultrasound datasets were obtained from patients enrolled at the University of Chicago Hospitals (Chicago, IL), or at Centro Cardiologico Monzino (Milan, Italy) undergoing clinically indicated 3DTEE imaging. The respective protocols were approved by the local Institutional Review Board, and informed consent was obtained from all participants.

In both cases, the 3DE studies were performed using the iE33 system (Philips Medical Systems, Andover, MA) equipped with fully sampled matrix-array 3DTEE transducer (X7-2t): the probe was positioned at the midesophageal level with a 120° tilt and images acquired using the wide-angled acquisition mode, in which ECG-triggered wedge-shaped subvolumes were obtained over four consecutive cardiac cycles. Each acquired volume included the MV, the aortic valve and the proximal ascending aorta, having dimensions of roughly 200x200x200 voxels with a voxel resolution ranging from 0.2 to 1.0 mm.

A heterogeneous group *G* of 33 consecutive patients (mean age 50±10 years) was used to test the accuracy of the proposed algorithm. This set was composed of:

- 9 subjects with normal left-ventricular volume and mitral apparatus (NL), undergoing 3DTEE to rule out a stroke cardioembolic source.
- 12 patients with dilated cardiomyopathy (*DCM)*, presenting global left ventricular dysfunction (ejection fraction <35%) and dilatation.
- 12 patients (MVR) with degenerative MV disease and severe mitral regurgitation that underwent MV repair with conventional surgical techniques on the ML and, when indicated, on subvalvular apparatus, with implantation of partial annular rings on the posterior leaflet.

To assess the MA and ML segmentation and quantification algorithms' accuracy, the following experiments were designed:

1) MA and ML automated segmentations were compared point-to-point with manual tracings performed by an expert cardiologist, and assumed as the "gold standard", by computing Euclidean distances expressed in pixels in 2D space. The tracing was performed on each of the 36 radial cut-planes, resulting into the 72 points corresponding to the MA locations, and respective leaflets medial axis. For ML comparison, a spline interpolation was applied on the set of

automatically computed tracings, to ensure that each ML medial axis contained the same number of points as in the manual tracings.

2) To validate the accuracy in the computation of the ML regional thickness and regional tenting height, the same set of radial cut-planes and corresponding automated and manual tracings were used. For each pair of corresponding radial cut-planes and tracings, the local 2D thickness and ML tenting were computed, and corresponding errors, in pixels, were then obtained.
3) To represent the average error distribution in the considered groups, the local error distribution obtained from each dataset was remapped into a circular parametric map (Fig. 4.1). Then, results from the considered patients were combined to compute a parametric map of median errors.
4) The accuracy in the computation of CL and in the segmentation of A and P ML was assessed by comparing the length of the CL and the morphological parameters of leaflets with reference values previously published.

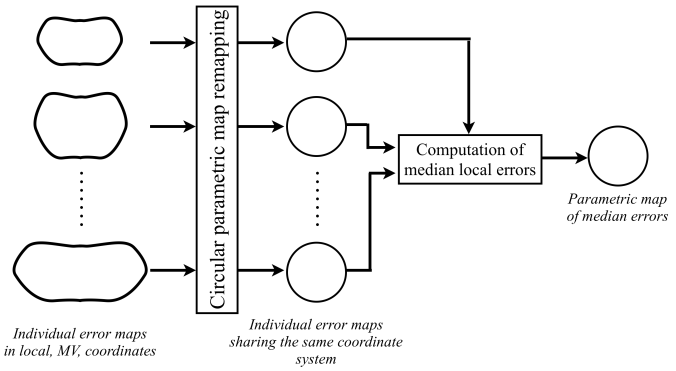

Figure 4.1. Schema illustrating the procedure for the computation of the parametric maps of error distribution for each population.

To test the reproducibility of the morphological parameters obtained from both the MA and ML 3D representations, in terms of their inter-observer variability, two operators, blinded to each other, analyzed separately all the datasets in the *NL* group. To test for intra-observer variability, the first operator repeated the analysis twice. Both inter- and intra-observer variability was quantified using the coefficient of variability (CV) (defined as the absolute difference between the pair of measures in percent of their mean), Bland-Altman analysis (with corresponding limits of agreement) and Pearson correlation coefficient (r).

In addition, to test for the accuracy of the extracted parameters, the mean of the two measures obtained by the first operator was compared against a "gold standard", defined as the parameters (MA perimeter, A-P and Al-Pm diameters, height, 3D and 2D surfaces, ML exposed surface area) computed by a cardiologist using a conventional manual approach (MVQ-QLAB, Philips). Bland-Altman and linear correlation analyses were applied to determine the bias and limits of agreement.

4.2 Results of validation in humans

4.2.1 Algorithm's accuracy

The generation of the "gold standard" involved a total of 324 2D tracings (36 leaflet tracings and 72 MA points for each of the 33 subjects in the *G* group) to be used for comparison, and took about 10 minutes/dataset.

Figure 4.2 shows the regional distribution of the median error (Euclidean distances) in pixels between the manual and automated results relevant to the annular contour points location, counter-clockwise along the annular profile (from Al to Al), computed for the whole *G* group. It is possible to notice the globally low median error of 1.1 pixels (25% and 75% percentile: 1; 2 pixels, respectively) along the MA contour, showing the good performance of the automated detection algorithm. In particular, slightly higher distances (between 1 and 1.7 pixels) were observed near the A point, when compared with regions between Al and Pm points (between 0 and 1.5 pixels). Considering the broadest space resolution encountered (1.0 mm), this corresponds to the highest expected error of 1.4 mm in the Al and Pm regions and of 1.6 mm around the A point.

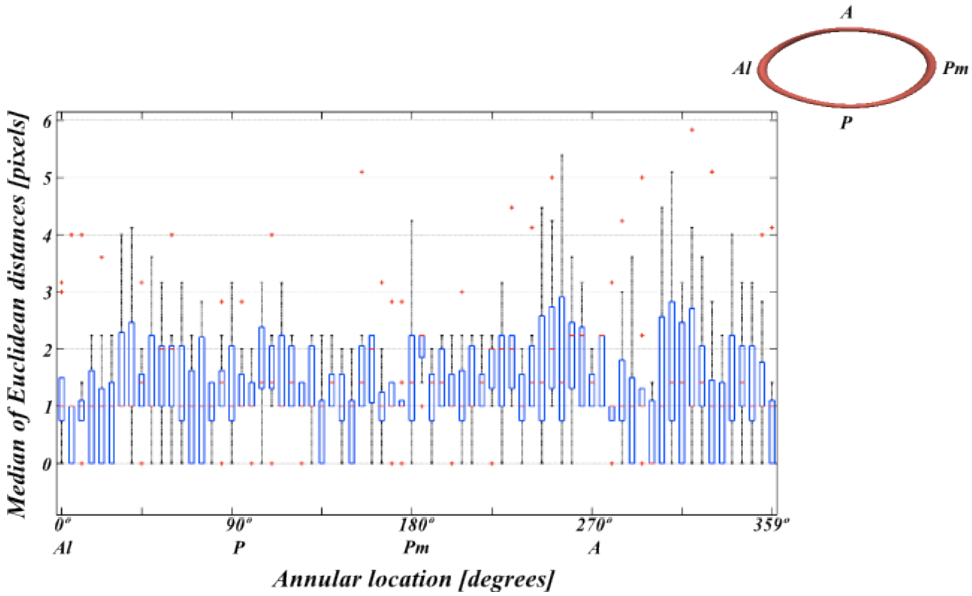

Figure 4.2. Box and whisker plots (represented as median, first and third quartiles) for the regional error distribution in the MA segmentation algorithm versus manual tracings. The corresponding anatomical locations on the MA are depicted on the right.

In addition, Table 4.1 summarizes the errors computed considering separately each group of patients (*NL*, *DCM* and *MVR*), and allows to confirm that the MA segmentation algorithm offers the same level of accuracy both in normal and diseased valves.

Annular section \ Group	NL	DCM	MVR
Anterior	1.2 (1.0; 2.1)	1.3 (0.8; 1.6)	1.0 (0.8; 1.8)
Antero-lateral	0.9 (0.2; 1.8)	0.9 (0.4; 1.6)	1.1 (0.3; 1.5)
Posterior	1.0 (0.0; 2.1)	1.0 (0.2; 1.4)	1.2 (0.0; 1.8)
Postero-medial	1.0 (0.6; 1.4)	0.9 (0.0; 1.6)	0.9 (0.3; 1.2)

Table 4.1. Distribution of regional errors of the MA segmentation algorithm of reach of the tested groups. Errors are presented as median, 25% and 75% percentiles.

Figure 4.3 shows the distribution of absolute errors for the ML segmentation (first row) and of the signed errors for thickness and tenting computation (second and third rows). The error distributions are represented as circular parametric maps and were

obtained by comparing the manual and automated results. For each parameter, the same error color scale was used in all groups to allow for visual comparison.

The errors in ML segmentation (Fig. 4.3, first row) are comparable among populations, and range from 0 to 2 pixels, with a median error in the *G* group equal to 0.8 pixels (with 25% and 75% percentiles of 0.25 and 1.2 pixels, respectively). In *MVR,* slightly higher errors around the posterior annular region, given the presence of suture points as a result of the annuloplasty procedure, were observed. In *NL,* slightly higher errors around the anterior annular portion were visible.

The median of signed errors for thickness and tenting computation (Fig. 4.3, second and third rows) show values of -0.1 pixels (-1.5; 1.2 pixels), and of 0.2 (-1.6; 1.5 pixels), respectively for these two regional parameters. Again, in *NL* a slightly higher tenting height overestimation, located towards the left half of the map and reflecting the positioning error shown in the ML segmentation around the anterior region, was visible. Also in *MVR* this behavior was present, but with higher errors in thickness and tenting around the posterior annular portion, as a result of the presence of suture points mentioned previously.

Table 4.2 summarizes the ML segmentation errors in each of the groups (*NL*, *DCM* and *MVR*). As seen from Fig. 4.3 and already confirmed for the MA segmentation, ML errors in segmentation and quantification of regional thickness and tenting were not population dependent, with result comparable among the groups.

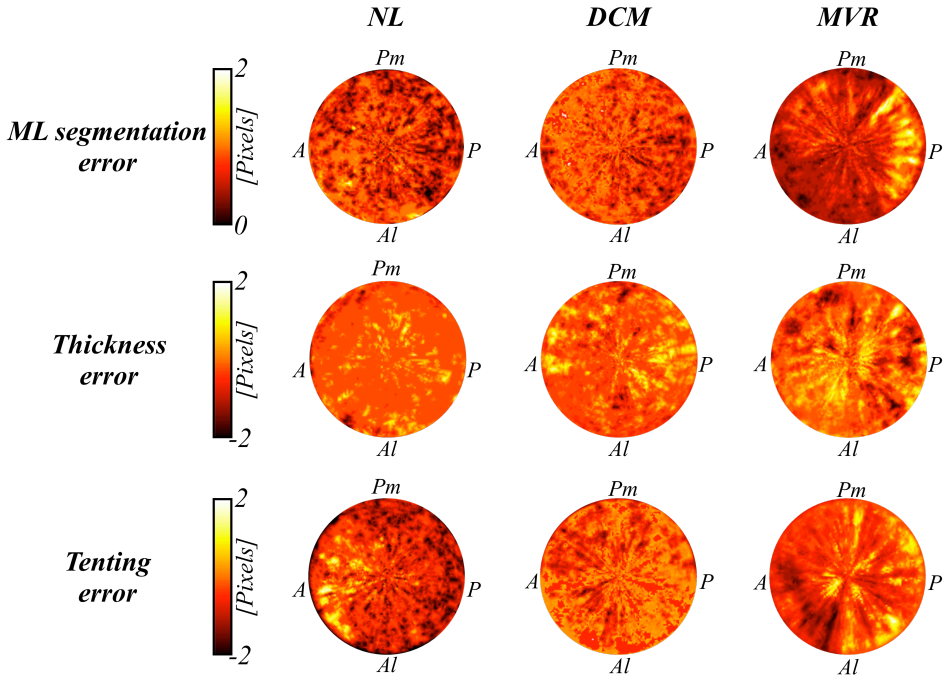

Figure 4.3. Parametric maps of regional error distribution for the ML segmentation and quantification algorithms. From left to right: NL, DCM and MVR groups; from top to bottom: ML segmentation error, thickness error and tenting error. The same color scale have been used for each variable to allow comparisons between groups.

Variable \ Group	NL	DCM	MVR
ML segmentation error (pixels)	0.7 (0.5; 0.9)	0.8 (0.6; 0.9)	0.8 (0.7; 1.1)
Thickness computation error (pixels)	-0.1 (-1.4; 1.1)	-0.1 (0.1;0.2)	0.0 (-0.1; 1.3)
Tenting computation error (pixels)	0.1 (-1.6; 1.8)	-0.2 (-0.3; 0.3)	0.2 (-1.8; 2.1)

Table 4.2. Distribution of regional errors of the ML segmentation and quantification algorithms for each of the analyzed groups. Errors are presented as median, 25% and 75% percentiles.

4.2.2 Algorithm's repeatability

Table 4.3 shows the computed inter- and intra-observer variability, both for MA and ML parameters in the *NL* group, used for this particular analysis. The proposed algorithm showed a good level of reproducibility for most of these parameters. In particular, intra-observer variability was high (CV values close to 10% and correlation coefficients higher than 0.95) for annulus perimeter, A-P and Al- Pm diameters, as well as for surface areas and mean thickness. Conversely, height, tenting volumes and maximum and average tenting heights were found as the least reproducible (CV around 20% and correlation coefficients below 0.9).

Parameter	Mean±SD	Intra-observer variability			Inter-observer variability		
		CV (%)	BA	r	CV (%)	BA	r
MA perimeter	111.1±14.3 mm	3.0±1.3	-1.1±6.7	0.97	6.0±4.8	-6.6±7.7 mm	0.93
MA A-P diameter	29.4±4.0 mm	4.0±2.4	0.6±2.4 mm	0.97	8.8±6.6	-2.4±4.5 mm	0.83
MA Al-Pm diameter	37.8±5.5 mm	3.9±2.7	0.2±3.4 mm	0.96	9.1±7.6	-3.2±6.7 mm	0.84
MA height	5.0±1.2 mm	12.1±5.4	0.2±1.6 mm	0.84	19.1±7.0	0.7±1.7 mm	0.73
MA 3D surface area	9.1±2.5 cm^2	7.4±4.6	0.4±1.9 cm^2	0.91	12.8±9.8	-1.3±2.4 cm^2	0.96
MA 2D surface area	8.6±2.5 cm^2	6.1±4.7	0.2±1.5 cm^2	0.95	11.8±7.2	1.1±2.0 cm^2	0.97
ML 3D surface area	13.5±3.0 cm^2	8.1±3.8	-0.2±2.8 cm^2	0.88	13.5±9.3	-1.9±2.8 cm^2	0.90
ML mean thickness	2.6±0.9 mm	3.5±2.6	0.1±0.2 mm	1.00	6.4±5.8	-0.2±0.5 mm	0.99
ML mean tenting	1.6±0.5 mm	11.1±8.9	0.1±0.5 mm	0.88	16.8±7.6	0.2±0.7 mm	0.82
ML mean curvedness	0.9±0.2	2.8±1.3	0.1±0.1	0.98	5.8±2.2	0.4±0.2	0.94
MV tenting volume	1.3±0.2 ml	11.5±6.3	0.1±0.3 ml	0.75	17.3±7.3	-0.2±0.3 ml	0.89
ML max. tenting height	5.0±0.9 mm	9.4±13.5	-0.1±1.5 mm	0.74	18.0±9.9	0.3±2.2 mm	0.81

Table 4.3. Results of the reproducibility analysis for the measured MV morphological parameters. Mean value of the two observers is reported, together with the coefficient of variation (CV), bias ± 2SD from Bland-Altman analysis (BA) and Pearson correlation coefficient (r).

4.2.3 Comparison with "gold standard"

In this step, the proposed method was compared against the parameters obtained in QLAB using a completely manual segmentation approach (sec. 3.1.3) and performed by an expert cardiologist. Only the set of morphological parameters available in both tools was used for comparisons.

Fig. 4.4 shows the kind of 3D surface reconstructions available from each tool. In addition, Table 4.4 lists the results of the comparison with the "gold standard". Optimal correlation, very small biases and narrow limits of agreement were found in all parameters except for the MA height, were the lowest accuracy, as shown by wide limits of agreement (±38.2%) and low *r* value (0.74) was achieved.

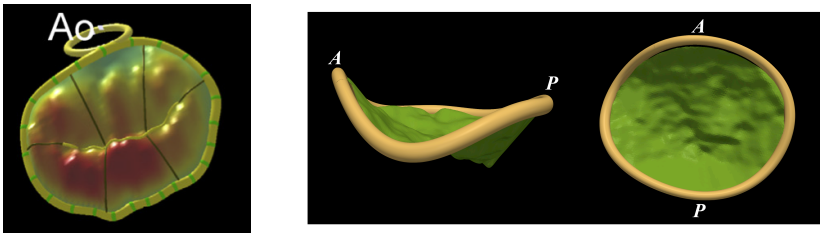

Figure 4.4. Surface reconstructions of the MA and ML obtained from QLAB (left) and with the proposed method (right). Ao: aortic valve, A: anterior annular portion, P: posterior annular portion.

Parameter	Bland-Altman analysis		Linear regression		
	Bias	CI	m	b	r
MA perimeter	-1.4 (1.3%) mm	±8.0 (±7.2%) mm	0.99	-0.7	0.97
MA A-P diameter	2.2 (7.6%) mm	±4.0 (±14.0%) mm	0.89	5.07	0.93
MA Al-Pm diameter	-0.02 (0.07%) mm	±4.4 (±11.9%) mm	0.85	5.45	0.93
MA height	-0.2 (3.3%) mm	±2.2 (±38.2%) mm	0.93	0.18	0.74
MA 3D surface	0.2 (2.0%) cm^2	±1.7 (±18.1%) cm^2	0.94	0.70	0.96
MA 2D surface	-0.13 (1.4%) cm^2	±1.6 (±17.9%) cm^2	0.91	0.64	0.96
ML 3D surface	2.8 (13.2%) cm^2	±1.7 (±14.0%) cm^2	1.07	2.09	0.98

Table 4.4. Results of the comparison with the "gold standard". Values between parenthesis represent the percentage of the mean. Bias was computed as the difference between the measured value and the gold standard.

4.3 Validation using porcine specimens

4.3.1 Population and validation protocol

A set of seven excised porcine hearts, previously defrozen, was used to compare the results of MA quantification with a commercial tool and to further assess the reproducibility of the algorithm also when a different imaging approach other than transesophageal is performed [97].

To do so, a test bench implemented by Leopaldi et al. [98] and able to house an entire explanted porcine heart, was used to replicate the *in vivo* hemodynamics (Fig. 4.5). This system allows the acquisition of video recordings of the valves with endoscopic and echocardiographic techniques, via epicardial approach, and includes three main components: a computer-controlled pulse duplicator, a simulator of the hydraulic input impedance of the systemic circulation and a preload reservoir. These components allow emulating different heart rates and systolic/diastolic pressure conditions.

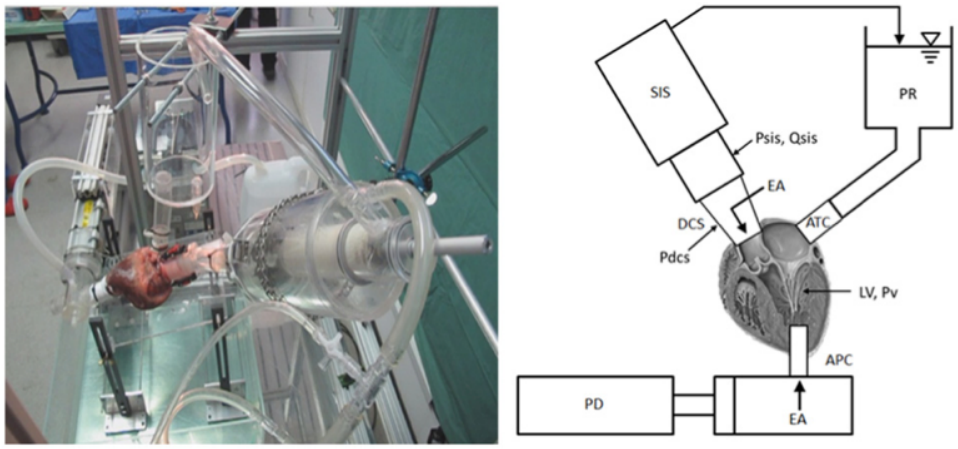

Figure 4.5. Test bench used for the acquisition of 3DE datasets from excised porcine hearts. Left: photography of the system. Right: schematic of the test bench: pulse duplicator (PD), systemic impedance simulator (SIS), preload reservoir (PR), apical connector (APC), atrial connector (ATC), double cone system (DCS), endoscopic accesses (EA). (image taken from Leopaldi et al.[98]*)*

3DE datasets were acquired with an iE33 system (Philips Medical Systems, Andover, MA) using both the X-7 (pediatric) and the X-5 (3D) transducers, from an epicardial approach. For each of the excised hearts, several acquisitions were performed, and only the end-systolic frames with the best quality (i.e., completely depicting the MV and with reduced presence of artifacts) were considered. In the end, a total of 42 volumes, with resolutions ranging from 0.3 to 0.6 mm, were used for the validation of the MA segmentation algorithm described in Sec. 3.3. An example image of the acquired datasets is shown in Fig. 4.6.

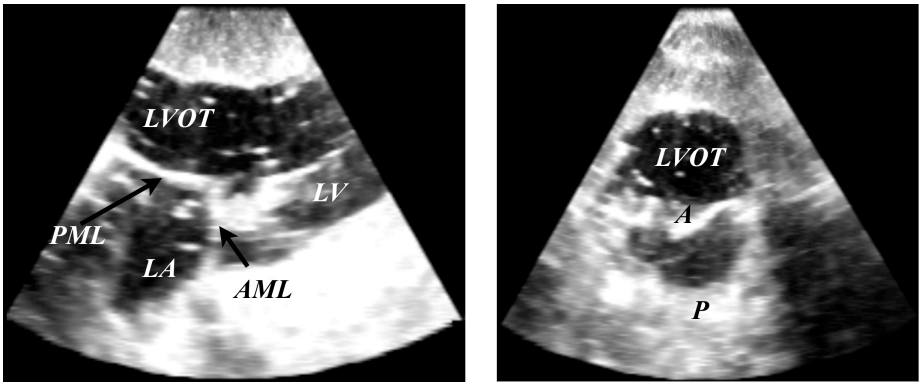

Figure 4.6. Two cut-planes of a 3DE image acquired from one of the porcine specimens used in the experiments. LA: left atrium; LV: left ventricle; LVOT: left ventricular outflow tract; AML: anterior mitral leaflet; PML: posterior mitral leaflet; A: anterior annular region; P: posterior annular region.

Comparisons were made using as reference the MA parameters obtained using a modified research version of the QLAB software (Philips), capable of analyzing also not 3DTEE datasets. For each of the 42 volumes, the same expert conducted the analysis with both tools, manually tracing the MA (using QLAB), and initializing the MA segmentation algorithm (9 points). This procedure was repeated three times, thus obtaining three measures for each dataset, for a total of 126 measures using each software.

The following set of MA morphological parameters, available in both tools, was used for comparisons (Sec. 3.3.7):

- MA perimeter
- A-P diameter
- Al-Pm diameter
- MA height
- MA projected 2D area

Comparisons were performed by applying linear regression (and the Pearson correlation coefficient r) and Bland-Altman analyses. The reproducibility in the quantification of the morphological parameters, for each of the two tools, was assessed in terms of intra-observer variability, using the last two measurements made by the expert. As with the human datasets, this level of reproducibility was measured using the coefficient of variability.

4.3.2 Results

The intra-observer variability analysis of the porcine hearts is summarized in Table 4.5. Both tools exhibited comparable levels of reproducibility, with most of the computed MA parameters having CV below 7%, except for the MA height which, as in the assessment of human valves, had a high level of variability (14.3% with the proposed approach and 22.3% with QLAB).

Parameter	Mean±SD	CV(%) QLAB	CV(%) proposed approach
MA perimeter	125.7±20.3 mm	3.9±1.2	3.2±0.6
MA A-P diameter	27.1±5.3 mm	4.1±0.5	3.8±1.5
MA Al-Pm diameter	36.1±4.3 mm	3.6±0.8	3.4±1.8
MA height	4.6±1.6 mm	22.3±2.5	14.3±3.2
MA 2D surface area	9.1±3.8 cm^2	7.0±1.2	6.8±1.8

Table 4.5. Results of the reproducibility (inter-observer) analysis on each tool for the measured MA morphological parameters in the porcine hearts.

Table 4.6 shows the results of the linear regression and Bland-Altman analyses (using QLAB as reference) applied for comparing both tools in the porcine hearts. Most of the measurements were highly correlated, with Pearson coefficients close to 0.9 and low biases (below 3% of the corresponding parameter). The only exception, as with the intra-observer variability, was the MA height, exhibiting low correlation levels (Pearson coefficient of 0.45) and high biases (close to 67% of the average MA height).

Parameter	Mean±SD	r	BA
MA perimeter	125.7±20.3 mm	0.92	1.5±8.6 mm
MA A-P diameter	27.1±5.3 mm	0.96	0.9±3.6 mm
MA Al-Pm diameter	36.1±4.3 mm	0.94	1.1±3.6 mm
MA height	4.6±1.6 mm	0.45	-3.1±3.2 mm
MA 2D surface	9.1±3.8 cm^2	0.87	1.5±2.8 cm^2

Table 4.6. Linear regression and Bland-Altman analyses results, when comparing the proposed approach vs. QLAB. The Pearson correlation coefficient (r) and the bias±2SD of the Bland-Altman analysis are reported.

4.4 Discussion

The proposed algorithm resulted in the quantification of MA and ML morphological parameters in approximately one fifth of the time needed by other conventional software (Philips' QLab MVQ module [20]). Moreover, novel parameters such as local leaflet thickness and local tenting, not available in other existing (custom-based or commercial) software, were reliably quantified.

The dense angular sampling of the 3D volume used for constructing the set of radial 2D cut-planes (5º apart) ensures a high degree of spatial correlation between adjacent slices, thus adding robustness to the MA segmentation. Moreover, the use of WNCC together with the JE image improves the 3D spatial reconstruction of the MA, overcoming the limitations of WNCC alone (high sensitivity to small disturbances and cumulative errors). This can be confirmed by the relatively low median errors in the detection of MA and ML (1.1 and 0.8 pixels, respectively).

The use of the parametric maps of median errors applied to the validation of regional thickness and tenting height parameters allowed to evidence minimal signed errors, with local positive errors (between 1 and 2 pixels) in tenting height towards the anterior region for the *NL* group, probably due to the fact that these datasets were acquired with the worst spatial resolution (close to 1.0 mm), compared to the other groups, which affects the selection of initialization points in the anterior annular region. Thus, local errors in both segmentations of MA and ML affect cumulatively the tenting height computation. Also higher signed errors, both for thickness and tenting computations, were observed toward the posterior region in *MVR*, which can be explained by the presence of the implanted ring and in particular for the location of suture points in the ML surface.

Except for these local inhomogeneities, the error distribution is almost uniform around the positive and negative values, thus implying that there is not systematic bias toward under or over-estimation of the computed parameters.

When compared with previous semi-automated image-based approaches [24] [23], the proposed method overcomes some of the existing limitations. In particular, after initialization the leaflet thickness is computed from the set of initialized cut-planes, which allows obtaining the JE image without any predefined thickness value. When combined with the WNCC and the 8 user-defined points, the Dijkstra algorithm allows the correct segmentation of the MA even in the anterior annular region. This improves what developed by Schneider et al. [24] and Pouch et al. [23], where a fixed thickness value was required during segmentation, limiting the clinical applicability.

Another advantage of the proposed method is related to the orientation of the MV within the acquired volume: the definition of one point in the LA cavity during the initialization allows the segmentation of valves in virtually any orientation within the pyramidal 3DE dataset. In previous studies[23], proper orientation of the MV apparatus inside the acquired dataset (i.e., parallel to one of the volume's main axes) was a pre-requisite for the segmentation to be applicable.

In the present implementation, the only constraints in the MA segmentation are the ROS and ROI sizes (which in spite of imposing a curvature constraint in the curvature of the segmented MA, still allow reduced segmentation errors, below 2 pixels, as seen on Sec. 3.4.3) and the connectivity in the detection of 3D annular points, whereas ML segmentation relies on 2D graph connectivity: this resulted in adequate patient-specific segmentations both in normal and pathologic patients. In contrast, previous model-based approaches [26],[29], [28], [30], [34] had the advantage of computing the MV configuration during the complete cardiac cycle (from diastole to systole), but with the drawback of using geometrical, morphological or mechanical priors. Also, in these approaches the computation of the ML surface during systole from a limited set of anatomical landmarks led to inaccurate estimation and reported errors ranged from 2 to 5 mm, which is higher than current 3DE resolutions (of the order of 0.3 to 1 mm) and comparable with the ML thickness or tenting heights.

Conversely, although in the proposed approach the initialization procedure seems cumbersome (with 9 points required for achieving MA segmentation and additional 4-6 for CL and ML differentiation), the results suggest a more precise delineation of MA and ML when compared with previous approaches[26],[29], [28], [30], [34], although it is important to mention that given the lack of a standard database, the datasets used on each validation were different. In particular, for the considered higher voxel size (1 mm), median errors of 1.1 mm (25% and 75% percentiles of 1mm and 2mm) were achieved for MA segmentation and of 0.8 mm (25% and 75% percentiles of 0.25 mm and 1.2 mm) for ML segmentation. A trade between the algorithm accuracy and the complexity of initialization step becomes evident: a simpler initialization procedure or a completely automated method results in less accurate and reliable quantification of the MA and ML morphology; if such approaches are to improve their accuracy, a heavier user interaction will be required.

As regards the repeatability of the analysis performed on human populations, the results showed a good inter and intra-operator reproducibility, except for the annular height and the maximum and mean tenting heights. Similar results were obtained when assessing the porcine hearts dataset: in this case the lowest reproducibility was obtained for the MA height, with the coefficient of variability of QLAB being higher than that of the proposed approach (22.3% vs. 14.3%, Table 4.5), which can be explained by the user intensive interaction required by this tool (a completely manual approach). The reported high variability in the computed annular height is in agreement with Maffessanti et al. [99], where repeatability of the manual measurements was investigated in a cohort of 15 patients with degenerative mitral valve disease; in that work the MA height was found to be the most variable parameter (inter-observer: 17.2%; intra-observer: 11.5%). The level of intrinsic variability in this parameter is probably related to the spatial resolution of the

acquired image, which in case of 1 mm resolution represents up to the 20% of the mean annular height value.

Finally, referring to Tables 4.4 and 4.6, it can be concluded that MA quantification given by the algorithm presented in Sec. 3.3 is comparable, and even superior, to that provided by QLAB. In particular, lower coefficients of variability were observed in the proposed method; this stresses the usefulness of the semi-automated approach since the simpler initialization (of only 9 points) reduces the user-dependency (and thus the variability of the algorithm) and in addition ensures that a complete characterization of both MA and ML can be achieved in less time (2.5 min vs. approximately 10 min with QLAB).

Chapter 5

Clinical application of the algorithm for the morphological quantification of MA and ML

In this chapter, two applications of the developed algorithms using clinical data are described, both focused on the regional characterization of the ML surface.

5.1 Characterization of valves with ML abnormalities

The aim of this sub-study was to use the regional thickness computation algorithm to locate the presence of abnormalities in the ML surface. To do so, 3DTEE images obtained in two small groups of patients were studied:

1) Three patients with mitral leaflet perforation resulting from bacterial endocarditis;
2) Two patients with mitral leaflet malcoaptation;

Figure 5.1 shows the 3D volume rendering (top) of the 3DTEE data and the corresponding 3D mesh (bottom) with leaflets thickness superimposed as a parametric color map, for the three patients with leaflet perforation (Fig. 5.1 a-c) and the two patients with leaflets malcoaptation (Fig. 5.1 d-e). It is possible to notice the direct match between the location of the perforation/malcoaptation, highlighted in the rendered volumes, and the corresponding zero-thickness regions (gray spots in Fig. 5.1, bottom) in the parametric images.

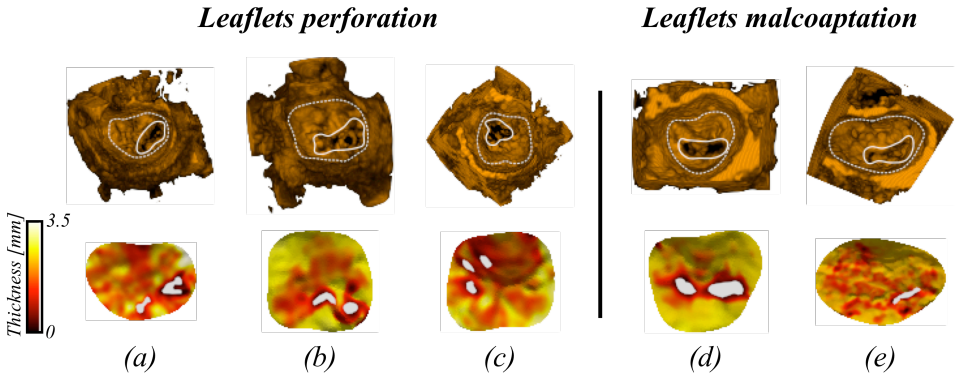

Figure 5.1. MV 3D volume renderings (top) and 3D representations (bottom) for patients with leaflets perforations (a-c) and malcoaptation (d, e). The dashed and continuous contours in the rendered volumes represent the approximate locations of the MV and abnormalities, whereas the color scale on the left is the same for all representations. Black continuous lines in the 3D representations correspond to the location of the CL.

5.2 Characterization of global and regional MA and ML morphology in different patients populations

In this sub-study, the information present in the 3DE datasets is fully exploited and used to study morphological differences in the MV configuration of the *NL*, *DCM* and *MVR* groups, previously mentioned in section 4.1.

In particular, global parameters as well as median parametric maps depicting the distribution of regional thickness, tenting and curvedness were obtained for each group. To test for morphological differences, the Mann-Whitney U test was applied, considering *NL* as the control group. In addition, to test for differences between the anterior and posterior ML for each group, the Wilcoxon signed-rank test was applied. In both cases, differences were considered significant for $P<0.05$.

Figure 5.2 shows an example of the distribution of the regional parameters along the leaflets in one patient from each group, where on each rendered surface, represented in its own original dimensions, the color map (from blue to red, low to high values) is associated to the corresponding thickness, tenting and curvedness regional distributions, and the position of the CL is superimposed. When compared with the NL subject, MV dilation is evidenced in the DCM patient (second column in Fig. 5.2) whereas reduction in annular size can be observed for the MVR patient (last column in Fig. 5.2). Low thickness distributions (between 1.0 and 1.8 mm) were found for NL and MVR patients, in particular toward the CL; on the contrary the DCM patient exhibited an inhomogeneous regional pattern of thickness distribution, with thicker regions (of approximately 3.0 mm) closer to the CL. An almost symmetric pattern of tenting was observed in the NL patient, both in the A-P and Al-Pm directions, with the MVR patient exhibiting a similar behavior but with a higher range of values (with global maximum near 6.1 mm); in contrast, the DCM patient showed both a more asymmetric distribution, oriented toward the Pm annular region, and more pronounced tenting values (around 5.8 mm). The curvedness distribution showed lower values for the NL patient (between 0.0 and 0.4), with the DCM and MVR patients exhibiting comparable ranges of values (between 0.0 and 1.0); in addition the local curvedness pattern in the NL subject evidenced a higher concentration of values near the free edge of the A ML, whereas the DCM curvedness values are shifted toward higher values with the high curvedness regions being also larger when compared with the NL subject; there is an apparent stretching of ML surface in the MVR patient, evidenced by the non-uniform distribution of high curvature regions (red spots in the corresponding pattern of Fig. 5.2), probably related with the presence of the implanted ring.

Table 5.1 summarizes the resulting MV morphological parameters in the three groups. Using *NL* as reference, a trend of increase in all parameters, except the MA height, was found in *DCM*, with statistical significance in MA perimeter, ML tenting volume, anterior and posterior ML surface areas and CL length. On the contrary, a trend of reduction in almost all the measurements (except for the tenting volume) was observed in *MVR*, with significant differences in MA height and anterior and posterior ML surface areas).

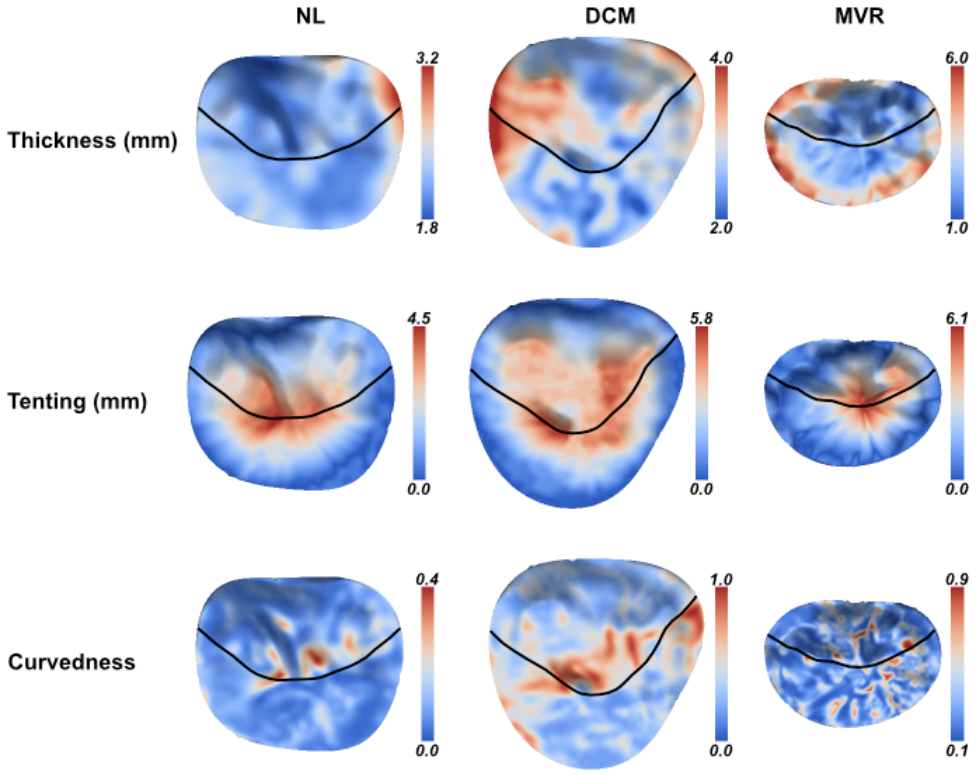

Figure 5.2. MV 3D representations with regional distribution of thickness, tenting and curvedness for a subject in the NL, DCM and MVR groups. Each 3D surface is represented as the atrial surgical view (i.e. with A annular region on top) and have been scaled so as to depict the difference in MV dimensions between populations. The black continuous line on each rendered valve represents the location of the CL.

Parameter	NL	DCM	MVR
Mitral annulus			
Perimeter (mm)	112.0 (99.7; 126.0)	121.6 (113.6; 129.4)*	102.1 (96.4; 109.7)
A-P diameter (mm)	31.4 (28.0; 33.4)	34.1 (30.7; 38.8)	26.1 (24.8; 27.9)
Al-Pm diameter (mm)	36.8 (33.1; 42.2)	38.0 (35.7; 43.1)	34.8 (32.2; 38.7)
Height (mm)	5.5 (4.8; 6.5)	5.1 (3.8; 7.2)	4.4 (4.3; 4.7)*
3D surface area (cm^2)	9.4 (7.4; 11.7)	10.4 (9.8; 12.8)	7.8 (6.9; 8.6)
2D area (cm^2)	9.2 (7.2; 11.3)	10.2 (9.7; 12.4)	7.6 (6.7; 8.5)
Mitral leaflets			
Tenting volume (ml)	1.4 (1.3; 2.1)	3.0 (2.4; 4.3)*	1.6 (1.3; 2.1)
A ML 3D surface area (cm^2)	5.5 (4.1; 6.6)	7.6 (5.5; 8.3)*	4.4 (3.9; 5.1)*
P ML 3D surface area (cm^2)	4.7 (4.2; 6.3)	5.9 (5.2; 7.3)*	4.0 (3.2; 4.5)*
Coaptation			
Length (mm)	48.0 (44.6; 56.8)	58.7 (53.1; 62.0)*	46.8 (44.9; 49.6)

**P<0.05 vs. NL, Mann-Whitney U test.*

Table 5.1. Computed parameters expressed as median (25-th; 75-th percentiles) for the morphologic characterization of mitral annulus and leaflets in control subjects (NL), patients with dilated cardiomyopathy (DCM) and patients after mitral valve repair with annuloplasty (MVR).

To allow visual comparison of the characteristic regional distribution for each parameter in each group, and also to take into account differences in size and morphology, a circular parametric map was obtained for each patient through a remapping operation onto a unit disk, from which a final parametric image reflecting the median value over the group at each position was computed (recall Fig. 4.1 in the previous chapter). The same procedure was applied to derive the average location of the coaptation line for each group.

In Fig. 5.3, the thickness pattern exhibits higher values for the *MVR* group, followed by the *DCM* and *NL* groups. In the *NL* group, this distribution was lower for the central portion of the anterior *ML*, whereas its free edge and the posterior ML had higher

values. A generalized nonuniform thickening of both ML was observed in *DCM*, even in regions far from the anterior ML's free edge; the *MVR* featured similar patterns when compared with *NL* (i.e., a thinner anterior ML central portion and a thicker free edge and posterior ML), except for the presence of suture points located around most of the posterior ML (Fig. 5.3c).

The tenting distribution was characterized by higher values in *MVR*, followed by the *DCM* and *NL* groups. The pattern in *NL* and *MVR* was more symmetrical along the A-P and Al-Pm axes, whereas in the *DCM* higher tenting values (red colored in Fig. 5.3e) were observed toward the Pm region of the corresponding renderings.

As regards curvedness, the *NL* and *MVR* groups (Figs. 5.3g and 5.3i) showed more uniform distributions and were more curved toward the center of the CL; on the contrary a wider range and a more inhomogeneous pattern was observed in *DCM* (Fig. 5.3h).

Finally, the average location of CL (black continuous lines in Fig. 5.3) is almost centered along the A-P axis for the *NL* and *MVR* groups, whereas in *DCM* it was closer to the P annular location.

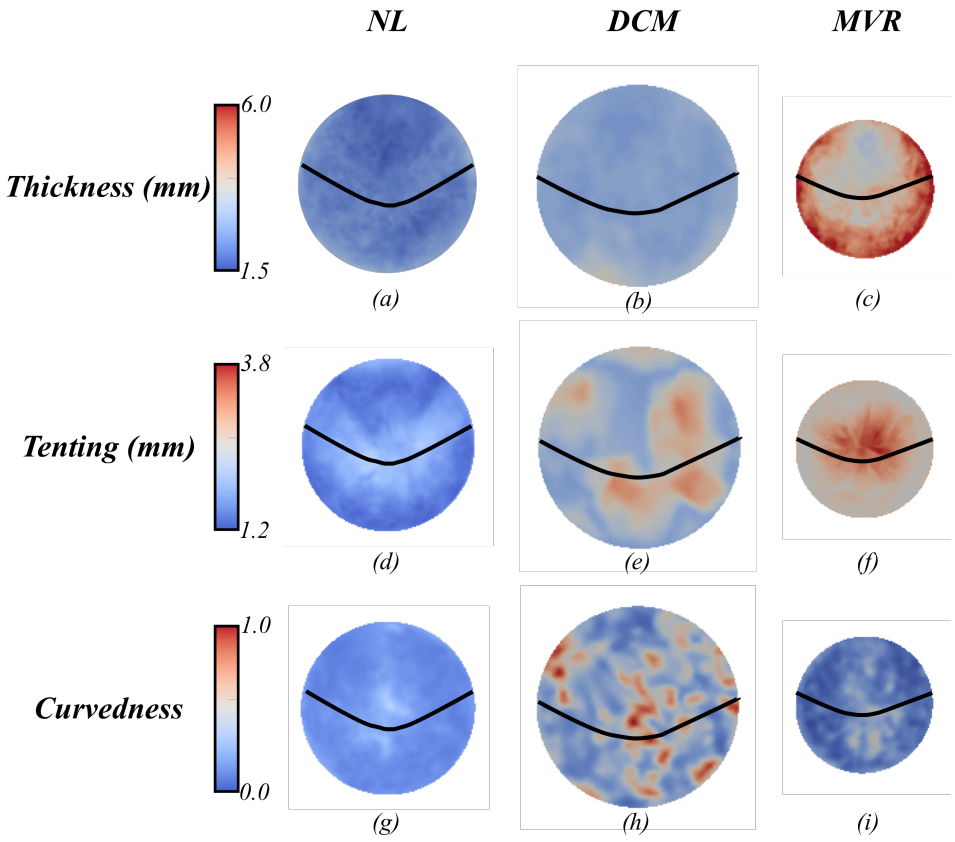

Figure 5.3. MV parametric maps for the median regional distribution of thickness, tenting and curvedness for the NL, DCM and MVR groups. Maps are presented as the atrial surgical view (i.e. with anterior annular region on top) and have been scaled so as to depict the difference in MV dimensions between groups. The black continuous line on each map represents the average location of the CL. The same color scale have been used for each variable to allow comparisons between groups.

Table 5.2 summarizes the findings of Fig. 5.3. Values for the median and percentile range distributions of regional thickness, tenting and curvedness, computed over the mitral leaflets, separately for the anterior and posterior portions are presented. When compared to controls, in *DCM* a higher tenting and curvedness was found in both anterior and posterior ML, together with an increased thickness in the anterior leaflet. In

MVR, an increased thickness and tenting was found in both leaflets, while curvedness did not change. When comparing the measurements obtained separately for each leaflet, it is possible to observe (referred to the anterior leaflet):

1) A thicker and less tethered posterior leaflet with comparable curvedness values in the *NL* group
2) A lower thickness and tenting of the posterior leaflet associated to slightly higher curvedness values in the *DCM* group
3) Lower tenting and slightly higher curvedness in the posterior leaflet, with no difference in thickness, in the *MVR* group.

Regional parameter	*NL*		*DCM*		*MVR*	
	A ML	***P ML***	***A ML***	***P ML***	***A ML***	***P ML***
Thickness (mm)	2.5 (2.4; 2.8)	2.9 (2.8; 3.1)†	3.6 (3.1; 3.8)*	3.2 (2.9; 3.4)†	4.1 (3.4; 5.7)*	5.9 (4.6; 6.7)*
Tenting (mm)	1.8 (1.6; 2.0)	1.6 (1.4; 1.8)†	3.2 (2.4; 4.5)*	2.5 (1.9; 3.1)*†	3.3 (2.9; 3.9)*	3.0 (2.6; 3.6)*†
Curvedness (adimensional)	0.4 (0.0; 0.5)	0.4 (0.1; 0.6)	0.8 (0.2; 1.0)*	1.0 (0.1; 1.0) *†	0.5 (0.1; 0.6)	0.6 (0.0; 0.7)†

**P<0.05 vs. NL, Mann-Whitney U test.*
†P<0.05 P vs. A, Wilcoxon signed-rank test.

Table 5.2. Regional distribution of anterior (A) and posterior (L) leaflets, expressed as median (25-th; 75-th percentiles) in control subjects (NL), patients with dilated cardiomyopathy (DCM) and patients after mitral valve repair with annuloplasty (MVR)

The spatial configuration of the tenting pattern is further explored in Fig. 5.4, where the distribution of tenting heights along the CL (from Al to Pm region) for the *DCM* and *MVR* groups is plotted, using *NL* group as reference. Although statistically significant differences were found only for the minority of computed points, local tenting values were more pronounced in *DCM* and *MVR* groups when compared with controls; also an almost symmetric distribution can be observed for the *NL* and *MVR* groups (centered around 50% of the CL total extension), whereas the distribution for the *DCM* patients is biased toward the right side of the plot.

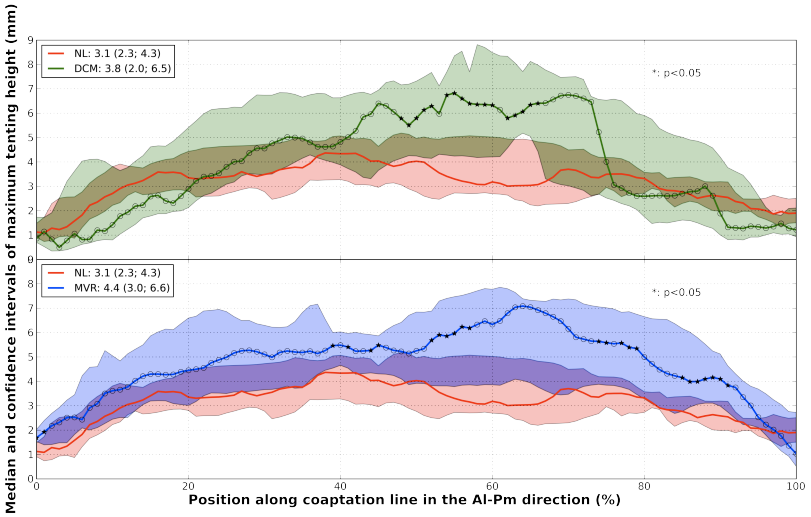

Figure 5.4. Distribution of regional tenting heights through the coaptation line for each of the studied populations. Values depicted on each legend correspond to the median, 25% and 75% percentiles.

5.3 Discussion

The global and local characterization of the MV results of clinical importance, since many cardiovascular diseases (dilated cardiomyopathy, rheumatic stenosis, degenerative mitral valve disease, endocarditis, among others), as well as conventional MV surgical procedures (MVR with annuloplasty), induce morphological regional changes in the leaflets thickness and tethering. The understanding of such phenomena is

of clinical importance and might shed new lights on the remodeling processes involved in different pathologies, as well as on the effects and outcome of surgical procedures. Until now, this type of local characterization has not been fully exploited.

The computed patterns in patients with leaflet perforation and malcoaptation (Fig. 5.1) confirm the reliability of the method in computing regional thickness distribution, since it allowed a correct identification of the local defects position, visually consistent with those depicted on the rendered volumes. The potential use of this information as a clinical tool would be the automated detection and quantification of the extent of damage in case of leaflet perforation, or the estimation of the surface of the regurgitant orifice in valves with malcoaptation.

With reference to the characterization of different populations, *in vivo* regional characterization of ML thickness, tenting and curvature was possible for normal subjects and patients with dilated cardiomyopathy and after annuloplasty procedures, which evidenced the morphological differences existing between these groups.

In particular, results for the quantification of MA and ML parameters in the *NL* group (Table 5.1) are in agreement with previous studies[99-101], including the A and P ML surface areas (with the latter having reduced dimensions).

A differential distribution of regional thickness both in the anterior and posterior ML was also confirmed for the NL group: as seen in Fig. 5.3 (top row), a thinner central portion (dark blue, with values near 1.5 mm) is present in the anterior ML, whereas most of its free edge as well as the posterior ML exhibit higher thickness values (light blue regions, with values near 2.0 mm); this is consistent with previous findings[38] that described different biochemical composition on different portions of the ML.

Regarding the tenting pattern, an almost symmetrical distribution along the antero-posterior and antero-lateral/postero-medial axes of the valve was observed in the controls group, which is the result of a normal morphology and arrangement of the chordae system[42]. The uniformity in thickness and tenting distributions was also observed in the curvedness pattern (Fig. 5.3g); lower median curvedness distributions near the MA (close to 0.0) were noticeable, with values increasing following a concentric pattern until they reach their maximum near the center of the ML surface (corresponding to the red-colored regions, with curvedness values close to 0.4). This pattern confirms the ML billowing described by Salgo et al[102], which reduces leaflet stress during valve closing[31], [102].

In the *DCM* group, as expected, enlarged MA and ML dimensions were obtained when compared with *NL*. In particular, significant differences were found for MA perimeter, tenting volume and ML surfaces, thus confirming the elongation of the ML surface as a result of global LV remodeling, as described previously by other authors[35]. In addition, the computed regional patterns of thickness, tenting and curvedness were completely asymmetrical when compared with *NL*. Thickening of both ML can be observed in Fig. 5.3b, with the anterior ML being thinner than the posterior. In addition, these changes in regional thickness induced by ML remodeling are not uniform, since thinner regions (colored in dark blue, with thickness of approximately 2.5 mm) are randomly distributed along the ML surface. Regarding the tenting distribution, higher values (in red color) appear closer to the postero-medial annular portion, an effect that derives from the asymmetrical displacement of papillary muscles in presence of global ventricular dysfunction[44], [103]. Finally, the randomness in the curvedness pattern of Fig. 5.3h confirms the previous findings regarding the changes in the shape and geometry of the ML.

The assessment of global and local MA and ML in the *MVR* group evidenced significant reduced dimensions of both MA and ML when compared with the *NL* group, a result of the implantation of the annuloplasty ring which undersized the valvular dimensions to improve reverse remodeling [99]. In particular, the implanted ring reduced the MA height and the areas of both ML. The analysis of the thickness pattern evidences

an apparent increase in thickness of both ML, however we consider this more the result of MV stretching imposed by the presence of the annular ring than an effect related with the particular pathology. On the other hand, an almost normal coaptation pattern (i.e. almost centered along antero/posterior and antero-lateral/postero-medial axes) can be observed in Fig. 5.3f, which is consistent with the aim of the surgical procedure, that is the restoration of valve competency[99].

However, it is also important to mention that given the reduction of annular dimensions, much higher tenting values were present near the coaptation region (the red regions in Fig. 5.3f, and close to 3.8 mm) when compared with the *NL* group (the light blue regions in Fig. 5.3d, and close to 2.0 mm). The regional pattern of curvedness of Fig. 5.3i also confirms the effect of the implanted annulus on the ML configuration: a similar concentric distribution, when compared with controls, was observed where relatively low values were observed near the annulus and a more curved ML surface is present near the center of the valve.

As shown in the previous paragraphs, the characterization of MA and ML global and local morphology in different populations is consistent with previous works. The ability of characterizing the local morphology of the ML surface adds significant clinical value to the assessment and characterization of different populations, and also helps to understand the effect that different cardiomyopathies or surgical procedures have on the configuration and morphology of the valvular apparatus. An example of such application would be the assessment of ML thickness in patients with rheumatic stenosis, since this regional information may allow improved score computation to define the proper surgical intervention; in fact, such patients are nowadays addressed to MV replacement or percutaneous balloon dilatation (i.e., commissurotomy) based on Wilkins score [104] which includes thickness information computed from a single 2D view.

Chapter 6

Segmentation and quantification of the anatomic regurgitant orifice

In the following, a novel algorithm for the extraction of quantitative parameters in valves with mitral regurgitation (MR) is presented. The method operates on 3DE datasets and, after a simple step of user-initialization, is capable of segmenting and extracting quantitative parameters from the anatomic regurgitant orifice (ARO) 3D representation.

An overview of current clinical approaches for the quantification of the regurgitant orifice is presented, followed by a description of semi-automated methods. Then, the different considered approaches will be discussed and the final implementation of the proposed algorithm will then be described in detail, followed by its validation, a final discussion and comparison with state of the art algorithms.

6.1 State of the art: current approaches for the assessment of mitral regurgitation

Current guidelines for the quantitative assessment of MR recommend the use of 2D color Doppler flow imaging for the estimation of the vena contracta (VC), the effective regurgitant orifice area (EROA) and the regurgitant volume [62], [105].

Most of this analysis is currently carried on by the cardiologist, and the quantitative assessment of such parameters is performed in a complete manual fashion. However, some semi-automated approaches aiming at reducing user-dependency have also been proposed.

In this section, two approaches will be described an analyzed in detail, both aimed at segmenting the regurgitant orifice from 3DE datasets.

6.1.1 Manual assessment

Currently, the estimation of the size of the anatomical regurgitant orifice in patients with MR is performed using color Doppler imaging, with the VC and the EROA being the most used parameters.

The VC is defined as the narrowest portion of the regurgitant jet (Fig. 6.1, white arrows) and in the clinical settings it is measured as a diameter, obtained from a 2D cut-plane perpendicular to the commissural line. The measurements are repeated over at least two to three beats to improve accuracy, and the average of these measurements is reported as the VC diameter[105]. A VC of less than 3 mm indicates mild MR, whereas a diameter greater than 7 mm defines severe MR[3]. Intermediate values (from 3 to 7 mm) do not allow to distinguish moderate from mild or severe MR, and other methods (such as quantification of EROA or regurgitant volume) are required for confirmation[105].

On the other hand, the EROA is an indirect measure of the size of the anatomical regurgitant orifice. Its quantification relies on the proximal flow convergence principle (Sec. 2.3), which postulates that when an incompressible fluid (such as the blood) passes

through a small orifice (the regurgitant orifice) the flow accelerates near to the orifice and converges as a hemispheric shell.

By determining the radius of this 3D surface (Fig. 6.1, in red) and applying the continuity equation, an estimation of the area of the regurgitant orifice (the EROA) can be obtained.

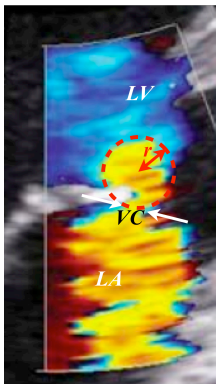

Figure 6.1. A 2D color Doppler image showing a regurgitant jet (yellow) from the left ventricle (LV) into the left atrium (LA). The approximate location of the VC is depicted with white arrows, whereas the proximal isovelocity surface and its radius are depicted in red. (image modified from Lancelloti et al. [105]*)*

In spite of being currently used in clinics for the MR severity assessment, several pitfalls and limitations make the quantification of VC diameter and EROA from 2D color Doppler highly unreliable. The first drawback is the intrinsic 3D nature of the regurgitant jet and of the orifice, which implies that 2D color Doppler acquisitions cannot represent adequately the geometry of the anatomical regurgitant orifice.

In fact, the use of a 2D cut-plane for the acquisition of color Doppler images assumes that the regurgitant orifice is almost circular, although, as already shown by other authors [3], [106], [107], only in a few organic MR cases this assumption remains valid, whereas in functional MR the shape of the orifice is rather elongated. As a consequence, depending on the cut-plane used for imaging the VC, it could appear broader or narrower than the correct measure. In addition, as demonstrated by Little et al. on *in vitro* experiments[108], the shape of the proximal isovelocity surface (in the flow convergence method) has a complex not-hemispheric geometry (Fig. 6.2), even when the regurgitant orifice is circular, which makes the computation of EROA using the flow convergence method an inaccurate estimation of the real size of the regurgitant orifice.

Finally, as seen in Fig. 6.1, a clear depiction of both VC and proximal isovelocity surface is not always guaranteed; user expertise and careful setting of acquisition parameters in the color Doppler imaging system are required to ensure correct visualization of these features. This implies a high level of intraobserver variability even among experienced echocardiographers[109]. In fact, in a study from Biner et al.[48] the inter-observer agreement was found modestly reliable and suboptimal for the VC and EROA measurements, with kappa coefficients of 0.28 and 0.32 respectively, thus underling the high variability and low reliability of this approach.

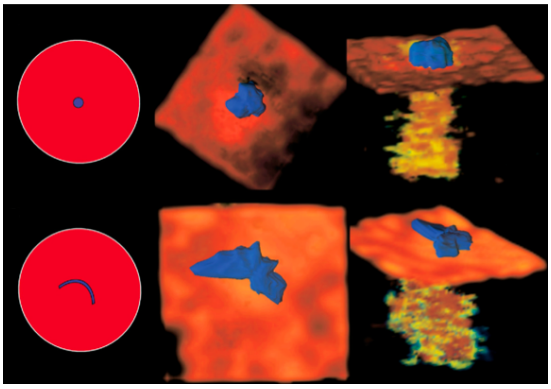

Figure 6.2. The complex geometry of the 3D proximal isovelocity surface for(a) circular and (b) arc-shaped orifices, as demonstrated by Little et al. from in vitro experiments. The center and right panels show views of the 3D surface from above and from the side. Notice the irregular shape of the surface, even when the regurgitant orifice is circular. (image taken from Little et al. [108]*)*

The recent advent of 3D color Doppler imaging alleviates some of the issues present in 2D-based quantification of MR. Using this technology, a direct planimetry approach on the 3D dataset can be implemented so as to identify the true cross-sectional area of the VC, thus obtaining a direct measure of the regurgitant orifice area[107] (instead of a 1D measure, the VC diameter, as using 2D images).

An example of this approach is the method implemented by Yosefy et al. [63], where the VC cross-sectional area was measured using 3DE datasets with 3D color Doppler flow information. By manually positioning a cross-sectional plane through the VC, and perpendicular to the jet direction, the VC area was determined using manual planimetry of the color Doppler image (Fig. 6.3). Conventional 2D VC diameter measurements as well as 3D VC areas were measured and compared with conventional 2D color Doppler EROA: in a cohort of 49 patients with MR, acceptable level of correlation between 3D VC area and 2D EROA (r^2 = 0.86) was found, whereas the 2D VC correlated poorly with the 2D EROA (r^2 = 0.61) and overestimated the size of the regurgitant orifice, thus causing clinical misclassification in 45% of patients with eccentric (elongated) regurgitant jet.

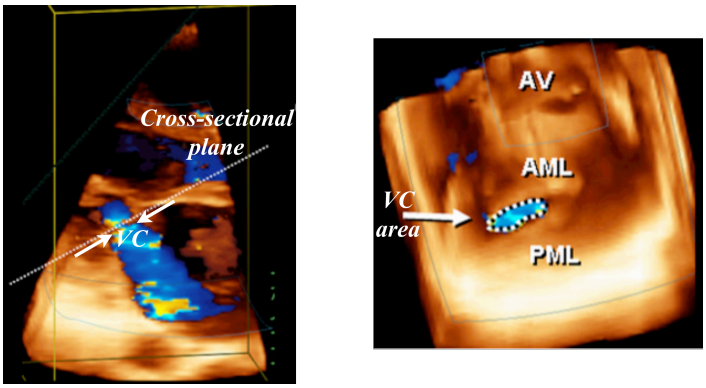

Figure 6.3. Planimetry of the 3DE dataset, with color Doppler information, to quantify the VC area. (a) The VC location and a manually defined cross-sectional plane; (b) ventricular view of the cross-sectional plane, depicting an elongated VC (AML: anterior mitral leaflet, PML: posterior mitral leaflet, AV: aortic valve) (image modified from Yosefy et al.[63]*)*

A limitation of the previous approach is that 2D color Doppler EROA was used as the gold-standard, an not accurate measure given the non-hemispherical shape of the proximal isovelocity surface. In a recent study, Shanks et al. [64]used the same approach proposed by Yosefy et al. but compared the 2D VC diameter, 2D EROA and 3D VC area with the results obtained using cardiac magnetic resonance (an approach that allows, as

with 3DE datasets, direct visualization and quantification of the regurgitant orifice). A group of 30 patients with MR was used in this study, and the results showed modest correlation between 2D VC diameter and 2D EROA (r^2 = 0.32), whereas the 2D EROA measurements significantly underestimated the size of the regurgitant orifice by 22% when compared with 3DE color Doppler planimetry and cardiac magnetic resonance. In addition, high levels of reproducibility were found for the 3DE planimetry approach: intra-observer reproducibility of 0.011 cm^2 (2.4% of the mean) and inter-observer reproducibility of 0.013 cm^2 (2.8% of the mean). The conclusions of this study also showed that using the current grading system for the MR severity (based on 2D VC and EROA measurements), one third of the patents with mild MR and over half of those with moderate and severe MR were upgraded into a more severe grade based on the 3DE color Doppler measurements.

From the previous studies it becomes evident that: (i) in spite of being two measures of the same physical variable, the VC width and the EROA 2D measurements are poorly correlated, which underlines the intrinsic limitations of these approaches; ii) 2D EROA systematically under-estimates the size of the regurgitant orifice; iii) a significant proportion of the studied patients can be misdiagnosed if the assessment of MR relies on 2D measurements only; and iv) 3D measurements of the VC area are highly reproducible.

This last statement coincides with the review of Paaladinesh et al. [110] where they suggest the use of VC area from 3DE color Doppler datasets as the preferred choice, when possible, in the assessment of patients with MR.

In spite of the apparent advantages of the 3D color Doppler planimetry approach for the estimation of the size of the regurgitant orifice, several challenges are still present:

i. The orientation of the cross-sectional cut-plane relies on the correct visualization of the VC in the 3D color Doppler image. This in turn requires off-line navigation on the 3D dataset to locate the plane containing the narrowest portion of the 3D regurgitant jet, a non trivial procedure that demands careful user interaction. In addition, the correct visualization of the VC can be affected by user and machine settings, such as color Doppler gain, and thus makes the method user dependent[106].
ii. In addition, the actual regurgitant orifice may not be completely planar and thus might not be fully contained in the cut-plane, thus leading to under-estimation of the real orifice size. Finally, color Doppler artifacts such as blooming (the apparent thickening of structures and dependant on gain settings) may lead to inaccurate estimations of the VC area[111]. Also, the acquisition of 3D color Doppler datasets is currently performed as ECG-triggered sub-volumes (>8 heart beats), thus requiring stable heart rate and longer apneas, conditions that limit its applicability in clinical practice.

Despite these limitations, it could be concluded that the preferred approach for the assessment of MR severity is 3DE with 3D color Doppler flow information. However, more accurate and reliable measurements could be obtained if the real 3D surface of the regurgitant orifice would be extracted, or if the user dependency and the effects of artifacts in 3D color Doppler imaging would be minimized or avoided.

6.1.2 Semi-automated approaches

A few computational approaches, aimed at reducing user intervention and thus obtaining more repeatable measures of the regurgitant orifice area, have been recently proposed [51], [112], [52] and [53].

In [51] and [112], Chandra et al. compute the anatomical orifice area from 3DE datasets, instead than from conventional 3D color Doppler, by obtaining an initial 3D model of the regurgitant valve using QLAB. In patients with MR, the area of leaflet mal-

coaptation corresponds to an interruption in the coaptation zone of individual parallel planes, used during manual segmentation of the ML in QLAB (Fig. 6.4a). The set of discontinuities from each 2D parallel plane conforms a 3D points cloud defining the orifice boundary in the 3D model (Fig. 6.4b), which corresponds to the anatomical regurgitant orifice. Thus, by defining a 3D, usually non-planar, contour from this set of points and computing the minimal spanning surface, the area of this regurgitant orifice can be computed. The analysis of each image in the dataset (i.e., the generation of the 3D model in QLAB and the quantification of the 3D surface area of the regurgitant orifice) required 6 min on average, and results were compared with standard 2D color Doppler EROA measurements. From a group of 61 patients (from which 38 had eccentric regurgitant jets), the results correlated well with EROA for the patients with central jets (r = 0.85) whereas for those with eccentric jets correlation was lower (r = 0.73). Intra and inter-observer variability for eccentric and central jets, measured as the coefficient of variation, were of the order of 15% and 13%, respectively.

Several limitations of this approach are present:

i. A true anatomical regurgitant orifice can be obtained only when the leaflet tips face each other (with a pattern similar to that of Fig. 6.4a); only under this assumption the 3D contour of the regurgitant orifice can be defined as the set of points corresponding to the non-coapted leaflets tips. However, this assumption is not valid in many MR patients, specially in MV prolapse: in these cases, it is usual to find overlapping leaflets (Fig. 6.4c and 6.4d), which makes difficult the definition of a non-continuous coaptation zone. This becomes evident in the 3D model of Fig. 6.4d, where a clear depiction of what would be the regurgitant orifice is difficult to visualize.
ii. A relatively low level of repeatability was reported, which can be explained by the completely manual approach required for the computation of the 3D model and delineation of the 3D contour of the regurgitant orifice. In addition, relatively high manual processing times are required which also may limit the clinical applicability of this approach.

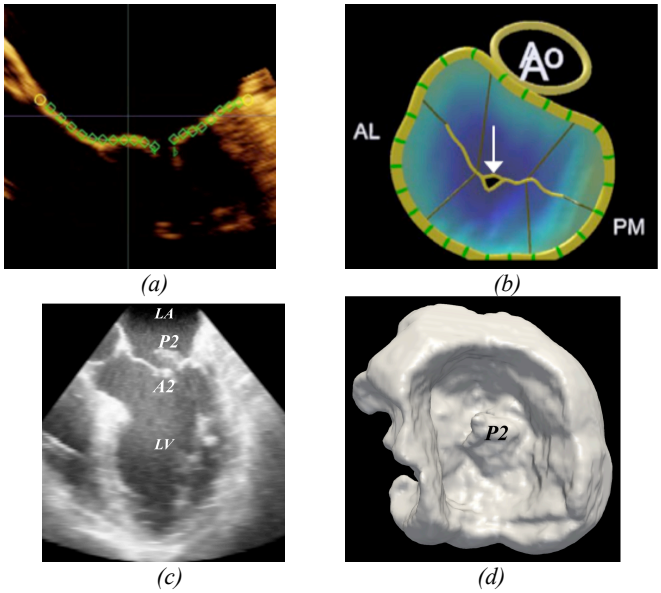

Figure 6.4. (a) A discontinuity in the coaptation zone as seen from a parallel 2D cut-plane from the 3DE dataset; notice the leaflet tips facing each other; (b) 3D reconstruction of the MV in (a) including the 3D regurgitant orifice (obtained using QLAB); (c) an example of a discontinuity in the coaptation zone where the leaflet tips are not facing each other in the 2D cut-plane (on the contrary, the P2 scallop and the A2 segment overlap); (d) atrial view of the 3D mesh model of the 3DE volume in (c), notice the prolapsed P2 scallop and the difficulty of visualizing the regurgitant orifice. (images (a) and (b) taken from Chandra et al.[112])

Conversely, Grady et al. [52] proposed a method that operates directly on the 3D color Doppler dataset. The algorithm requires 1 user-defined point to locate the MA, followed by a 3D color segmentation algorithm capable of extracting the proximal isovelocity surface (Fig. 6.5), from which the EROA can be directly computed. This algorithm eliminates the assumptions about the shape of the regurgitant orifice, since the isosurface is segmented directly from the 3D color Doppler dataset. However, custom-made hardware was required to allow sufficiently high volume rate acquisition thus ensuring reliable measurements. This last requirement, in combination with the fine setting of the acquisition parameters so as to correctly depict the regurgitant jet and the 3D isovelocity surface, constitute the main barriers for clinical acceptance and usefulness of the method.

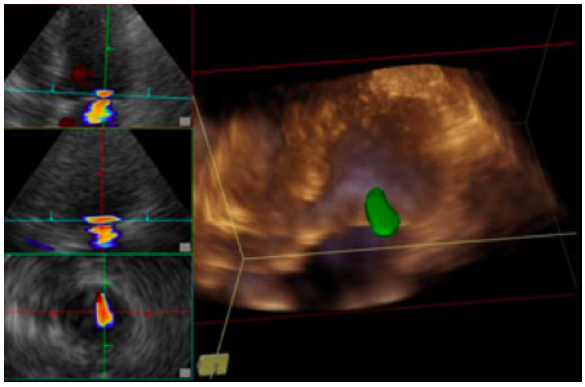

Figure 6.5. An example of a proximal isovelocity surface obtained with the method proposed by Grady et al[52].

In [53], Moraldo et al. circumvent the problem of manually estimating the radius of a shell in 2D color Doppler by measuring the rate of increase of flow velocity with distance. The estimation of this parameter is performed automatically, using 2D color image segmentation techniques, thus resulting in an automatic measure of the EROA. However, to ensure a reliable estimation, a total of 40 2D color Doppler frames per patient must me acquired. This, added to the still present fundamental weaknesses of the hemispheric flow-convergence assumptions, makes the method impractical for clinical diagnosis of MR.

Although not closely related, the works of Zhang et al. and Baloch et al. [113], [114], dealing with the semi-automated segmentation of cerebral aneurysms from 3D mesh representations, are briefly described here since some of the shape features used in their studies were also considered in the final implementation of the 3D vena contracta segmentation algorithm.

In both approaches, the aim was to differentiate the aneurysm from the adjacent vessel. To do so, several regional shape descriptors are computed on a 3D mesh representation of the aneurysm, including: Gaussian, mean, maximum and minimum principal curvatures, shape index, average geodesic distance and shape diameter function, among others (see sections 2.4.9 to 2.4.11 in Chapter 2 for the definition of these features). Subsequently, an objective energy function is appropriately defined in terms of the computed features and minimization is performed via graph-cut algorithms, with the mesh vertices belonging to the local minima representing the boundary between the aneurysm and the vessel (see Fig. 6.6). Average reported accuracies of the methods are 88.1% and 89.7% respectively.

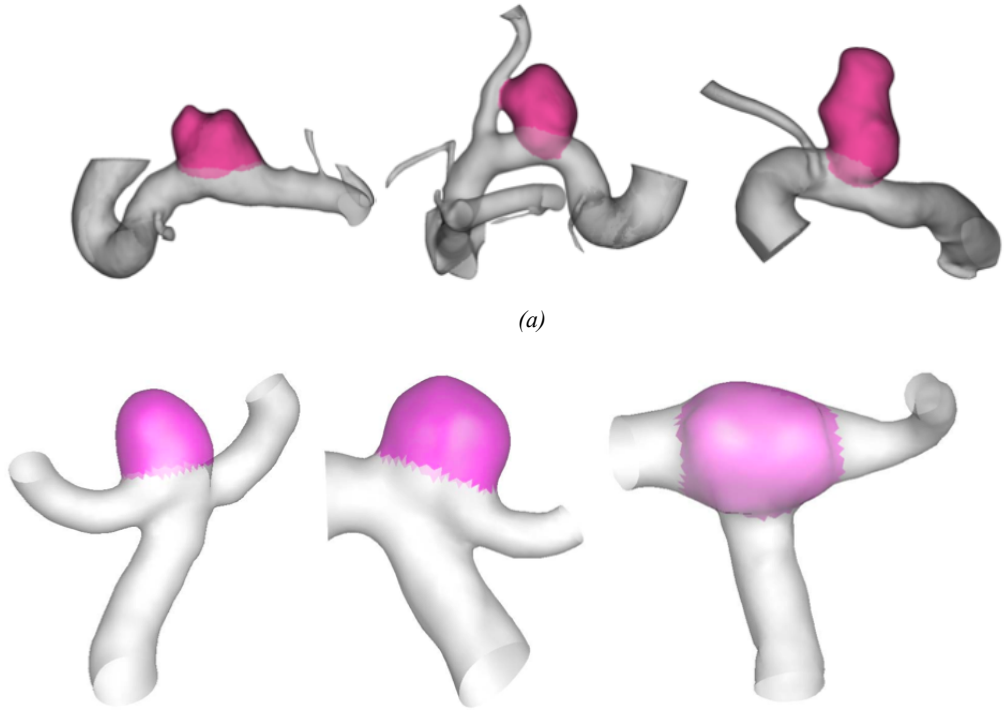

(a)

(b)

Figure 6.6. Aneurysm segmentation results from the algorithms proposed by Baloch et al. (a) and Zhang et al. (b) (images taken from [114] *and* [113]*)*

A potential limitation of both approaches lies in the high number of mesh features to be computed: 20 in [114] and almost 120 in [115], taking into account different *N-ring* neighborhoods on the mesh. Although computation times were not reported, given our own experience in the calculation of such mesh parameters we consider that an elevated number of features may lead to computation times greater than 6 minutes (in the best case scenario, with only 20 features being computed), thus limiting the applicability of these approaches. In addition, the method proposed in [114] requires the initialization of 3 user-defined points on the mesh, thus affecting its repeatability, whereas in [113] a classifier is required for correctly labeling the mesh vertices as belonging to the aneurysm or to the vessel, which in turn implies that the results will be highly dependent on the selection of the training datasets.

6.2 Preliminary solutions

Two different solutions were considered for the segmentation and detection of the ARO: in the first one, a 3D contour of the orifice was obtained by operating directly on a 3D mesh representation of the non-coapted leaflets, whereas in the second method a segmentation of the void regions in the 3DE (containing the regurgitant flow) was explored. Also from the second approach, a 3D mesh representation of the segmented void region was obtained and several mesh features were computed. These preliminary tests constituted the basis of the method that was finally implemented (that will be described in sec. 6.3) to allow the detection of the 3D ARO.

A detailed description of the two initial approaches is presented in the following paragraphs.

6.2.1 3D ARO segmentation from mesh representations of regurgitant valve

A similar approach to that proposed by Chandra et al. [51], [112], and discussed in the previous section, was considered. In this case, the goal was to simplify the required user interaction.

To do so, a 3D mesh representation of the regurgitant valve was automatically obtained by applying the same procedure described in Sec. 3.2.1: the 3DE volume was first segmented using a modified fuzzy approach and then the marching cubes algorithm was applied on the resulting 3D binary mask (an example of this first step is the Fig. 6.7, left). Then, a semi-automated segmentation of the regurgitant orifice, visible in the computed 3D mesh, was considered: first the user had to select a set of seed points (between 6 and 10, depending on the size of the orifice) located near the orifice and representing part of its contour (red points in Fig. 6.7, right). A connective path between consecutive pairs of points, constructed using Dijkstra's algorithm, would allow the delineation of the 3D contour of the ARO.

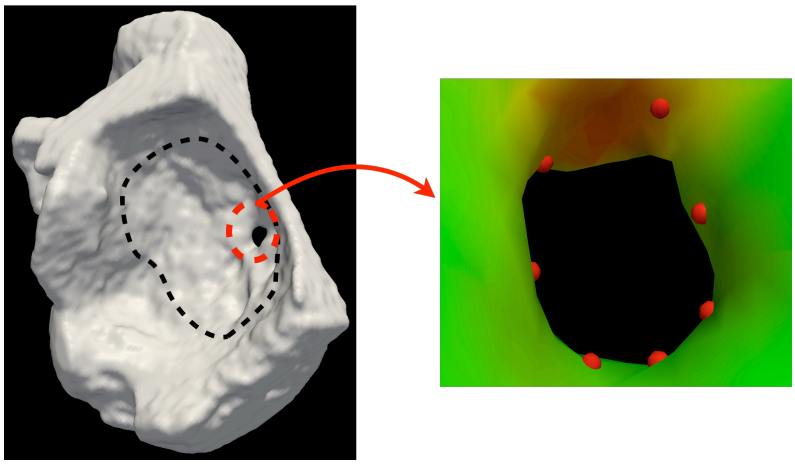

Figure 6.7. Left: atrial view of a 3D mesh corresponding to a valve with MR (the regurgitant orifice is marked with the red circle); right: a detail of the regurgitant orifice depicting the user-defined points (in red) and the concaveness scalar field aimed at enhancing regions near the leaflets tips.

Although much of the previously required user interaction was avoided with this approach (it took about 30 secs on average to initialize the set of contour points), several limitations arose:

i) Ideally the points traced manually by the user should be located on the tip of the leaflets, thus ensuring that the computed contour represents the surface corresponding to the narrowest portion traversed by the regurgitant jet (i.e., the ARO). However, this is not the case, since given only the 3D representation the user can't easily establish the corresponding location of leaflets extrema. As a result the computed contour over-estimates the real size of the ARO.

ii) To ensure the proper location of the seed points after initialization, the *concaveness* metric (Sec. 2.4.10) was used in order to enhance the regions near the tip of each leaflet. This metric was used as it is in correspondence with the tip of the leaflets, where high convexity regions can be found, coincident with the location of the ARO. However, the resulting scalar field (the *concaveness* color map superimposed on Fig. 6.7, right) was instead quite uniform thus hampering any attempt to enhance this region.

iii) Even if issues (i) and (ii) were overcome, the method would only result appropriate for valves where the leaflet tips face each other (recall Fig. 6.4a);

as mentioned previously (and also as seen in Fig. 6.4c), in prolapsed leaflets this requirement is not satisfied.

Given the previous limitations, a different approach aimed at segmenting the regions near the 3D ARO was implemented. This method is described below.

6.2.2 Segmentation of regions located near the 3D ARO

Given the limitations discussed in the previous section, and the fact that the ARO is by definition a measure derived from the shape of the regurgitant jet, instead of the particular configuration of the leaflets, a different approach was considered. Instead of segmenting the tissue (i.e. the leaflets, annulus and surrounding structures), an initial segmentation was directly obtained from the 3DE volume's void regions corresponding to the lower (almost black) intensity voxels that contain the regurgitant flow.

A completely automated approach is not useful in this case, since only regions near the regurgitant orifice are of importance: these regions contain the regurgitant orifice, and no knowledge of the complete morphology of both atrial and ventricular cavities is required. A user-guided segmentation using active contours was preferred (see Sec. 2.4.5 and the works of Zhu and Yuille[72] and Yushkevich et al.[73]), where user interaction is required in two stages of the algorithm: for the definition of a *probability map* that controls balloon evolution (and that corresponds to an intensity transformation of the original 3DE dataset), and for the placement of one *seed* point located near the regurgitant orifice[1]. After a few iterations (typically between 100 and 200, requiring approximately 20 secs) a 3D structure containing the regurgitant jet can be obtained. The resulting segmentations along with the corresponding 3D mesh representations is shown in Fig. 6.8 for valves with degenerative MV disease (prolapse) and functional MR.

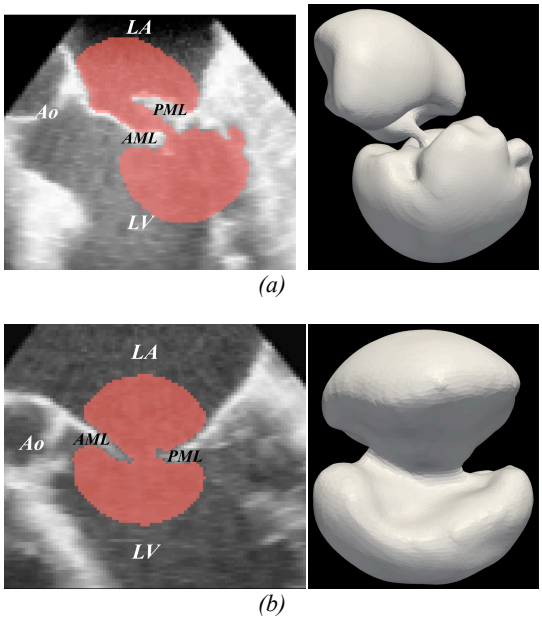

Figure 6.8. Results of void segmentation using active contours for: (a) a patient with degenerative MV disease and (b) a patient with functional MR. The left panel displays 2D cut-planes of the original 3DE datasets with the segmented void regions in red overlay; the right panels depict the 3D mesh representations of the segmented voids. LA: left atrium; LV: left ventricle; Ao: aortic valve; AML: anterior mitral leaflet; PML: posterior mitral leaflet.

[1] Given that this initial segmentation step was used in the final implementation, further details of this method will be given in Sec. 6.3.

The previous examples have been intentionally included to depict the differences in the leaflets configuration (in the patient with MV disease the leaflets overlap, whereas in the second one the tips are facing each other), and at the same time to show the similar characteristics exhibited by the segmented structures: in both cases, two rounded shapes, corresponding to the partial segmentations of the left atrium and ventricle, are connected by a narrow structure, a 'waist', that contains the ARO.

This constitutes an important result since, regardless of the particular pathophysiology of MR (whether it is organic or functional), a similar 3D structure containing the 3D ARO can be obtained. Given the characteristics of this structure, and its further utilization as part of the final implementation for the detection of the regurgitant orifice, a new nomenclature is defined and will be used from now on (refer to Fig. 6.9):

- The convex shapes corresponding to the partial segmentation of the left atrium and ventricle will be called ***cavities***
- The 'waist' or narrower structure connecting the *cavities* is defined as ***channel***. This structure contains the 3D ARO.
- The complete 3D structure that contains both *cavities* and the *channel* will be named ***partial void*** (since it refers to a partial segmentation of the void regions in the 3DE dataset).

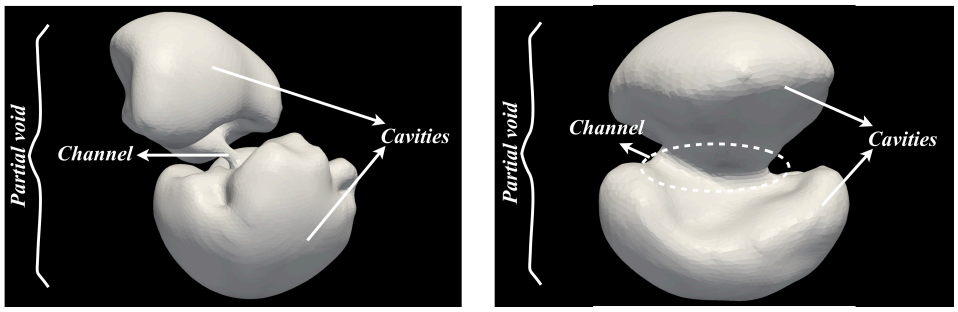

Figure 6.9. Definition of the channel, cavities and partial void.

Thus, based on the geometry of the *partial void*, any algorithm aiming at segmenting the 3D ARO must be capable of correctly detecting the narrower portion located within the *channel*. In the next section, several mesh features aiming at enhancing this region of the *partial void* will be discussed.

6.2.3 Features computed on the *partial void* for the enhancement of the *channel* region

Several simple geometrical priors become evident from the structure of the *partial void* (Fig. 6.9):

i. The *cavities* are broader than the *channel*
ii. The *channel* is located toward the middle of the *partial void*, whereas the *cavities* toward the extrema
iii. The *cavities* are convex shapes, whereas the *channel* seems to be concave
iv. The *channel* can be narrow (Fig. 6.9, left) or wide (Fig. 6.9, right), but in any case it will satisfy the geometrical prior (i)

In order to enhance the *channel*, several shape, curvature and concaveness features were considered, each of them targeting the geometrical priors listed previously:

- The shape diameter function defined by Shapira et al. [83] (Sec. 2.4.11) is a direct measure of how broad or narrow are the *cavities* and the *channel.*

- The average geodesic distance proposed by Zhang et al. [84] (Sec. 2.4.11) will exhibit lower values for vertices near the center of the mesh (the *channel*) and higher values for those located on the extrema (the vertices on top of each *cavity*)
- The Gaussian, mean and principal curvatures (sec. 2.4.9), as well as Koenderink's shape index[81] are a measure of how concave or convex a 3D shape can be.
- A similar measure of convexity/concavity is provided by the concaveness defined by Chen and Georganas[82] (sec. 2.4.10), with the advantage that, when compared with curvature and shape index features, stability and convergence issues during the computation are absent in this case. Thus, it is expected that concaveness provide a more reliable measure.

Special attention must be paid to the curvature, shape index and concaveness measures since they are scale (i.e. *N-ring* size) dependent. In the end, and after conducting preliminary tests, *concaveness* computation with a ring size equal to the 25% of the *partial void's* bounding box, was adequate to correctly depict the concavity/convexity features of both *cavities* and *channel*. Smaller scales were insufficient and unable to capture these features given the dimensions of the structures of interest in the *partial void*.

Conversely, the curvature-based parameters as well as the shape index were discarded, given their unreliability (owed, as mentioned previously, to the numerical instability of its computation). Fig. 6.10 shows the selected computed parameters (shape diameter function, average geodesic distance and concaveness) for the two structures in Fig. 6.9.

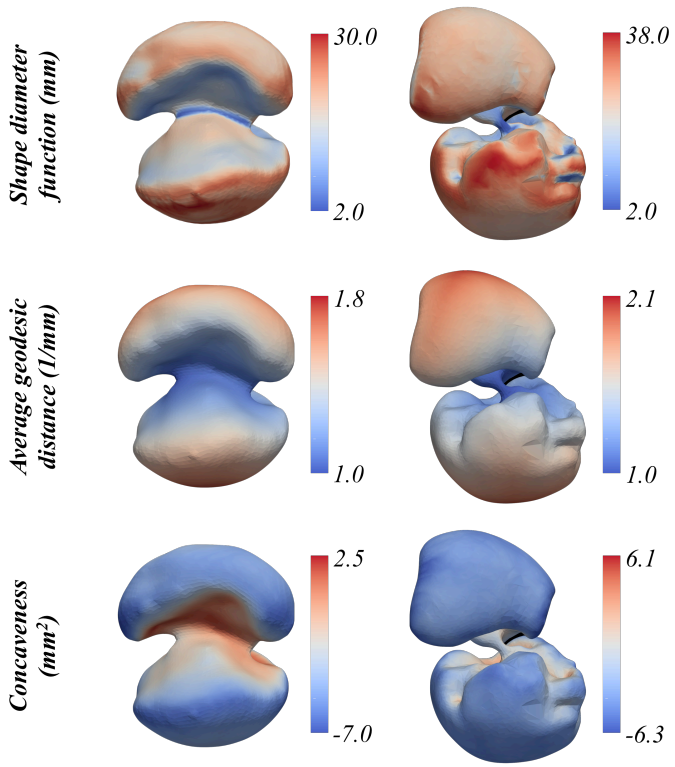

Figure 6.10. Shape diameter, average geodesic distance and concaveness scalar fields computed on the partial voids of Fig. 6.9. The concaveness was computed using a ring size equivalent to 25% of the object's bounding box.

Several observations can be made from the previous figure:

- The shape diameter function provides the most accurate and detailed delineation of the *channel* and the 3D ARO (the dark blue ribbons in Fig. 6.10, first row), whereas the other two parameters provide a lower level of detail and differentiation. The enhancement provided by the shape diameter function is owed to the fact that this measure represents a direct estimation of the object's diameter at each vertex on the mesh, and thus, in regions near the 3D ARO narrower portions, exhibiting lower diameters, are obtained.
- The fact that the average geodesic distance depict also lower values near the *channel* region, is the result of the almost identical size of the *cavities* which implies that the *channel* will be located near the center of the 3D structure. However, this symmetry is almost an exception and in most of the segmented *partial voids* one of the *cavities* is bigger than the other. In these cases, the *channel* region will not necessarily exhibit low geodesic distance values.
- As regards the average geodesic distance field, it is important to notice that the values at the extrema of the object have relatively high values (the red-colored regions in Fig. 6.10, second row). This characteristic provides an additional feature if extrema points of the *partial void* have to be determined (as was the case in the final implementation of the algorithm)
- In the concaveness field, the boundaries between the *channel* and the *cavities* are not well defined, although, as expected, the *channel* seems to exhibit a concave behavior (positive *concaveness* values) at the given scale. However, as mentioned previously, the clear depiction of these characteristics is highly dependent on the choice of the scale (which may not be completely adequate for the case of the patient with MV disease, Fig. 6.10, bottom right; in this case concaveness values close to zero can be observed). In addition, the required computation time is also dependent on the scale, and for a neighborhood size of 25% of the object's bounding box, the required time for the estimation of concaveness at each vertex of the mesh is roughly 3 min (for meshes of 11000 vertices).

Based on the previous observations, it is possible to conclude that the shape diameter function and the average geodesic distance are the most robust features capable of depicting the approximate location of the 3D ARO and of the *partial void* extrema locations, both important features in the final implementation. These findings served as the basis for the development of a new semi-automated algorithm for the segmentation and quantification of the 3D ARO, described in the next section.

6.3 Detailed description of the proposed algorithm

The proposed 3D ARO segmentation algorithm operates on 3DTEE datasets. After selection of a systolic frame and an initial supervised segmentation step, a 3D mesh of the *partial void* is obtained; then, a completely automated graph-based max-flow/min-cut algorithm is used to segment the 3D contour of the ARO. Once segmented, a minimal spanning surface representing the 3D ARO surface is computed and several 2D and 3D morphological parameters are calculated. A flow chart of the steps involved in the segmentation and quantification algorithm is shown in Fig. 6.11.

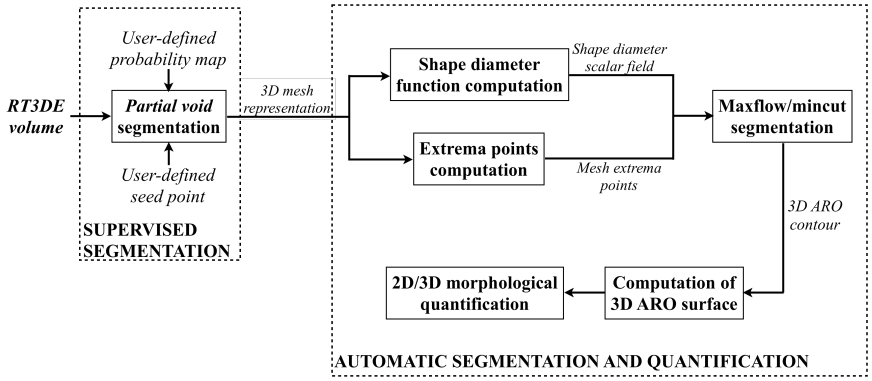

Figure 6.11. Flow chart for the 3D ARO segmentation algorithm.

Each step depicted in the previous figure is described below.

6.3.1 *Partial void* segmentation

To obtain the *partial void*, an active contour method using the region competition approach was used (the details of this method are described in sec. 2.4.5 and in the work of Zhu and Yuille[72]). In this method, a 3D surface evolves at each iteration to estimate a segmentation of the structure of interest. The evolution of this surface is controlled by the sum of internal and external forces:

$$F = \alpha(P_{obj} - P_{bkg}) + \beta k \qquad (6.1)$$

The internal force in (6.1) (βk) is proportional to the mean curvature of the surface (k), whereas the external force ($\alpha(P_{obj} - P_{bkg})$) is a *probability map* representing the probability that a voxel belongs to the object of interest or to the background. In this approach, the *probability map* is the result a smooth threshold applied to the original 3DE volume and defined as a sigmoid function:

$$I_{out} = 1 - \frac{2}{1 + e^{-\frac{I_{in} - \mu}{\sigma}}} \qquad (6.2)$$

where I_{in} represents the original grayscale 3DE image, μ defines the threshold around which the transformation is applied, σ is a smoothing parameter that determines how steep the sigmoid curve is, and I_{out} represents the desired *probability map* with intensity values ranging from -1 to 1.

A fixed value of σ = 0.3 proved adequate for all the datasets tested, whereas the threshold μ must be manually set by the user, given the different acquisition parameters (such as gain and dynamic range) of each 3DE dataset. In practice, with his selection the user has to ensure that void regions (including the regurgitant orifice) are mapped to positive values (i.e., will be located below the defined threshold). Generally, this threshold has an intensity value between 50% and 60% of the maximum intensity value in the 3DE image. An example of a computed *probability map* for an image containing a regurgitant orifice is shown in Fig. 6.12.

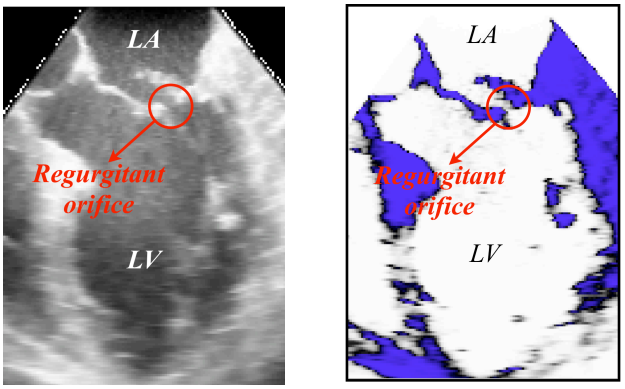

Figure 6.12. (a) A 2D cut-plane of a 3DE dataset containing a prolapsed leaflet; the void regions corresponding to the left atrium (LA), left ventricle (LV) and the regurgitant orifice are also depicted. (b) Probability map of the image in (a), with the void regions having values close to 1 (in white).

The next step of the initialization is to first select a cut-plane containing the orifice and then manually provide one seed point located on the regurgitant orifice; the advantage of the region competition method is that after contour evolution the orifice will always be included in the final segmentation. The final step is the iterative active contour evolution: Fig. 6.13 shows a sequence of iterations starting from the user-defined seed, and where the last panel corresponds to the finally segmented *partial void*.

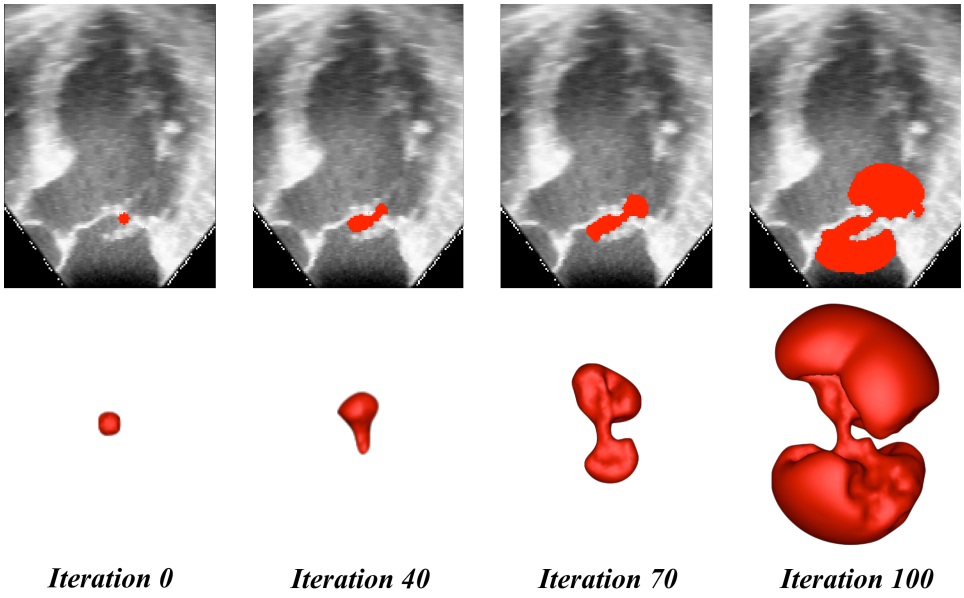

Figure 6.13. Active contour evolution from the initial seed defined by the user. The first row shows a 2D cut-plane of the original 3DE dataset, with the evolving contour shown in red; the second row corresponds to the computed 3D mesh representations of the evolving contour.

Once computed the *partial void*, a 3D mesh representation is obtained using the marching cubes algorithm[75]. The resulting mesh is used as input for the next steps of the algorithm described below.

6.3.2 Shape diameter function computation

As discussed earlier, the shape diameter function (SDF) [83] correctly delineates the narrower structures, and will also be utilized to define the edge capacities in the max-flow/min-cut algorithm.

Essentially the algorithm relies on a simple ray-tracing point-mesh intersection procedure (as already mentioned in sec. 2.4.11): for each vertex on the surface, a cone

centered on its inward unit normal is defined; then, several rays inside this cone are traced and the intersection of each ray with the polygonal mesh is established. Thus, the algorithm requires the definition of two parameters before its application: the cone angle and the number of rays to be traced; the selection of these parameters must ensure that, once computed, the SDF would be as accurate as possible especially in the *channel*, which contains the regurgitant orifice.

Large cone angles imply that some rays will intersect unrelated parts of the mesh (Fig. 6.14a), thus giving an unreliable measure of the shape's diameter; conversely, narrow cones will constrain the rays to portions near the *channel* (Fig. 6.14b), thus ensuring a more accurate diameter computation. On the other hand, a low number of rays may result insufficient to obtain an adequate estimation of the diameter at each vertex (Fig. 6.14c), since only a few portions of the mesh are sampled on each iteration; conversely, a high number of rays ensures a more reliable measure (Fig. 6.14d) but at the same time increases the computation time.

In the end a cone angle of 30º and a total of 30 rays resulted adequate for each of the datasets tested; these settings provided good differentiation of the *channel* and at the same time low computation times (of the order of 15 secs for meshes with 11000 vertices).

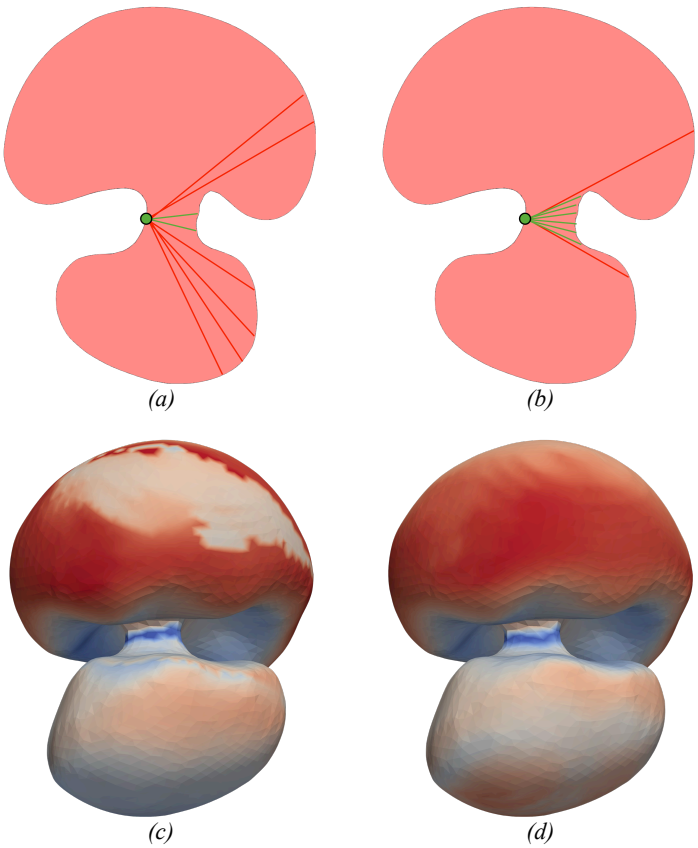

Figure 6.14. The effect of the cone angle and the number of rays in the computation of the SDF. (a) and (b) 2D illustrations of a partial void depicting the how the rays traced intersect different portions of the mesh: for a wider cone angle (a) most of the rays diverge and intersect mesh portions far from the channel (red rays), whereas with a narrower cone angle (b) almost all ray intersections are close to the channel (green rays). (c) Computation of the SDF using 10 rays and a cone angle of 30º, notice the resultant noisy scalar field; (d) Computation of the SDF using 30 rays and a cone angle of 30º, in this case an almost continuous scalar field is obtained

6.3.3 Extrema points computation

The extrema points correspond to the vertices located on the most distal region of each *cavity* in the *partial void* mesh; these points will correspond to the *source* and *sink* nodes of the max-flow/min-cut algorithm.

A modification of the approach described by Katz et al. [116] was implemented in this step. In [116] a set of *feature points* located on the tips of prominent features in the 3D mesh is computed. The algorithm first computes the average geodesic distance[84] (AGD) (see sec. 2.4.11) for each vertex on the mesh and then determines if the vertex is a local maximum by applying the condition:

$$agd(v_i) > agd(v_j), \quad v_j \in \mathbf{x} \tag{6.3}$$

where *agd(.)* are the AGDs at v_i and v_j vertices and **x** is the set of vertices belonging to the *1-ring* neighborhood of v_i. Thus, a vertex will be a local maximum if its AGD value is higher than that of each of its neighboors.

Due to noise in the mesh, the previous condition may also extract points that do not necessarily lie in prominent features of the mesh. An additional constraint is also imposed: a *feature point* must be located in the convex hull of the mesh, thus ensuring that only extrema points are included in this set. Then, the final set of *feature points* can be obtained by:

i. Computing the convex hull of the mesh;
ii. Finding the vertices in the convex hull that satisfy Eq. 6.3;
iii. Repeating (ii) for the mesh, and
iv. Finding the intersection between the sets found in (iii) and (iv).

The result of the previous approach applied to a *partial void* mesh is depicted in Fig. 14a.

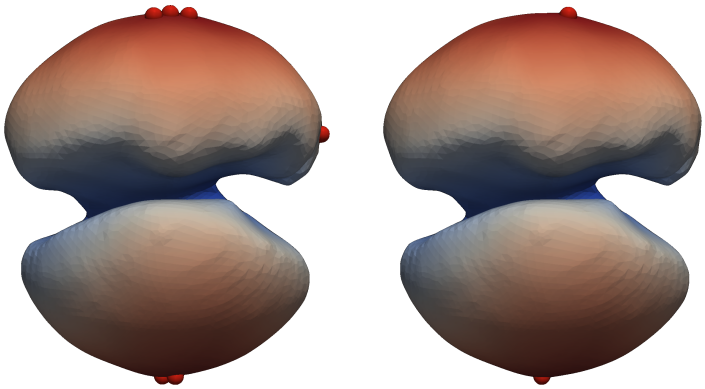

(a) *(b)*

Figure 6.15. (a) Feature points obtained using the algorithm proposed by Katz et al. [116]*; (b) Final source and sink vertices obtained applying the modified algorithm with the additional criterion described in the text. In both panels the color map on the mesh represents the AGD function.*

Notice that most of the computed *feature points* of Fig. 6.15a are located on the extrema regions of each *cavity*, in correspondence also with the local maxima of the AGD function (the red colored regions). In order to obtain only two extrema points, each located on one of the *cavities*, a modification of the previous approach is proposed by introducing and additional criterion:

i. The *source* vertex will be the *feature point* with the highest AGD value
ii. The *sink* vertex will be the *feature point* located at the maximum Euclidean distance from the *source* vertex.

Once applied this criterion on the set of points in Fig. 6.15a, only two vertices remain (Fig. 6.15b) representing the expected location of the *source* and *sink* vertices.

In the next section the segmentation algorithm for the detection of the 3D ARO contour is described.

6.3.4 Max-flow/min-cut segmentation of the 3D ARO contour

With the estimation of the SDF scalar field and of the location of the *source* and *sink* vertices, a directed graph using the mesh edges and vertices is constructed, and then the max-flow/min-cut algorithm is applied to find a 3D contour at the location of the ARO.

The directed graph $G=<V,E>$ consists of nodes V corresponding to each vertex on the *partial void* mesh, and a set of directed edges going from the *source* to the *sink* vertex. To ensure that the min-cut will lie at the location of the ARO, the set of SDF scalar values is first transformed using a non-linear function:

$$sdf_T(v_i) = e^{\left[\frac{sdf(v_i)}{sdf_{\min}}-1\right]} - 1 \qquad (6.4)$$

where sdf_{min} is the global minimum of the SDF, $sdf(v_i)$ is the value of the SDF at vertex v_i and $sdf_T(v_i)$ is its transformed value. With this transformation, the original dynamic range of the SDF scalar field is increased, thus ensuring that values closer to the global minimum (located near the VC) will have transformed values closer to zero. The use of this transformation is useful especially when the SDF field is affected by noise in the mesh.

Once transformed the SDF values, the edge capacities $C_{vi,vj}$, are simply defined as:

$$C_{v_i,v_j} = sdf_T(v_i) + sdf_T(v_j) \qquad (6.5)$$

By this formulation, the edge capacities in the *channel* will be characterized by lower values, thus resulting in a min-cut lying on the ARO.

Fig. 6.16 depicts some examples of the ARO contour segmentation on *partial voids* with different geometries. Notice that, in all cases, the contours coincide with the locations of the lower values in the SDF function, thus representing the 3D contour of the ARO. In addition, and in all the structures, the computed contours are not flat, thus implying that the ARO has, in fact, a non-planar 3D shape.

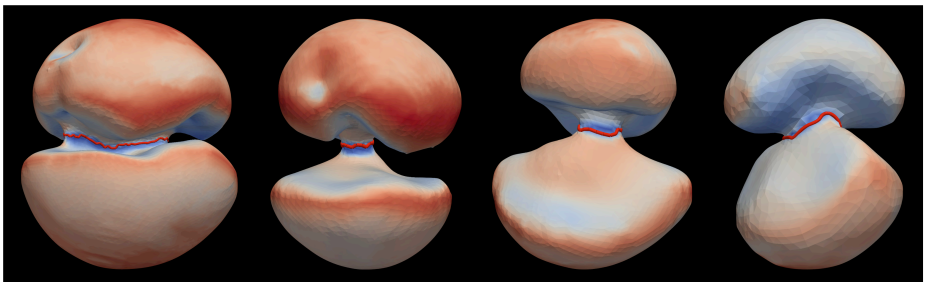

Figure 6.16. Examples of the automatically computed 3D ARO contours using the max-flow/min-cut algorithm. The color map on each mesh represents the computed SDF scalar field (with blue regions corresponding to the lower values), whereas the red contours represent the computed min-cut. Notice the direct correspondence between each contour and the local minima in the SDF field.

Given the limited resolution and the noise present in the mesh, usually a 'jagged' contour is obtained (Fig. 6.17a). An additional step was thus implemented, consisting of a

cubic-spline interpolation applied to the points in the initial contour, which ensures a smooth representation of the 3D ARO boundary (Fig. 6.17b). This smooth contour served as the input for the next steps of the algorithm.

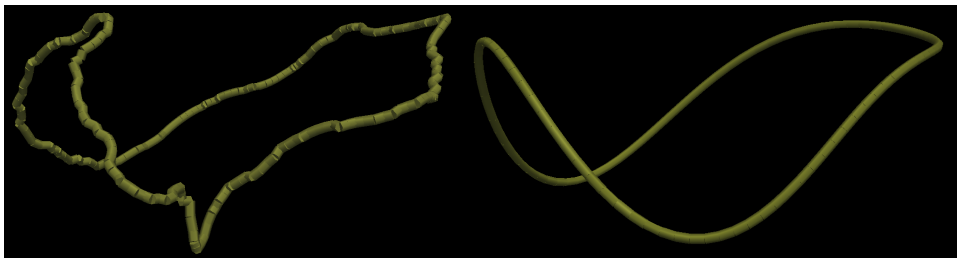

Figure 6.17. Left: an initial 'jagged' contour is obtained from the min-cut segmentation. Right: the smooth ARO contour after cubic-spline interpolation.

6.3.5 Computation of the 3D ARO surface

Given the non-planar shape of the obtained contour, the minimal surface area spanning its boundary was obtained as a representation of the ARO surface. This minimal surface can be computed numerically by using the "stretched membrane" approximation and solving the biharmonic equation [51], [112]. The thin-plate splines represent the fundamental solution to this equation[117], and thus, by applying a thin-plate spline interpolation on the sparse set of points defining the 3D contour, the corresponding 3D ARO surface can be obtained.

In Fig. 6.18 three examples of the computed 3D ARO surfaces are shown. Notice that none of these surfaces is planar or circular.

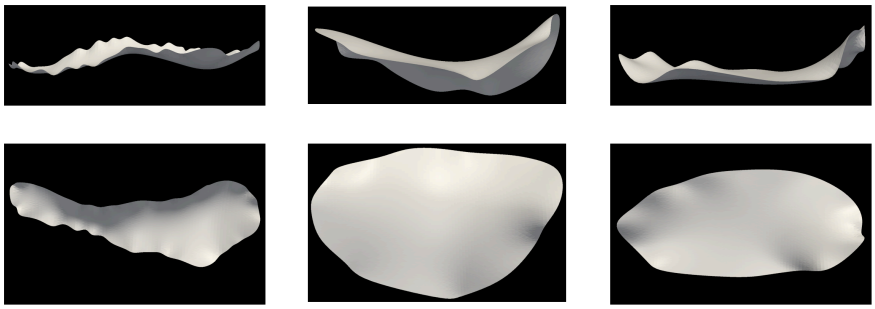

Figure 6.18. Lateral (first row) and superior (second row) views of three computed 3D ARO surfaces.

6.3.6 2D and 3D morphological quantification of the ARO

The 3D surface area and its 2D projected area were computed from the triangulation of the 3D ARO minimal surface. Then, the planarity index, defined as the ratio between the 2D and the 3D area was computed (for an almost planar ARO, this index approaches to 1).

In addition, after projecting the 3D ARO contour onto its best-fit plane, and fitting it to an ellipse, several additional 2D parameters were calculated:

i. Maximum and minimum axes, defined as the length of the semi-major and semi-minor axes of the fitted ellipse, respectively;
ii. Mean axis, defined as the average of the maximum and minimum axes;
iii. Circularity, defined as the ratio between the minimum and the maximum axis. Values closer to 1 represent more circular orifices.

6.3.7 Algorithm's implementation

The semi-automated segmentation of the *partial void* was performed using ITK-SNAP[73], an open source tool that allows the segmentation of medical structures using active contours. The definition of the *feature map* and of the seed point on a cut-plane

depicting the regurgitant orifice required about 1 min. The remaining steps of the process were implemented using the open source programming libraries VTK (Visualization Toolkit)[94] and iGraph[118]. The computation of the shape diameter function and of the extrema points required on average 40 secs, whereas the min-cut computation and the quantification of the ARO required additional 20 secs. This means that a complete quantification of the 3D structure of the ARO was achieved in roughly 2 min (including initialization).

Chapter 7

Segmentation and quantification of the anatomic regurgitant orifice: validation

Given the lack of a true "gold standard" for the quantification of the 3D ARO morphology, a comparison was performed between the 2D parameters obtained using the proposed approach and the results from 2D manual planimetry of the orifice applied to two different patients populations: with degenerative MV disease and functional MR. In addition, the geometry of the ARO was also assessed in terms of 3D and 2D areas of the orifice, as well as its circularity and planarity indices. These results, as well as the discussion and comparison with other approaches, are presented in the next sections.

7.1 Population and validation protocols

7.1.1 Experimental settings

Twenty-five patients (mean age 63±8 years) with mild to severe MR undergoing clinically indicated 3DTEE were enrolled at Centro Cardiologico Monzino (Milan, Italy). From this set of patients, a group of 12 had MR resulting from functional MR (*FMR* group), whereas the remaining 13 patients presented mitral valve prolapse (*MVP* group), with MR resulting from degenerative MV disease.

The protocol was approved by the local Institutional Review Board, and informed consent was obtained from all participants. The 3DE studies were performed using the iE33 system (Philips Medical Systems, Andover, MA) equipped with fully sampled matrix-array 3DTEE transducer (X7-2t), with each acquired volume including the MV, the aortic valve and the proximal ascending aorta, and having dimensions of roughly 200x200x200 voxels with a voxel resolution ranging from 0.2 to 1.3 mm.

7.1.2 Planimetry of the ARO: "Gold standard" measurements

An expert operator proceeded into the analysis of the enrolled population, on the mid-systolic frame of each 3DTEE dataset, based on the following steps:

i. The 3D data was visualized by an *en face* (atrial) view of the MV (Figs. 7.1a, 7.1d). Then, an initial 2D cut-plane, parallel to the anterior-posterior valvular axis, and containing a partial view of the regurgitant orifice, was initially selected. This plane was then tilted and translated until the widest *channel*, containing the ARO, was observed (Figs. 7.1b, 7.1e).
ii. From that view, a 2D cut-plane (corresponding to the green line in Fig.s 7.1b and .1e) normal to the assumed regurgitant flow and thus containing an *en face* view of the regurgitant orifice, was selected. This plane was translated until the orifice with the smallest size, corresponding to the 2D ARO, was observed (Figs. 7.1c, 7.1f).
iii. From this image, the 2D ARO contour was manually traced and its area quantified, using an open source image processing tool (ImageJ, National Institutes of Health [119]). In addition, an ellipse was fitted to the contour

and the circularity index (defined as the ratio of the semi-minor and semi-major axes in the ellipse) was computed.

iv. For each processed volume, the steps (i) to (iii) were performed twice by the same operator in separate sessions blinded to previous results, and the average of the estimated areas and circularity indices was finally reported.

On average, 9 min per volume was the required time to complete the planimetry and quantification of circularity of the ARO.

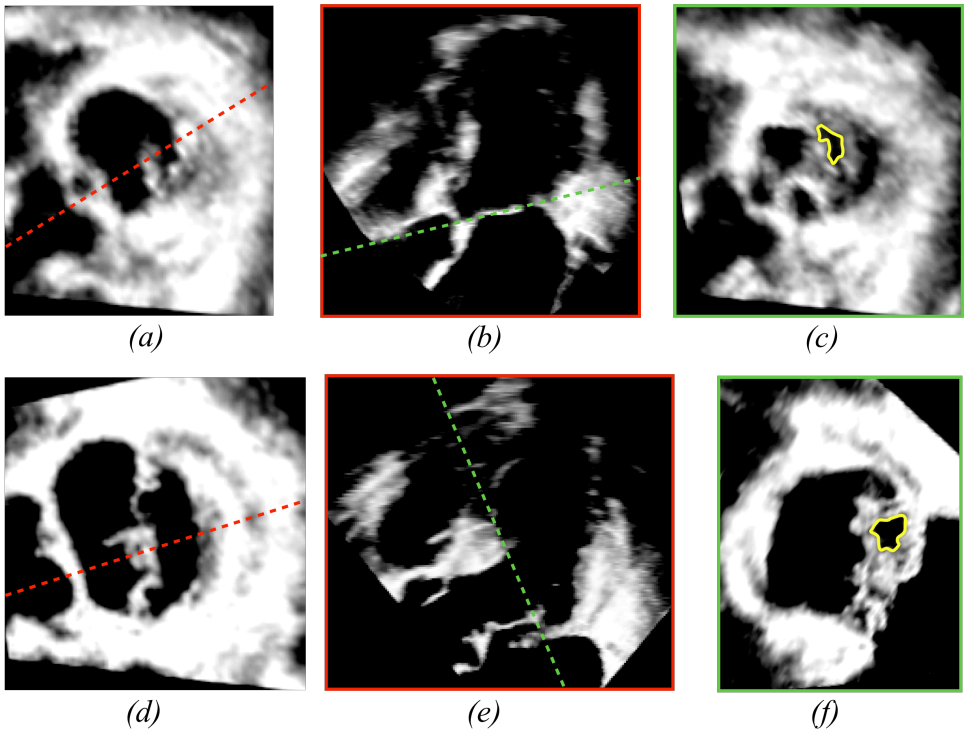

Figure 7.1. Examples of the planimetry procedural steps for the ARO for a valve with functional MR (top row) and a valve with MV prolapse (bottom row). (a) and (d):from an en face view of the MV, a cut-plane in the anterior-posterior direction is obtained (dashed red line); (b) and (e): from the plane containing the channel a cut-plane normal to the regurgitant flow is positioned (dashed green line); (c) and (f): the final plane containing the planimetry of the ARO (yellow contour).

7.1.3 Statistical analysis

To determine the accuracy of the automated measurements, obtained as described in Chapter 6, the 2D area and circularity indices were compared using linear regression and Bland-Altman analyses with the gold standard measurements. The comparisons were performed both for the entire 25 patients, and separately for the *FMR* and *MVP* groups. For each case, the Pearson correlation coefficient r (from the linear regression) and Bland-Altman's bias and confidence intervals (CI) are reported.

7.2 Results

Table 7.1 lists the reproducibility results of the 2D planimetry approach defined as the gold standard. This reproducibility was assessed using the coefficient of variability (CV), defined as the absolute difference between the pair of manual measures (for 2D areas and circularity index) in percent of their mean. For the ARO 2D areas, most of the CV values were below the 10% limit, except for the datasets 3, 4, 8, 9 and 22, with values

above 15% in all cases; conversely, the coefficients of variability for the ARO circularity index were below 11.1% in all cases.

	Dataset ID	ARO 2D areas		ARO circularity	
		Mean (cm^2)	CV (%)	Mean	CV (%)
FMR group	1	0.48	11.0	0.12	4.4
	2	0.28	6.4	0.32	6.9
	3	0.03	18.6	0.68	8.5
	4	0.02	21.3	0.70	8.2
	5	0.18	7.4	0.60	6.7
	6	0.19	9.2	0.45	3.2
	7	0.25	8.3	0.58	9.5
	8	0.06	20.1	0.72	8.4
	9	0.01	16.0	0.86	8.9
	10	0.26	10.2	0.98	9.7
	11	0.10	13.3	0.26	6.2
	12	0.22	9.2	0.25	5.3
MVP group	13	0.28	5.0	0.60	3.8
	14	0.16	8.7	0.90	6.3
	15	0.41	10.3	0.30	9.2
	16	0.13	11.1	0.78	8.5
	17	0.14	8.3	0.58	5.2
	18	0.17	9.5	0.50	5.5
	19	0.23	11.8	0.63	6.1
	20	0.15	6.7	0.61	9.1
	21	0.16	4.7	0.38	3.9
	22	0.01	19.0	0.99	8.3
	23	0.21	10.1	0.43	11.1
	24	0.32	9.5	0.49	8.0
	25	0.21	9.7	0.49	8.4

Table 7.1. Coefficients of variation obtained from the two manual measures of the ARO 2D area and circularity indices.

In addition, to allow visual comparison of the two measures, Fig. 7.2 shows an example of an orifice manually traced by the user and the corresponding 2D view of the same orifice automatically computed by the algorithm.

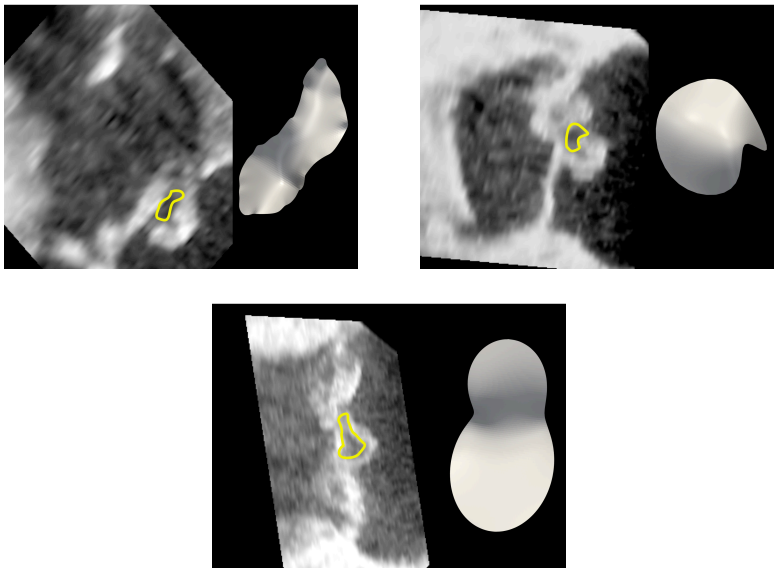

Figure 7.2. Three different examples comparing the 2D contour obtained from planimetry (green contour on the left image of each panel) and a 2D view of the automatically computed 3D ARO (gray shape on the right of each panel)

Fig. 7.3 and Fig. 7.4 show the results of the linear regression and Bland-Altman analysis. The ARO 2D areas (Fig.7.3) showed a good correlation (r = 0.88) and a small negative bias (-0.02 cm^2) with the gold standard for both the combined group of patients,

as well as in each separate group. No significant differences were found when comparing both measures in the combined group or in the *FMR* and *MVP* groups (Student's tests p-values of 0.23, 0.17 and 0.52 respectively), thus implying that both measures were equivalent.

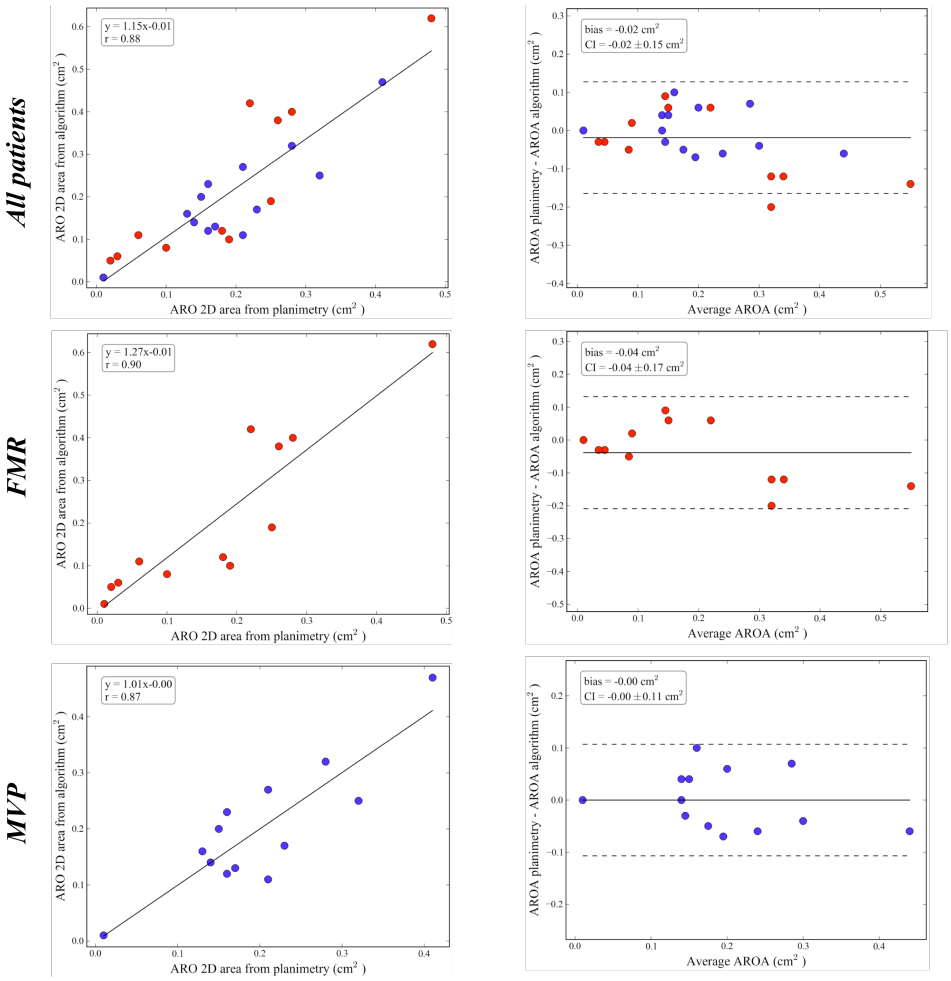

Figure 7.3. Comparison results for the ARO 2D areas, performed in the combined group of patients and on each group separately. Left column: linear regression; right column: Bland-Altman analysis.

For the ARO circularity index (Fig.7.4), the results were highly correlated, with r coefficients of 0.97 and 0.95 for *FMR* and *MVP*, respectively, and 0.95 for all the patients. Small biases and narrow limits of agreement (of the order of ±0.1 cm^2) where found in all cases, and as with the ARO 2D areas, no significant differences were found when comparing both measures in the combined group or in the *FMR* and *MVP* groups (Student's tests p-values of 0.25, 0.75 and 0.22, respectively).

When compared with the results of ARO 2D area comparisons, the circularity index showed a higher level of agreement between the two methods.

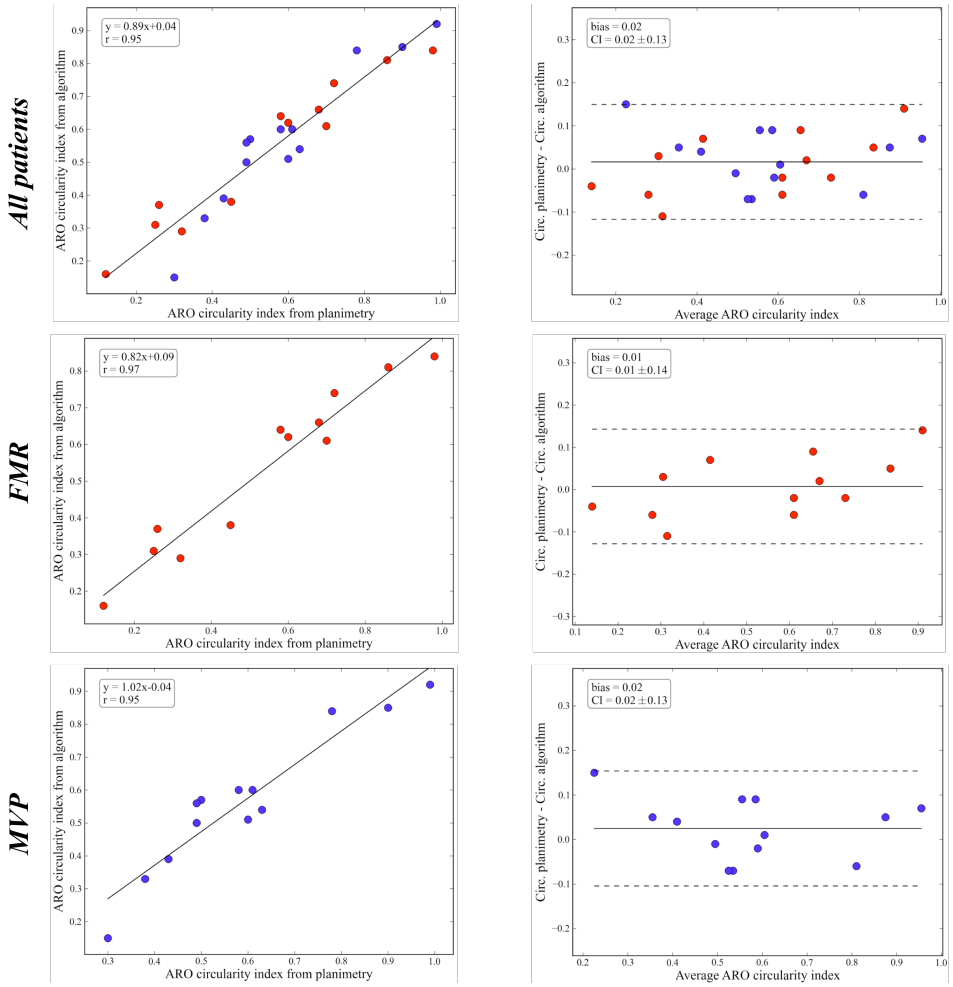

Figure 7.4. Comparison results for the ARO 2D circularity indices, performed in the combined pool of patients and on each group separately. Left column: linear regression; right column: Bland-Altman analysis.

7.3 Morphological characterization of the 3D ARO

Each group of patients was also assessed in terms of the 3D and 2D computed parameters obtained from the automatic detection of the 3D ARO. To test for differences between *FMR* and *MVP* groups on each measured parameter, the Mann-Whitney U test was applied. To test for differences between the 2D and 3D ARO areas, in the combined group and in the *FMR* and *MVP* groups, the Student's paired t-test was applied. In all tests, difference considered significant for $p<0.01$.

Table 7.2 shows the median, 25% and 75% percentiles of the 3D and 2D ARO areas, the planarity and circularity indices for each group.

Parameter \ Group	All patients	FMR	MVP
3D ARO surface area (cm^2)	0.21 (0.13; 0.38)	0.13 (0.09; 0.42)	0.30 (0.17; 0.33)
2D ARO projected area (cm^2)	0.16 (0.11; 0.28)$^{\xi}$	0.12 (0.08; 0.38)$^{\xi}$	0.17 (0.13; 0.27)$^{\xi}$
Planarity index*	0.80 (0.77; 0.90)	0.90 (0.84; 0.92)	0.77 (0.66; 0.78)$^{\zeta}$
Circularity**	0.57 (0.38; 0.66)	0.62 (0.36; 0.68)	0.56 (0.50; 0.60)

* Defined as the ratio of the 2D projected area to the 3D surface area

** Computed from the fitting of the 2D projected contour to an ellipse, and defined as the ratio of the semi-minor to the semi-major axis

$^{\xi}$ $p<0.01$ vs. 3D ARO surface area, Student's paired t-test

$^{\zeta}$ $P<0.01$ vs. FMR, Mann-Whitney U test

Table 7.2. Computed 3D and 2D ARO parameters for the combined, FMR and MVP groups.

In the group of 25 patients, the ARO 3D surface area varied between 0.01 cm^2 and 0.71 cm^2, while the range for the 2D projected area was between 0.01 cm^2 and 0.62 cm^2. For both parameters, no differences between *FMR* and *MVP* were noticeable. In addition, when comparing the 2D and 3D ARO areas on each group, in all cases significant differences were found.

As regards the circularity index, only one patient presented an almost rounded ARO (circularity index = 0.92), whereas the remaining subjects had indices below 0.82. No significant differences were found between groups. As the average values were significantly smaller than 1.0 (median values of 0.62 and 0.56 for the *FMR* and *MVP* groups, respectively), in both cases an elongated ARO was present.

In all cases the presence of non-planar AROs was confirmed by the computed planarity index: only 6/25 patients had an index above 0.9 (but less than 1.0). A median value of 0.80 was observed for the combined group of patients, with values ranging from 0.49 to 0.94. In this parameter, significant differences were found between the pathologic groups, with the *MVP* exhibiting more non-planar ARO than *FMR* (medians of 0.56 vs 0.62).

To further explore the differences between the 2D and 3D ARO computed areas, linear regression and Bland-Altman analyses were carried on between both computations, with the results being shown in Fig. 7.5. For all three cases, high correlation was observed between the 3D and 2D measures (r above 0.95), whereas the bias and confidence intervals, from the Bland-Altman analysis[2], were smaller in the *FMR* when compared with the *MVP* group (1.15±0.16 vs 1.41±0.49).

[2] Y-axis in Fig. 7.5. represents the ratio of the two measures, instead of the difference, so as to remove trends in the data.

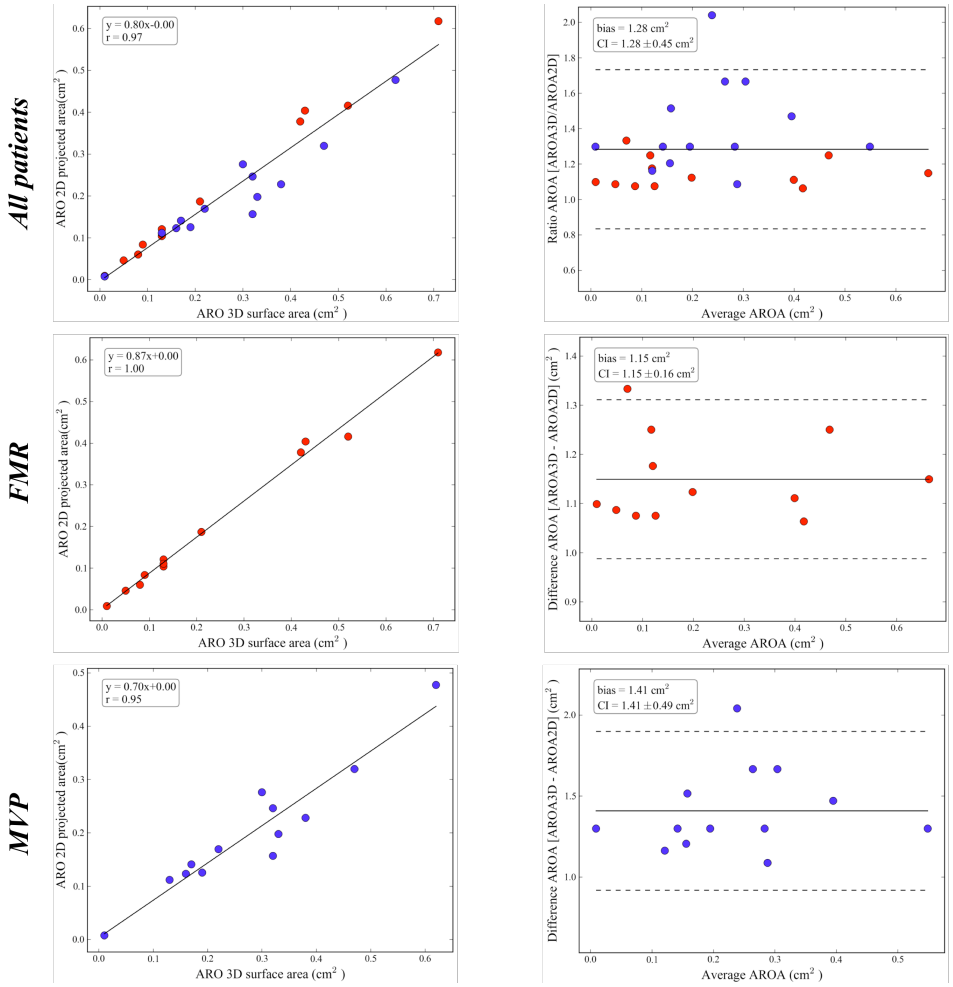

Figure 7.5. Linear regression and Bland-Altman results for the comparison between the ARO 3D and ARO 2D areas, performed in the combined pool of patients and on each group separately. Left column: linear regression; right column: Bland-Altman analysis.

Finally, the histogram distribution of the planarity and circularity indices was also obtained, and is displayed in Fig. 7.6. The distribution of the circularity index was comparable in all three cases, centered toward a value close to 0.5; conversely, the planarity index showed a skewed distribution toward higher values (close to 0.9) for the *FMR*, whereas the *MVP* group exhibited a more central distribution, with values around 0.75.

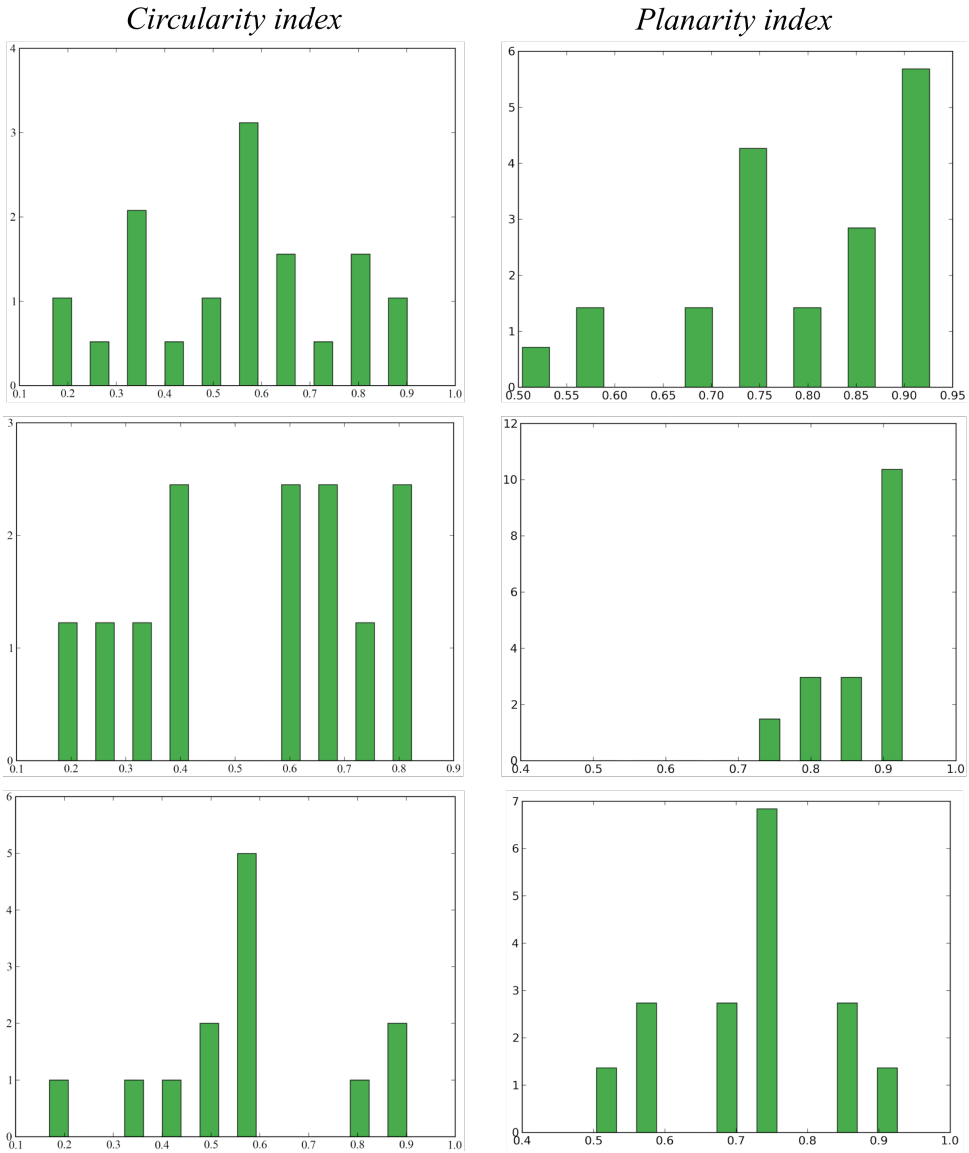

Figure 7.6. Histogram distributions for the circularity (left column) and planarity (right column) indices, for the patients in the combined groups (first row), the FMR group (second row), and MVP group (third row).

7.4 Discussion

7.4.1 Strengths of the algorithm and comparison with other approaches

The successful segmentation of the ARO lies in the max-flow/min-cut algorithm, which allows the computation of a closed connected contour representing its boundary. As discussed in Sec. 6.2.3, the shape diameter function (SDF) [83] is a robust mesh feature that, when computed on the *partial void* mesh, is capable of accurately depict and differentiate the channel that contains the ARO. However, the simple thresholding of the SDF values, or the use of a clustering algorithm (such as k-means) does not satisfy the requirements of a connected closed contour. On the other hand, the use of snakes on the mesh [120], [121] requires the definition of an initial contour that must lie close to the final expected location; even if that requirement is satisfied, snake convergence is not always guaranteed.

Conversely, by representing the 3D triangular mesh as a graph and properly defining a pair of *source* and *sink* nodes as well as the edge capacities, the max-flow/min-cut algorithm can be applied. Since the edges near the ARO have low capacities (given their dependence on the SDF values), once reached the maximum flow those edges will easily be saturated, which corresponds by definition[70] to the minimum cut.

Although not tested in the studied population, the algorithm is potentially capable of quantifying the total regurgitant area also in valves with multiple regurgitant jets. In such configurations, each ARO can be separately segmented using the proposed approach, and then the individual contributions are summed up. Such computation is not possible using the flow convergence method, since the superposition of regurgitant jets makes difficult the visualization of a proximal isovelocity surface in the color Doppler image.

When compared with other approaches, the proposed methodology overcomes many of the previous limitations. Hence the method of Chandra et al. [51], [112] allows the computation of the 3D ARO, it relies on manual tracing in multiple planes from the 3DTEE dataset, thus resulting in time consuming and user dependent procedure, which in turn reduces the reproducibility of the measurements. In addition, it is not clear how this algorithm could perform in MV with overlapping prolapsed leaflets.

As our method relies on minimal user intervention (during the active contour segmentation of the *partial void*), together with the reduced computation time, it allows the quantification of the 3D ARO in about 2 min, with the capability of segmenting orifices both in MV with functional MR and prolapse.

Moraldo et al. [53]used an automatic image processing algorithm to process a time sequence of 2D color Doppler frames images, thus obtaining an estimation of the EROA without user interaction, and thus high repeatability. However, to eliminate the need of user interaction a high frame rate is required and, in addition, the area computation still relies on geometrical assumptions about the circularity of the orifice which makes the obtained measure of EROA still unreliable. In the proposed approach, only one 3DTEE systolic frame is required to compute the 3D ARO, together with the lack of assumptions about its shape.

Grady et al. [52] computed the EROA by directly segmenting the 3D proximal isovelocity surface from the 3D color Doppler component of the 3DE dataset, thus avoiding any assumptions about the shape of the orifice. However, this algorithm still relies in the color Doppler dataset; data acquisition is based on longer procedure, as more beats need to be subsequently acquired to generate the pyramidal dataset, with potential limitations in patients with unstable heart rate and difficulties in keeping a prolonged apnea. In addition, the computed EROA area is still an indirect measure of the ARO area. On the contrary, the proposed algorithm makes use of existent technologies for the acquisition of 3DTEE datasets, and the segmentation is directly applied on the voids present in the images; thus, the segmented *partial void* represents the underlying anatomical structure containing the regurgitant orifice.

7.4.2 Validation with manual planimetry and differences in ARO geometry on different populations

The high level of agreement between the computed ARO 2D area and that obtained using planimetry of the orifice confirms the reliability of the proposed approach as a tool for the estimation of the ARO geometry. In particular for both groups, narrow confidence intervals (from Bland-Altman analyses) and high correlation coefficients were obtained.

The level of agreement was even higher when the circularity index was considered. This is due to the fact that this index represents a proportion between the minor and major axes of the 2D ARO. An overestimation of the ARO area resulting from

an increased length of both axes is masked once the ratio is computed. This explains the obtained zero biases, and the narrow limits of agreement.

The morphological analysis resulting from the 3D and 2D computed parameters in the two groups of patients using the proposed method, showed interesting findings. The first conclusion is that, regardless of the etiology of the MR, whether it is functional or organic (as in degenerative MV disease), almost all orifices (24 out of 25) in the studied population had a non-circular shape (Table 7.2 and first column in Fig. 7.6). This is in agreement with literature[3], [106], [107] using planimetry of the regurgitant orifice, and challenges the current standard clinical approaches[62], [105] relying on the measurement of both the VC width and the effective regurgitant orifice area via 2D color Doppler and the flow convergence method, which are based on the assumption of a symmetric regurgitant orifice.

The second finding regards the non-planarity of the ARO, thus indicating the existence of curved orifices. This also confirms what was already suggested by Grayburn et al.[111], and calls into question several approaches for the assessment of the ARO using planimetry with 3DTEE datasets and cardiac magnetic resonance[63], [64], [54]. In all of these cases, and in current clinical assessments that assume a planar orifice, the ARO area becomes underestimated (as confirmed by the significant differences displayed in Table 7.2), which can have profound implications in the diagnosis of patients with MR.

Current guidelines [62], [105] for the assessment of the severity of MR rely, among others, in the quantification of the effective regurgitant orifice area (EROA) using 2D color Doppler imaging:

- Mild MR: EROA $\leq$ 0.20 cm2
- Moderate MR: 0.20 < EROA $\leq$ 0.40 cm2
- Severe MR: EROA > 0.40 cm2

Based on the previous results regarding ARO non-planarity, and taking into account that the EROA assumes a planar orifice, it is possible to conclude that in particular cases the clinical standard approach could be misleading, with misclassification of the MR severity.

For example, if a planarity index of 0.5 (the lowest value found in the studied population) is assumed, this implies that the real size of the regurgitant orifice, if measured using the flow convergence method, is in fact twice that of the EROA. The big difference between these two values implies that the patient can be misdiagnosed with mild instead of severe MR, which can have an effect in the treatment planning defined by the cardiologist.

A concluding remark, also regarding the non-planarity of the ARO, are the significant differences found between the *FMR* and the *MVP* groups, with the latter exhibiting more curved orifices (Table 7.2); a result also confirmed by the high bias in Fig. 7.5 (on average the ARO 3D surface area is 1.41 times the ARO 2D area in the *MVP* group) and by the more centered histogram distribution in Fig. 7.6 (bottom right). This could be attributed to the complex morphology of the *channel* in these valves, where instead of "non-touching" leaflets (as in functional MR), leaflet overlapping is present in this case.

7.4.3 Limitations

The main limitation of the proposed 3D approach is in a proper validation with a 3D gold standard for the geometry of the ARO. Although comparisons with direct ARO planimetry showed high correlation, we cannot ensure that the computed contour and the derived parameters completely correspond to the true regurgitant orifice. However, our findings on the non-circularity and non-planarity of the ARO show that the proposed

approach could be a more reliable tool in the assessment of the severity of MR given the additional dimension in the computed parameters.

Another limitation is that the proposed approach offers 3D ARO quantification on a single (systolic) frame of the 3DE dataset, since it is known that coapting forces (and thus the size and shape of the orifice) varies through systole owed to changes in load conditions. Thus, further interaction would be required in order to completely characterize 3D ARO morphology during systole, both in functional and degenerative MR.

Chapter 8

Future directions

This chapter describes some applications to other cardiac valves and further possibilities offered by the tools described previously. In particular, the feasibility of the semi-automated quantitative assessment of the tricuspid and aortic valves is discussed in light of the algorithms described in chapters 3 and 6 for the segmentation and quantification of the MA, ML and the ARO. In addition, a discussion regarding the use of the MA and ML segmentation algorithm for the dynamic analysis of the MV is presented.

8.1 Morphologic quantification of annulus and leaflets in the tricuspid valve

Given the morphological similarities between the mitral and tricuspid valves (i.e., the presence of the leaflets attached to an annular structure, as well as the 3D non-planar shape of its annulus), we considered that the method for the segmentation of MA and ML and the quantification of its morphological parameters could be extended to the characterization of the tricuspid valve (TV).

To verify this hypothesis, the algorithms were tested on a TTE dataset containing a human TV; this approach allowed the complete 3D characterization of the tricuspid annulus (TA) and the tricuspid leaflets (TL), including the computation of regional TL parameters such as thickness, tenting as curvature.

Before describing the implemented approach, some additional notation will be introduced, using Fig. 8.1 as reference.

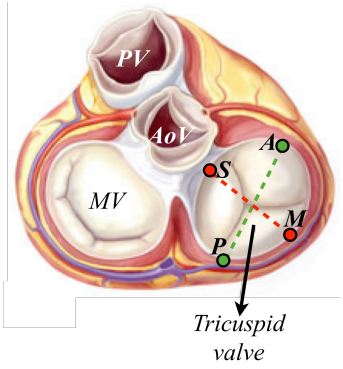

Figure 8.1. Illustration representing the four annular reference points used in this study. A: anterior; P: posterior; S: septal; M: medial; MV: mitral valve; AoV: aortic valve; PV: pulmonary valve. (image modified from http://www.mitralvalverepair.org/images/mv_anatomy/anatomy.jpg)

Based on this figure, four annular reference points were defined as in Kwan et al. [18]:

- The anterior (A) and posterior (P) annular points (green dots in Fig. 8.1) that define the AP axis (dashed green line in Fig. 8.1)
- The septal (S) and medial (M) point of the free wall annulus (red points in Fig. 8.1), defining the SM axis (dashed red line in Fig. 8.1)

Fig. 8.2 shows different cross-sectional planes taken from the TTE dataset used for this experiment. Notice that, in spite of being closer to the aortic valve, the septal annular point can be readily differentiated and, as with the other annular locations, corresponds to a thin-thick junction (Fig. 8.2, second panel). This is different from the morphology of the anterior point in the MV, which cannot be easily differentiated given the continuity with the aortomitral septum. This morphological prior implies some minor modifications on the initialization of the algorithm, as will be explained later.

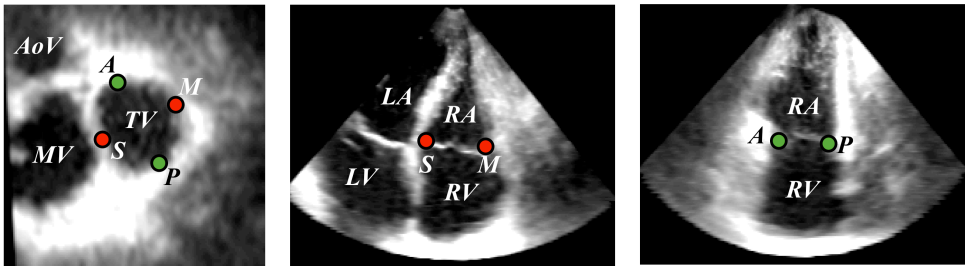

Figure 8.2. The anatomical reference markers for the TA as seen on the 3DTEE dataset used in this experiment. Left: atrial cut-plane; middle: cut-plane in the SM direction; right: cut-plane in the AP direction. AoV: aortic valve; MV: mitral valve; LA: left atrium; LV: left ventricle; RA: right atrium; RV: right ventricle.

In the following, the approach for the segmentation of the TA and the TV is presented, along with the results of the quantitative assessment.

8.1.1 Segmentation of TA and TL and computation of 3D representations

The segmentation of the TA and TL closely follows the previously described approach for the segmentation of the MA and the ML (sec. 3.3); that is, starting from a set of 8 user-defined annular points (and one point located in the right atrium), the algorithm successfully constructs the 3D representation of the TA followed by the automatic computation of the TL surface.

However, in this approach a minor modification was introduced: the 8 user-defined points are symmetrically distributed along the TA contour, instead of a denser initialization in the anterior annular portion utilized for the MA. The TA initialization procedure can then be summarized as follows (Fig. 8.3):

i. Selection of the S and M points and one point in the right atrium (Fig. 8.3a, red points). From this set of points, 36 rotational cut-planes are automatically computed, with the right atrium point ensuring that on each cut-plane the atrium will always lie on top of the valvular plane.
ii. The A and P points are selected from a cut-plane orthogonal to that defined in (i) (Fig. 8.3b, green points)
iii. Four additional points are symmetrically positioned around the TA contour, thus completing the initialization procedure (Fig. 8.3c, blue points).

As mentioned previously, this was the only minor modification to the proposed algorithm for its applicability to TV quantification. The next steps of the segmentation are identical, both for the TA and the TL segmentation, as well as for the computation of their corresponding 3D representations.

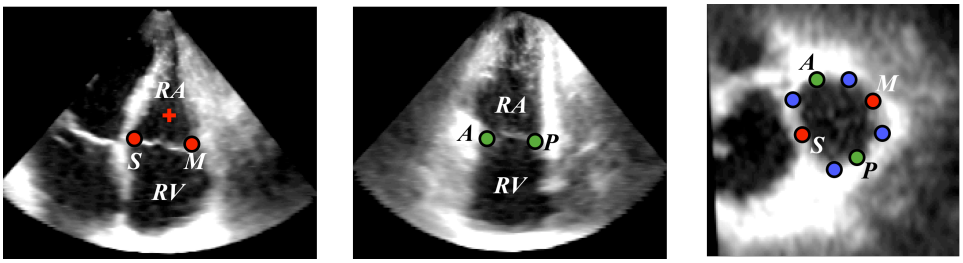

Figure 8.3. Location of the initialization points required for the TA segmentation algorithm. (a) S, M and RV points; (b) A and P points; (c) An atrial view of the TA depicting the 8 user-defined points.

As for the MV, a set of regional and global morphology parameters were obtained:

8) TA perimeter;
9) A-P and S-M diameters;
10) TA height
11) TA 3D surface area and 2D projected area
12) TL combined surface area
13) Tenting volume
14) TLregional thickness, tenting and curvedness

8.1.2 Results

To verify the applicability of the proposed algorithm, a TTE dataset containing a dilated TV with moderated regurgitation, acquired at Centro Cardiologico Monzino (Milan, Italy), was used. During acquisition care was taken to ensure that the complete TV structure (including TA and TL) as well as the right ventricle (RV) and the right atrium (RA) were contained in the dataset. The acquired volume had dimensions of 265x293x208 voxels and a voxel resolution of 0.79 mm.

The initialization and processing times required to obtain a complete characterization of this dataset where comparable to those required for the analysis of the MV (2 min approximately). Fig. 8.4 shows a 3D rendering of the original volume with the corresponding TA and TL 3D representations superimposed. This visual inspection allowed confirming that the computed representations are consistent with the information contained in the 3DE dataset.

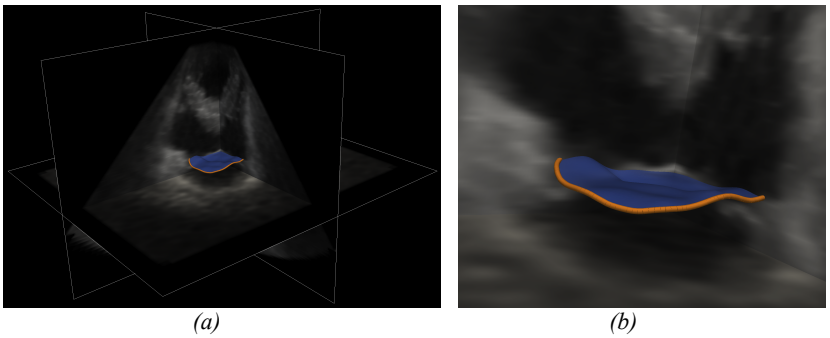

(a) *(b)*

Figure 8.4. (a) The computed TA (orange contour) and TL (blue surface) superimposed onto the original 3DE dataset. (b) A zoomed view of the image in (a).

Fig. 8.5. shows the 3D TA contour and the TL surface automatically computed from the set of initialization points. The TA evidenced a non-planar structure (as seen from the oblique view in Fig. 8.5, left) with an oval shape (as seen from the atrial view in Fig. 8.5, right), whereas the TL tips are slightly tethered toward the RV, as a result of the tension imposed by the chordae tendineae. In addition, when compared with the ML reconstructions shown in chapter 3, the TL the surface seems more flattened.

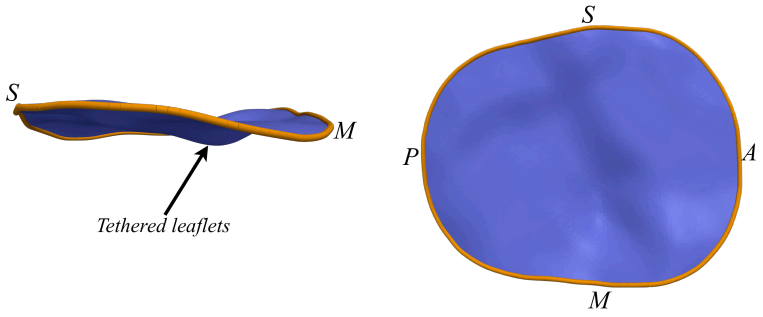

Figure 8.5. Oblique (left) and atrial (right) views of the computed TA and TL.

The results of the global morphologic quantification are summarized below:

i. TA perimeter: 118 mm.
ii. A-P and S-M diameters: 41.15 mm and 32.3 mm.
iii. TA height: 5.0 mm.
iv. TA 3D surface area and 2D projected area: 13.4 cm^2 and 12.2 cm^2.
v. TL combined surface area: 11.8 cm^2.
vi. Tenting volume: 1.0 ml.

Finally, the resulting local thickness, tenting and curvedness patterns are displayed in Fig. 8.6. Low thickness regions are present near the region in which the leaflets tips meet during closure, whereas high tenting and curvedness zones are observed toward the medial region.

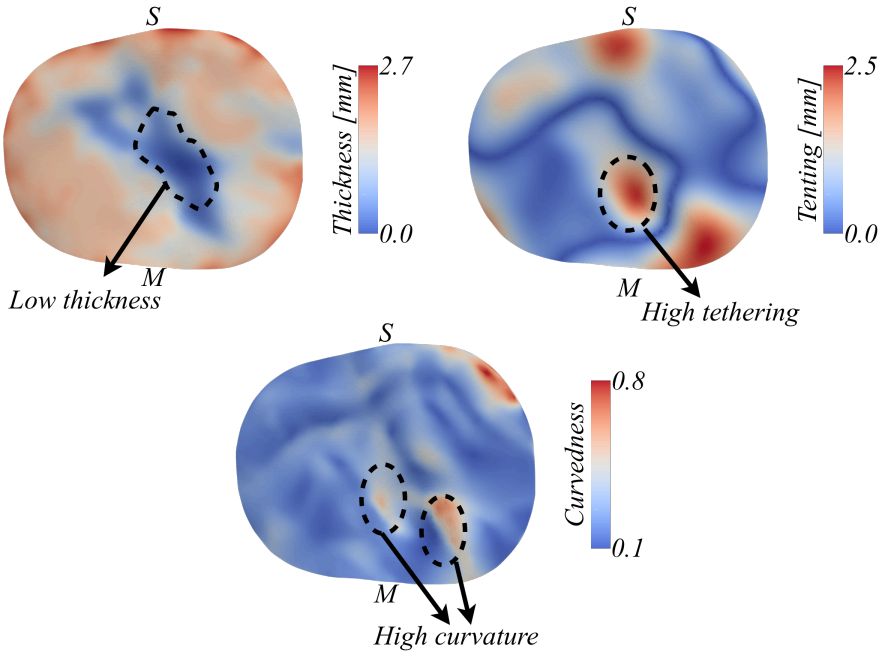

Figure 8.6. Regional distribution of thickness, tenting and curvedness in the studied TV, automatically obtained with the quantification algorithm.

8.1.3 Discussion

The semi-automated approach for the assessment of the MV morphology proved also to be applicable for the complete characterization of the TA and TL, with the only exception that the eight initialization points located on the annulus are evenly distributed

along the contour (this doesn't add complexity to the initialization procedure or increase the computation time).

In addition, the algorithm seems to correctly depict the morphology of the TA, since from its 3D reconstruction an almost oval shape and a non-planar contour were observed, along with the presence of two high points toward the S and M regions and two lower portions toward the A and P regions, in agreement with previous reports [17], [18] (recall Fig. 8.5, left).

The annular shape was elliptical, with well differentiated values for the AP and SM diameters (41.2 vs 32.3 mm) and with 2D and 3D TA areas of 12.2 cm^2 and 13.4 cm^2. This result is consistent with those reported by Anwar et al. [19], where 3DE datasets were acquired from normal patients, and AP diameters of 40±7 mm and 2D TA areas of 10.0±2.9 cm^2 were found. In addition, coincidences were also found with the work of Maffessanti et al. [122], where cardiac magnetic resonance was used to assess the morphology of the TA from diastole to systole in normal subjects. In that work, the 2D and 3D TA area median values reported were of 10.6 and 11.2 cm^2, whereas median values of 37.0, 33.0 and 5.6 mm were found for the AP and SM diameters and for the TA height. When compared with normal dimensions, the tested dataset evidenced higher 2D and 3D TA areas as well as larger AP and SM diameters, consistent with the dilated dimensions of the TV.

The quantified tenting volume and regional tenting distribution (Fig. 8.6) were also similar to the results reported by Sukmawan et al. [123], where tenting volumes of 1.1±0.6 ml and relatively flat tenting distributions were found for normal populations. In the studied patient, a tenting volume of 1.0 ml was measured, whereas, as seen in Fig. 8.5 (left), an almost flat TL surface was observed, which is also consistent with the regional tenting distribution (where most of the values are below 1.3 mm, and the higher tenting observed, near the M region, was about 2.5 mm, still low if compared with the measured TA height of 5.0 mm).

The validity of the computed regional thickness and curvedness, as well as the computed 3D surface area of the TL, remain to be confirmed, since there are no previous studies capable of quantifying these parameters in different populations; however the low thickness regions in Fig. 8.6 represent the malcoaptation of the TV with moderate regurgitation. This in turn underlines the novelty of this approach since, to the best of our knowledge, it constitutes the first practical implementation of a method for the delineation and quantification of the TA and TL structure, including both global and regional characterization. Although Sukmawan et al. [123] already proposed a similar approach for the 3D reconstruction of the TA and TL, the method is impractical since it involves a complete manual tracing of TA and TL in several radial cut-planes, which implies an extended interaction time and reduces the repeatability of the method, thus limiting its clinical applicability.

The previous results were encouraging, and open the possibility of a thorough and detailed analysis of the TV, with the aim of giving new insights into its morphology in different diseased populations. As already stated by Badano et al., the lack of standardized measures and specific software for the quantification of the TA and TL is one of the main obstacles in the integration of 3DE for the assessment of TV morphology and function in clinical routine[124]. We consider that the previously described approach is one step towards reducing this barrier.

8.2 Further possibilities

8.2.1 Assessment of aortic valve stenosis

As with the MV stenosis, in the aortic valve this disease prevents proper opening of the valve. The most common causes of aortic stenosis are a bicuspid aortic valve with superimposed calcific changes, calcific stenosis of a trileaflet valve, and rheumatic valve disease[125] (Fig. 8.7).

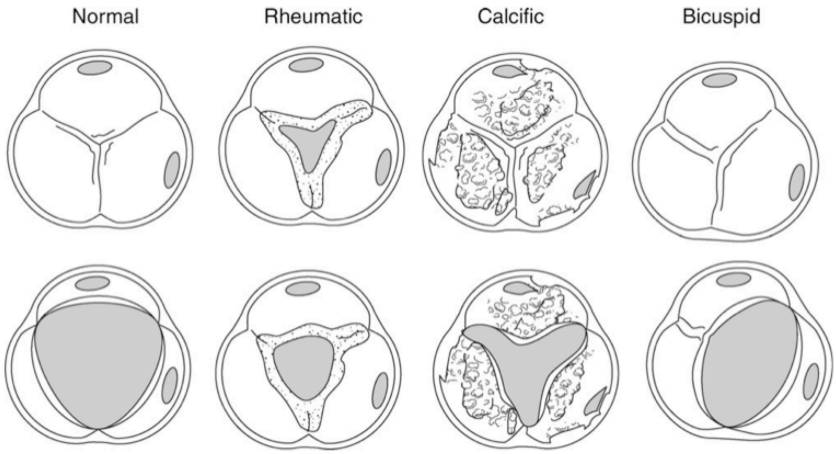

Figure 8.7. Illustration of the most common causes of aortic stenosis (image taken from Baumgartner et al. [125])

Current guidelines suggest the use of Doppler echocardiography for the assessment of aortic stenosis [126], with the aortic valve orifice area, when the valve is open, being one of the most important parameters to determine the severity of this disease. However, these area measurements are operator dependent[125], [126] and thus additional physiological parameters are required to obtain a reliable assessment.

Given the morphological similarities between the anatomic regurgitant orifice (in the MV) and the aortic valve orifice in stenotic valves (i.e. the presence of a channel through which the blood flows), we consider that the method described in Chapter 6 for the segmentation and quantification of the ARO could also be used for the estimation of the aortic valve orifice area in stenotic valves. To test this hypothesis, a 3DE dataset of a patient with calcific aortic stenosis (with a valve morphology similar to that shown in the third column of Fig. 8.7), and with a voxel resolution of 0.49 mm, was acquired at Centro Cardiologico Monzino (Milan, IT). Two cut-planes taken from this dataset, and depicting the approximate location of the orifice, are shown in Fig. 8.8.

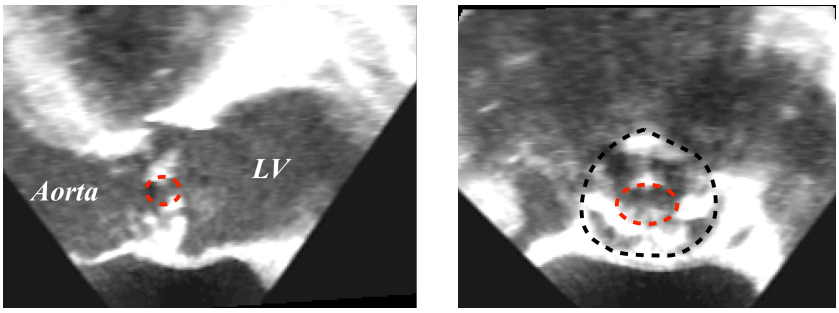

Figure 8.8. Two cut-planes of the 3DE used in this experiment. (a) Location of the aortic valve (between the left ventricle, LV, and the aorta) and of the orifice (dashed red contour); (b) the valve as seen from the aorta (dashed black contour) and the approximate location of the orifice (dashed red contour).

The next step was to apply the method described in Chapter 6 for the detection of the orifice; that is, first the user obtained a *probability map* by defining a threshold on the volume and then manually traced a seed point located near the center of the orifice, then the automatic graph-based method computed the min-cut of the *partial void* mesh's graph representation, corresponding to the 3D detected orifice. Fig. 8.9 (a, b) shows two views of the computed *partial void* and Fig. 8.9c depicts two different views of the computed orifice.

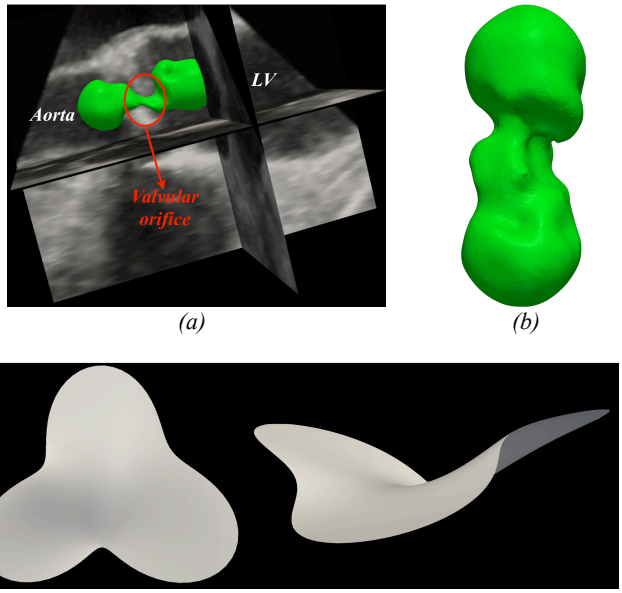

Figure 8.9. (a) The computed partial void (green) superimposed onto the original 3DE dataset, with the valvular orifice delineated by the red circle; (b) 3D mesh representation of the partial void; (c) Two views of the computed valvular orifice (the first surface on the left corresponds to the orifice as seen from the aorta)

The corresponding morphological parameters computed from the 3D surface representation of Fig. 8.9c were:

- 3D surface area: 0.62 cm^2
- 2D projected area: 0.56 cm^2
- Planarity index: 0.90

As a reference, the valvular orifice area measured using conventional 2D Doppler echocardiography was 0.42 cm^2. It is interesting to notice the shape of the computed orifice as seen from Fig. 8.9c (left), quite different from the rounded or elongated shapes of the regurgitant orifices in the MR patients; this underlines once again the versatility of the method to handle orifices with a variety of geometries.

Although a thorough validation of the approach is necessary on a higher number of cases, from the previous example it becomes evident the feasibility of this approach for the assessment of patients with aortic stenosis. In addition, it is also important to notice that the initialization procedure, in particular the location of the seed point, was not straightforward and required a trial and error approach to ensure both that the complete orifice was contained in the segmented *partial void* and that this structure contained two convex surfaces (one on the left ventricle and the other on the aorta) both connected by the *channel* containing the valvular orifice. Thus, a modification in the initialization procedure, by tracing more than one seed, might be required in these cases to ensure proper segmentation and quantification of the orifice.

8.2.2 Assessment of aortic and tricuspid regurgitation

The severity of TV and aortic valve regurgitation is commonly assessed using color Doppler flow imaging.

In the case of the TV, Velayudhan et al. [127] used a planimetry approach on the 3DE color Doppler dataset to obtain the area of the vena contracta; they also proposed new criteria for assessing the severity of the regurgitation based on this vena contracta area. In a more recent work, Song et al. [128] assessed a total of 52 patients with various degrees of functional TV regurgitation using 3DE color Doppler echocardiographic images; in this approach the effective regurgitant orifice area was obtained using the flow convergence method, and also new cutoff values were proposed for classifying the severity of the regurgitation.

Similar approaches have been implemented for the assessment of aortic regurgitation. In [129], Mori et al. proposed a planimetry approach to measure the vena contracta area in 3D color Doppler acquisitions; based on the experiments carried on in animals, a seemingly accurate assessment of the severity was achieved. In addition, current guidelines [130] recommend the use of the vena contracta width and the computation of the effective regurgitant orifice from 3DE color Doppler datasets.

As already discussed in sec. 6.1.1 for the quantification of mitral regurgitation, the common pitfalls in the use of color Doppler datasets and of the flow convergence method are: (i) The careful setting of acquisition parameters (such as gain and color scale), which are highly dependent on user experience, and (ii) the assumption of planar and circular regurgitant orifices. However, as shown in chapter 7 and also confirmed by previous works [3], [106], [107], in most of the patients the shape of the ARO is elongated instead of circular. In addition, also based on our findings, this orifice is non planar, which implies that flow convergence or planimetry based approaches fail to describe adequately its shape.

Based on the previous discussion, we consider that the proposed algorithm for the segmentation and quantification of the 3D ARO in valves with MR could easily be extended without modifications to the assessment of regurgitation in the tricuspid and aortic valves. In the proposed approach, instead of segmenting the valvular structures near the orifice (i.e. the leaflets), a generic 3D structure, the *partial void*, resulting from the segmentation of the intensity voids (the blood flow) in the 3DE ultrasound dataset, is used for segmenting the 3D ARO contour and deriving its surface and quantitative parameters. Being a generic structure, the same geometry (consisting of two *cavities* and a *channel* connecting them) can be found if the voids in the aortic or tricuspid valves are segmented. Although it remains to be tested, we consider that this approach will prove successful when applied to TTE datasets of aortic or tricuspid regurgitant valves.

8.2.3 Dynamic analysis of the MV

Given the continuous motion of the MV during the cardiac cycle, it is of clinical interest the quantification of its dynamics. Currently, several custom and commercial tools have been developed to this aim[26], [29], [34], [28], [30], [21], giving a complete characterization of the MA and, in some cases, ML function during the cardiac cycle. However, many of these approaches rely on models that usually predict the geometry of the ML during systole from segmentations of open valve configurations.

As already discussed in sec. 3.1.2, such approaches lack a detailed delineation of the leaflets and, most of the times, fail at correctly representing their configuration in closed valve configurations. If a complete understanding of the MV dynamics is to be achieved, more accurate methods for the estimation of the ML shape have to be implemented.

We consider that by introducing some modifications in the proposed approach for the MA and ML segmentation, the semi-automatic dynamic analysis of the MV can be achieved. In particular, and taking into account that the ML segmentation algorithm

operates directly on the 3DTEE dataset, and thus instead of inferring the leaflets configuration the obtained surface is a direct representation of their geometry, such tool would provide a more accurate assessment and quantification of the ML structure during systole.

Recalling sec. 3.3.3, where the ML segmentation algorithm was explained, the only requirement for the segmentation of the ML is the knowledge of the annular points. Once obtained these locations (two for each cut-plane), the graph-based approach allows the construction of the connective path (i.e, the leaflets) between the annular points. Thus, the only requirement for the segmentation of the ML on each systolic frame of the 3DTEE dataset is the knowledge at each point time of the MA contour.

In fact, if initialization is performed on the first systolic frame, we consider that the modified block-matching approach described in section 3.3.2 can be used to track the location of the initialization points on each of the remaining systolic frames. Once performed this tracking, the construction of the annular contour and the detection of the ML surface can be computed on each frame.

The proposed workflow for a 3DE dataset with N systolic frames would be:

i. Manually define the set $\boldsymbol{x_0}$ of 9 initialization points (8 lying in the MA, and one on the left atrium) in the end-diastolic frame f_0.
ii. Compute the 36 radial cut-planes in the next frame, f_1, using the set $\boldsymbol{x_0}$.
iii. Obtain $\boldsymbol{x_1}$, the set of 9 initialization points in f_1 obtained by tracking $\boldsymbol{x_0}$ with the modified block-matching approach of sec. 3.3.2.
iv. Repeat the steps (ii) and (iii) between consecutive pairs of frames until each set of initialization points $\boldsymbol{x_i}$ ($i=0...N$) has been computed for each of the systolic frames.

Once applied steps (i)-(iv), each systolic frame will have a set of 9 initialization points and 36 radial cut-planes. Use this information to:

- Compute the MA using $\boldsymbol{x_i}$ and the set of radial cut-planes, as described in sec. 3.3.2.
- Compute the leaflets 3D points cloud by finding their medial axis on each cut-plane, as described in sec. 3.3.3
- Compute the 3D mesh representation of the leaflets surface by triangulating the points cloud obtained previously.

As described in the previous approach, user intervention would be required only at the beginning of the process by defining a set of 9 initialization points (just as with the MA and ML segmentation in a single systolic frame). The remaining steps are completely automated and would allow the segmentation of the ML on each systolic frame in the 3DE dataset. Further improvements in the computational efficiency of the MA and ML would be required, since as mentioned in sec. 3.3.8, once initialized the algorithm, the required processing time is about 1 min, which implies that without taking into account the required time to propagate the initialization points to the remaining frames, using the current implementation and assuming at least 5 systolic frames (one of the lowest frame rates with current 3DTEE systems) a total processing time of at least 5 min would be needed to achieve full segmentation of the MA and ML during systole.

Another requirement is the adequate time resolution of the 3DE acquisition, so as to ensure that each of the initialization points to be tracked in two consecutive frames can be located in the region-of-search of the modified block-matching algorithm.

Chapter 9

Conclusions

The aim of this work was to provide a set of novel computational tools, capable of providing a more accurate quantitative assessment of the MV and requiring minimal user interaction. This has been accomplished through the development of algorithms that operate on 3DTTE and 3DTEE datasets, designed for the segmentation and quantification of the MA and ML during systole, including regional characterization, and a novel method for the quantification of the 3D ARO morphology.

In Chapters 3, 4 and 5, a semi-automatic algorithm for the segmentation of the MA and ML was presented and validated. After initialization of 9 user defined points, a completely automatic approach allows the construction of the annular contour and the extraction of the 3D representation of the ML; conventional morphological parameters as well as novel regional thickness, tenting and curvedness distributions were obtained. The validation stage, both in humans and animal specimens, showed the high accuracy of the algorithm as well as its high level of repeatability. The original contributions of this approach can be summarized as follows:

i. The quantification of MA and ML, including novel morphological parameters, is performed in approximately one fifth of the time required by conventional commercial software.
ii. Instead of a model-based approach [26], [29], [34], [28], [30], the quantification of MA and ML parameters was obtained directly from image features. The validation of the algorithm showed a more reliable estimation of these morphological parameters when compared with current state of the art approaches.
iii. The method overcomes previous approaches were leaflet thickness priors were incorporated and specific orientations of the MV within the 3DE dataset were required to achieve good segmentations[24], [23]. In our case the leaflet thickness, required for the enhancement of MA regions, is computed directly from the set of initialized cut planes, whereas the selection of an atrial point during initialization ensures that the MV can have any orientation within the 3D dataset.
iv. By computing the regional thickness, tenting and curvedness distributions, the proposed algorithm fully exploited the information contained in the 3DE datasets. This allowed to evidence differences between different normal and diseased populations, and shed new lights into the effects that some pathologies (such as dilative cardiomyopathy) or surgical procedures (such as mitral valve repair with annuloplasty) have on the morphology of the MV.

In chapters 6 and 7 a new method for the quantification of the 3D ARO was presented and preliminary validated. In this semi-automatic approach the user only had to select an initial threshold and one point near the regurgitant orifice; from this initialization a 3D mesh containing the regurgitant orifice was obtained, and a max-flow/min-cut graph segmentation approach allowed the automatic detection of the 3D

ARO contour an its morphological characterization, including the computation of the 3D surface area, its circularity and planarity. The original contributions of this work are listed below:

i. The method is capable of delineating the 3D ARO both in valves with functional mitral regurgitation or with degenerative MV disease. When compared with the approach of Chandra et al. [51], [112], it overcomes the need of a complete segmentation of the MA and ML before actually detecting the regurgitant orifice, a time-consuming and highly user dependent process. In our case a simple user-interaction step is required at the beginning of the segmentation, followed by a completely automated approach leading to the quantitative assessment of the ARO.
ii. By segmenting the void regions in the dataset, instead of the tissues, our algorithm is more versatile and is capable of segmenting orifices with different geometrical configurations, including overlapping leaflets in patients with MV prolapse. We consider that the method proposed by Chandra et al. [51], [112] cannot handle this type of orifices, thus limiting its clinical applicability.
iii. The proposed method overcomes all the manual and semiautomated approaches [63], [64], [52], [53] that rely in the color Doppler information and on geometric assumptions about the orifice shape in order to obtain an estimation of the orifice size. In our case we operate directly on the 3DE dataset, which makes the approach less user dependent, without requiring geometrical priors during the segmentation.
iv. The findings shown in Chapter 7, regarding the non-planarity and non-circularity of the ARO, put a big question mark on the current standard clinical approaches used for the assessment of mitral regurgitation, where the assumption of both planarity and circularity of the orifice is implied. As a consequence, we consider that current approaches may underestimate the real size of the orifice, which can lead to misdiagnosis of patients with these pathologies.

Nevertheless, it is also important to underline the fact that currently there is no "gold standard" to which our approach can be validated, which is the fundamental limitation of the proposed strategy. However, we consider that the proposed algorithm could provide a more reliable assessment of the severity of mitral regurgitation when compared with current approaches, such as 2D planimetry.

In Chapter 8 we discussed some future directions based on the developed computational tools. In particular we consider that the proposed algorithms for the quantitative assessment of the MA, ML and ARO would be versatile enough to be applied, with minor or no modifications, to the assessment of other cardiac valves, especially the aortic and tricuspid. This was in part confirmed by the quantitative analysis of a tricuspid valve TTE dataset, where a complete morphological characterization, including regional parameters, was achieved with essentially the same algorithm implemented for the segmentation of the MA and the ML. In this regard, we also consider that this algorithm could also be used for assessing the dynamics of the MV, by incorporating an optical flow based algorithm to allow the propagation of the initialization points to all the systolic frames in the dataset. Finally, although it has not been tested, we consider that the method for the morphological quantification of the ARO in MR can be extended *as is* to the assessment of aortic and tricuspid regurgitation, given that it relies on a generic shape that geometrically can be described as a 3D surface that contains an orifice connecting two cavities, a condition that is satisfied by any of the regurgitant configurations in the aortic or tricuspid valves.

Further applications to larger groups of different pathologies, as well as longitudinal studies, will further elucidate the clinical implications of the computed parameters with the developed new tools.

Bibliography

[1] V. T. Nkomo, J. M. Gardin, T. N. Skelton, J. S. Gottdiener, C. G. Scott, and M. Enriquez-Sarano, "Burden of valvular heart diseases: a population-based study," *The Lancet*, vol. 368, no. 9540, pp. 1005–1011, Sep. 2006.

[2] B. Iung, "A prospective survey of patients with valvular heart disease in Europe: The Euro Heart Survey on Valvular Heart Disease," *European Heart Journal Cardiovascular Imag*, vol. 24, no. 13, pp. 1231–1243, Jul. 2003.

[3] M. Enriquez-Sarano, C. W. Akins, and A. Vahanian, "Mitral regurgitation," *The Lancet*, vol. 373, no. 9672, pp. 1382–1394, Apr. 2009.

[4] R. M. Lang, V. Mor-Avi, L. Sugeng, P. S. Nieman, and D. J. Salm, "Three-dimensional echocardlography - The benefits of the additional dimension," *Journal of the American College of Cardiology*, vol. 48, no. 10, pp. 2053–2069, 2006.

[5] S. Chandra, L. Sugeng, and R. M. Lang, "Three-dimensional Echocardiography of the Mitral Valve Leaflet Anatomy and Repair," *Curr Cardiovasc Imaging Rep*, vol. 3, no. 5, pp. 268–275, Jul. 2010.

[6] R. A. Levine, M. O. Triulzi, P. Harrigan, and A. E. Weyman, "The relationship of mitral annular shape to the diagnosis of mitral valve prolapse," *Circulation*, vol. 75, no. 4, pp. 756–767, Apr. 1987.

[7] S. Chandra, I. S. Salgo, L. Sugeng, L. Weinert, W. Tsang, M. Takeuchi, K. T. Spencer, A. O'Connor, M. Cardinale, S. Settlemier, V. Mor-Avi, and R. M. Lang, "Characterization of degenerative mitral valve disease using morphologic analysis of real-time three-dimensional echocardiographic images: objective insight into complexity and planning of mitral valve repair," *Circulation: Cardiovascular Imaging*, vol. 4, no. 1, pp. 24–32, Jan. 2011.

[8] F. Veronesi, E. G. Caiani, L. Sugeng, L. Fusini, G. Tamborini, F. Alamanni, M. Pepi, and R. M. Lang, "Effect of mitral valve repair on mitral-aortic coupling: a real-time three-dimensional transesophageal echocardiography study," *Journal of the American Society of Echocardiography*, vol. 25, no. 5, pp. 524–531, May 2012.

[9] R. O. Bonow, B. A. Carabello, K. Chatterjee, A. C. de Leon Jr, D. P. Faxon, M. D. Freed, W. H. Gaasch, B. W. Lytle, R. A. Nishimura, P. T. O'Gara, R. A. O'Rourke, C. M. Otto, P. M. Shah, J. S. Shanewise, R. A. Nishimura, B. A. Carabello, D. P. Faxon, M. D. Freed, B. W. Lytle, P. T. O'Gara, R. A. O'Rourke, and P. M. Shah, "2008 Focused Update Incorporated Into the ACC/AHA 2006 Guidelines for the Management of Patients With Valvular Heart Disease," *Journal of the American College of Cardiology*, vol. 52, no. 13, pp. e1–e142, Sep. 2008.

[10] J. Grewal, S. Mankad, W. K. Freeman, R. L. Click, R. M. Suri, M. D. Abel, J. K. Oh, P. A. Pellikka, G. C. Nesbitt, I. Syed, S. L. Mulvagh, and F. A. Miller, "Real-time three-dimensional transesophageal echocardiography in the intraoperative assessment of mitral valve disease," *Journal of the American Society of Echocardiography*, vol. 22, no. 1, pp. 34–41, Jan. 2009.

[11] M. Pepi, G. Tamborini, A. Maltagliati, C. A. Galli, E. Sisillo, L. Salvi, M. Naliato, M. Porqueddu, A. Parolari, M. Zanobini, and F. Alamanni, "Head-to-Head comparison of two- and three-dimensional transthoracic and transesophageal echocardiography in the localization of mitral valve prolapse,"

Journal of the American College of Cardiology, vol. 48, no. 12, pp. 2524–2530, Dec. 2006.

[12] T. Szili-Torok and J. G. Bosch, "Transnasal transoesophageal ultrasound: the end of the intracardiac echocardiography age?," *Europace*, vol. 13, no. 1, pp. 7–8, Dec. 2010.

[13] D. Muraru, L. P. Badano, M. Vannan, and S. Iliceto, "Assessment of aortic valve complex by three-dimensional echocardiography: a framework for its effective application in clinical practice," *European Heart Journal - Cardiovascular Imaging*, vol. 13, no. 7, pp. 541–555, Apr. 2012.

[14] K. Otani, M. Takeuchi, K. Kaku, L. Sugeng, H. Yoshitani, N. Haruki, T. Ota, V. Mor-Avi, R. M. Lang, and Y. Otsuji, "Assessment of the Aortic Root Using Real-Time 3D Transesophageal Echocardiography," *Circ J*, vol. 74, no. 12, pp. 2649–2657, 2010.

[15] J. L. Gutierrez-Chico, J. L. Zamorano, E. Prieto-Moriche, R. A. Hernandez-Antolin, M. Bravo-Amaro, L. Perez de Isla, M. Sanmartin-Fernandez, J. A. Baz-Alonso, and A. Iniguez-Romo, "Real-time three-dimensional echocardiography in aortic stenosis: a novel, simple, and reliable method to improve accuracy in area calculation," *European Heart Journal Cardiovascular Imag*, vol. 29, no. 10, pp. 1296–1306, Dec. 2007.

[16] S. Goland, A. Trento, K. Iida, L. S. C. Czer, M. De Robertis, T. Z. Naqvi, K. Tolstrup, T. Akima, H. Luo, and R. J. Siegel, "Assessment of aortic stenosis by three-dimensional echocardiography: an accurate and novel approach," *Heart*, vol. 93, no. 7, pp. 801–807, Jul. 2007.

[17] T. T. Ton-Nu, "Geometric Determinants of Functional Tricuspid Regurgitation: Insights From 3-Dimensional Echocardiography," *Circulation*, vol. 114, no. 2, pp. 143–149, Jul. 2006.

[18] J. Kwan, G.-C. Kim, M.-J. Jeon, D.-H. Kim, T. Shiota, J. D. Thomas, K.-S. Park, and W.-H. Lee, "3D geometry of a normal tricuspid annulus during systole: a comparison study with the mitral annulus using real-time 3D echocardiography," *European Journal of Echocardiography : the journal of the Working Group on Echocardiography of the European Society of Cardiology*, vol. 8, no. 5, pp. 375–383, Oct. 2007.

[19] A. M. Anwar, M. L. Geleijnse, O. I. I. Soliman, J. S. McGhie, R. Frowijn, A. Nemes, A. E. Bosch, T. W. Galema, and F. J. ten Cate, "Assessment of normal tricuspid valve anatomy in adults by real-time three-dimensional echocardiography," *Int J Cardiovasc Imaging*, vol. 23, no. 6, pp. 717–724, Feb. 2007.

[20] *QLAB Quantification Software*. [Online]. Available: http://www.healthcare.philips.com/us_en/products/ultrasound/technologies/qlab/qlab_main.wpd. [Accessed: 22-May-2013].

[21] *Tomtec 4D MV-Assessment*. [Online]. Available: http://www.tomtec.de/end_users/4d_echo/4d_mv_assessmentc.html. [Accessed: 22-May-2013].

[22] Y. Wang, D. Vitanovski, B. Georgescu, R. I. Ionasec, I. Voigt, S. Datta, G. Funka-Lea, and D. Comaniciu, "Automatic Detection and Quantification of Mitral Regurgitation on TTE with Application to Assist Mitral Clip Planning and Evaluation." pp. 1–8, 06-Jul.-2012.

[23] A. M. Pouch, P. Yushkevich, B. M. Jackson, A. S. Jassar, M. Vergnat, J. H. Gorman, R. C. Gorman, and C. M. Sehgal, "Development of a semi-automated method for mitral valve modeling with medial axis representation using 3d ultrasound," *Medical Physics*, vol. 39, pp. 933–950, 2012.

[24] R. Schneider, D. Perrin, N. Vasilyev, G. Marx, P. del Nido, and R. Howe, "Mitral Annulus Segmentation From 3D Ultrasound Using Graph Cuts," *Medical*

Imaging, IEEE Transactions on, vol. 29, no. 9, pp. 1676–1687, 2010.

[25] R. Schneider, D. Perrin, and N. Vasilyev, "Mitral annulus segmentation from four-dimensional ultrasound using a valve state predictor and constrained optical flow," *Medical Image …*, 2011.

[26] I. Voigt, R. I. Ionasec, B. Georgescu, H. Houle, M. Huber, J. Hornegger, and D. Comaniciu, "Model-driven physiological assessment of the mitral valve from 4D TEE," presented at the SPIE Medical Imaging, 2009, pp. 72610R1–72610R11.

[27] R. Schneider, W. Burke, G. Marx, P. del Nido, and R. Howe, "Modeling mitral valve leaflets from three-dimensional ultrasound," *Functional Imaging and Modeling of the Heart*, pp. 215–222, 2011.

[28] R. Schneider, N. Tenenholtz, D. Perrin, and G. Marx, "Patient-specific mitral leaflet segmentation from 4D ultrasound," *... Image Computing and …*, 2011.

[29] P. Burlina, C. Sprouse, D. DeMenthon, A. Jorstad, R. Juang, F. Contijoch, T. Abraham, D. Yuh, and E. McVeigh, "Patient-specific modeling and analysis of the mitral valve using 3D-TEE," *Information Processing in Computer-Assisted Interventions*, pp. 135–146, 2010.

[30] T. Mansi, I. Voigt, E. Mengue, and R. Ionasec, "Towards patient-specific finite-element simulation of mitralclip procedure," *... Image Computing and …*, 2011.

[31] L. P. Ryan, B. M. Jackson, T. J. Eperjesi, T. J. Plappert, M. St John-Sutton, R. C. Gorman, and J. H. Gorman, "A methodology for assessing human mitral leaflet curvature using real-time 3-dimensional echocardiography," *J Thorac Cardiovasc Surg*, vol. 136, no. 3, pp. 726–734, Sep. 2008.

[32] E. Votta, A. Arnoldi, A. Invernizzi, R. Ponzini, F. Veronesi, G. Tamborini, M. Pepi, F. Alamanni, A. Redaelli, and E. Caiani, "Mitral valve patient-specific finite element modeling from 3-D real time echocardiography: a potential new tool for surgical planning," *Proceedings CI2BM09 - MICCAI Workshop on Cardiovascular Interventional Imaging and Biophysical Modelling*, pp. 1–9, Oct. 2009.

[33] F. Veronesi, C. Corsi, L. Sugeng, V. Mor-Avi, E. G. Caiani, L. Weinert, C. Lamberti, and R. M. Lang, "A study of functional anatomy of aortic-mitral valve coupling using 3D matrix transesophageal echocardiography," *Circulation: Cardiovascular Imaging*, vol. 2, no. 1, pp. 24–31, 2009.

[34] R. I. Ionasec, I. Voigt, B. Georgescu, Yang Wang, H. Houle, F. Vega-Higuera, N. Navab, and D. Comaniciu, "Patient-Specific Modeling and Quantification of the Aortic and Mitral Valves From 4-D Cardiac CT and TEE," *Ieee T Med Imaging*, vol. 29, no. 9, pp. 1636–1651.

[35] M. Chaput, M. D. Handschumacher, F. Tournoux, L. Hua, J. L. Guerrero, G. J. Vlahakes, and R. A. Levine, "Mitral leaflet adaptation to ventricular remodeling," *Circulation*, vol. 118, no. 8, pp. 845–852, Aug. 2008.

[36] M. Chaput, M. D. Handschumacher, J. L. Guerrero, G. Holmvang, J. P. Dal-Bianco, S. Sullivan, G. J. Vlahakes, J. Hung, R. A. Levine, and Leducq Foundation MITRAL Transatlantic Network, "Mitral leaflet adaptation to ventricular remodeling: prospective changes in a model of ischemic mitral regurgitation," *Circulation*, vol. 120, no. 11, pp. S99–103, Sep. 2009.

[37] J. P. Dal-Bianco, E. Aikawa, J. Bischoff, J. L. Guerrero, M. D. Handschumacher, S. Sullivan, B. Johnson, J. S. Titus, Y. Iwamoto, J. Wylie-Sears, R. A. Levine, and A. Carpentier, "Active adaptation of the tethered mitral valve: insights into a compensatory mechanism for functional mitral regurgitation," *Circulation*, vol. 120, no. 4, pp. 334–342, Jul. 2009.

[38] K. J. Grande-Allen, "Glycosaminoglycans and proteoglycans in normal mitral valve leaflets and chordae: association with regions of tensile and compressive loading," *Glycobiology*, vol. 14, no. 7, pp. 621–633, Apr. 2004.

[39] K. J. Grande-Allen, A. G. Borowski, R. W. Troughton, P. L. Houghtaling, N. R.

DiPaola, C. S. Moravec, I. Vesely, and B. P. Griffin, “Apparently normal mitral valves in patients with heart failure demonstrate biochemical and structural derangements,” *Journal of the American College of Cardiology*, vol. 45, no. 1, pp. 54–61, Jan. 2005.

[40] J.-P. E. Kvitting, W. Bothe, S. Göktepe, M. K. Rausch, J. C. Swanson, E. Kuhl, N. B. Ingels, and D. C. Miller, “Anterior mitral leaflet curvature during the cardiac cycle in the normal ovine heart,” *Circulation*, vol. 122, no. 17, pp. 1683–1689, Oct. 2010.

[41] J. Kwan, “Geometric Differences of the Mitral Apparatus Between Ischemic and Dilated Cardiomyopathy With Significant Mitral Regurgitation: Real-Time Three-Dimensional Echocardiography Study,” *Circulation*, vol. 107, no. 8, pp. 1135–1140, Feb. 2003.

[42] A. P. W. Lee, M. Acker, S. H. Kubo, S. F. Bolling, S. W. Park, C. J. Bruce, and J. K. Oh, “Mechanisms of Recurrent Functional Mitral Regurgitation After Mitral Valve Repair in Nonischemic Dilated Cardiomyopathy: Importance of Distal Anterior Leaflet Tethering,” *Circulation*, vol. 119, no. 19, pp. 2606–2614, May 2009.

[43] L. Ryan, B. Jackson, L. Parish, H. Sakamoto, T. Plappert, M. S. J. Sutton, J. Gorman III, and R. Gorman, “Quantification and localization of mitral valve tenting in ischemic mitral regurgitation using real-time three-dimensional echocardiography☆,” *European Journal of Cardio-Thoracic Surgery*, vol. 31, no. 5, pp. 839–844, May 2007.

[44] L. P. Ryan, B. M. Jackson, L. M. Parish, H. Sakamoto, T. J. Plappert, M. St John-Sutton, J. H. Gorman, and R. C. Gorman, “Mitral valve tenting index for assessment of subvalvular remodeling,” *The Annals of Thoracic Surgery*, vol. 84, no. 4, pp. 1243–1249, Oct. 2007.

[45] J.-M. Song, S. Fukuda, T. Kihara, M.-S. Shin, M. J. Garcia, J. D. Thomas, and T. Shiota, “Value of mitral valve tenting volume determined by real-time three-dimensional echocardiography in patients with functional mitral regurgitation,” *The American Journal of Cardiology*, vol. 98, no. 8, pp. 1088–1093, Oct. 2006.

[46] E. H. Stephens, T. A. Timek, G. T. Daughters, J. J. Kuo, A. M. Patton, L. S. Baggett, N. B. Ingels, D. C. Miller, and K. J. Grande-Allen, “Significant changes in mitral valve leaflet matrix composition and turnover with tachycardia-induced cardiomyopathy,” *Circulation*, vol. 120, no. 11, pp. S112–9, Sep. 2009.

[47] E. H. Stephens, T. C. Nguyen, A. Itoh, N. B. Ingels, D. C. Miller, and K. J. Grande-Allen, “The effects of mitral regurgitation alone are sufficient for leaflet remodeling,” *Circulation*, vol. 118, no. 14, pp. S243–9, Sep. 2008.

[48] S. Biner, A. Rafique, F. Rafii, K. Tolstrup, O. Noorani, T. Shiota, S. Gurudevan, and R. J. Siegel, “Reproducibility of Proximal Isovelocity Surface Area, Vena Contracta, and Regurgitant Jet Area for Assessment of Mitral Regurgitation Severity,” *JACC Cardiovasc Imaging*, vol. 3, no. 3, pp. 235–243, Mar. 2010.

[49] A. Lange, P. Palka, E. Donnelly, and D. Burstow, “Quantification of mitral regurgitation orifice area by 3-dimensional echocardiography: comparison with effective regurgitant orifice area by PISA method and proximal regurgitant jet diameter,” *International Journal of Cardiology*, vol. 86, pp. 87–98, Sep. 2002.

[50] Y. Matsumura, S. Fukuda, H. Tran, N. L. Greenberg, D. A. Agler, N. Wada, M. Toyono, J. D. Thomas, and T. Shiota, “Geometry of the proximal isovelocity surface area in mitral regurgitation by 3-dimensional color Doppler echocardiography: difference between functional mitral regurgitation and prolapse regurgitation,” *Am Heart J*, vol. 155, no. 2, pp. 231–238, Feb. 2008.

[51] S. Chandra, L. Weinert, L. Sugeng, I. S. Salgo, S. Settlemier, J. X. Shen, V. Mor-Avi, and R. Lang, “Volumetric Measurement of the Anatomic Regurgitant Orifice Area in Mitral Regurgitation: Comparison with Two-Dimensional Flow

Convergence Analysis," *Computers in Cardiology*, vol. 36, pp. 769–772, Oct. 2009.

[52] L. Grady, S. Datta, O. Kutter, and C. Duong, "Regurgitation quantification using 3D PISA in volume echocardiography," *Medical Image Computing and Computer-Assisted Intervention—MICCAI 2011*, no. III, pp. 512–519, 2011.

[53] M. Moraldo, C. Bergamini, A. S. N. Malaweera, N. M. Dhutia, P. A. Pabari, K. Willson, R. Baruah, C. Manisty, J. E. Davies, X. Y. Xu, A. D. Hughes, and D. P. Francis, "A novel fully automated method for mitral regurgitant orifice area quantification," *International Journal of Cardiology*, vol. 166, no. 3, pp. 688–695, Jul. 2013.

[54] S. Buchner, K. Debl, F. Poschenrieder, S. Feuerbach, G. A. J. Riegger, A. Luchner, and B. Djavidani, "Cardiovascular Magnetic Resonance for Direct Assessment of Anatomic Regurgitant Orifice in Mitral Regurgitation," *Circulation: Cardiovascular Imaging*, vol. 1, no. 2, pp. 148–155, Sep. 2008.

[55] H. Muresian, "The clinical anatomy of the mitral valve," *Clinical Anatomy*, vol. 22, no. 1, pp. 85–98, Dec. 2009.

[56] R. Lang, W. Tsang, L. Weinert, V. Mor-Avi, and S. Chandra, "Valvular Heart Disease," *Journal of the American College of Cardiology*, vol. 58, no. 19, pp. 1933–1944, Nov. 2011.

[57] P. O'Gara, L. Sugeng, R. Lang, M. Sarano, J. Hung, S. Raman, G. Fischer, B. Carabello, D. Adams, and M. Vannan, "The Role of Imaging in Chronic Degenerative Mitral Regurgitation," *JACC Cardiovasc Imaging*, vol. 1, no. 2, pp. 221–237, Mar. 2008.

[58] J. P. Sutton III, S. Y. Ho, and R. H. Anderson, "The forgotten interleaflet triangles: A review of the surgical anatomy of the aortic valve," *The Annals of Thoracic Surgery*, vol. 59, no. 2, pp. 419–427, Feb. 1995.

[59] N. Piazza, P. de Jaegere, C. Schultz, A. E. Becker, P. W. Serruys, and R. H. Anderson, "Anatomy of the Aortic Valvar Complex and Its Implications for Transcatheter Implantation of the Aortic Valve," *Circulation: Cardiovascular Interventions*, vol. 1, no. 1, pp. 74–81, Aug. 2008.

[60] F. Aguilar, H. Joachim Nesser, F. Faletra, S. De Castro, M. Maron, A. Patel, and N. Pandian, "Imaging modalities in valvular heart disease," *Current Cardiology Reports*, vol. 10, no. 2, pp. 98–103, 2008.

[61] G. Valocik, O. Kamp, and C. A. Visser, "Three-dimensional echocardiography in mitral valve disease," *European Journal of Echocardiography : the journal of the Working Group on Echocardiography of the European Society of Cardiology*, vol. 6, no. 6, pp. 443–454, Dec. 2005.

[62] W. A. Zoghbi, M. Enriquez-Sarano, E. Foster, P. Grayburn, C. Kraft, R. A. Levine, P. Nihoyannopoulos, C. M. Otto, M. A. Quinones, H. Rakowski, W. J. Stewart, A. Waggoner, and N. J. Weissman, "Recommendations for evaluation of the severity of native valvular regurgitation with two-dimensional and doppler echocardiography," *Journal of the American Society of Echocardiography*, vol. 16, no. 7, pp. 777–802, Jul. 2003.

[63] C. Yosefy, J. Hung, S. Chua, M. Vaturi, T.-T. Ton-Nu, M. D. Handschumacher, and R. A. Levine, "Direct Measurement of Vena Contracta Area by Real-Time 3-Dimensional Echocardiography for Assessing Severity of Mitral Regurgitation," *The American Journal of Cardiology*, vol. 104, no. 7, pp. 978–983, Oct. 2009.

[64] M. Shanks, H. M. J. Siebelink, V. Delgado, N. R. L. van de Veire, A. C. T. Ng, A. Sieders, J. D. Schuijf, H. J. Lamb, N. Ajmone Marsan, J. J. M. Westenberg, L. J. Kroft, A. de Roos, and J. J. Bax, "Quantitative Assessment of Mitral Regurgitation: Comparison Between Three-Dimensional Transesophageal Echocardiography and Magnetic Resonance Imaging," *Circulation: Cardiovascular Imaging*, vol. 3, no. 6, pp. 694–700, Nov. 2010.

[65] S. Golemati, A. Sassano, M. J. Lever, A. A. Bharath, S. Dhanjil, and A. N. Nicolaides, “Carotid artery wall motion estimated from B-mode ultrasound using region tracking and block matching,” *Ultrasound in Medicine and Biology*, vol. 29, no. 3, pp. 387–399, Mar. 2003.

[66] A. Amini, T. Weymouth, and R. C. Jain, “Using dynamic programming for solving variational problems in vision,” *Pattern Analysis and Machine Intelligence, IEEE Transactions on*, vol. 12, no. 9, pp. 855–867, 1990.

[67] E. W. Dijkstra, “A note on two problems in connexion with graphs,” *Numerische Mathematik*, vol. 1, no. 1, pp. 269–271, Oct. 1959.

[68] M. Van Stralen, J. Bosch, M. Voormolen, G. van Burken, B. Krenning, R. van Geuns, C. Lancee, N. De Jong, and J. Reiber, “Left ventricular volume estimation in cardiac three-dimensional ultrasound: A semiautomatic border detection approach,” *Acad Radiol*, vol. 12, no. 10, pp. 1241–1249, 2005.

[69] Cormen and E. Al, “Introduction to Algorithms, 3/e,” 2010.

[70] L. R. Ford and D. R. Fulkerson, *Flows in Networks*. Princeton University Press, 2010.

[71] Y. Boykov and V. Kolmogorov, “An experimental comparison of min-cut/max-flow algorithms for energy minimization in vision,” *Energy minimization methods in computer vision and pattern recognition*, pp. 359–374, 2001.

[72] S. C. Zhu and A. Yuille, “Region Competition: Unifying Snakes, Region Growing and Bayes/MDL for Multiband Image Segmentation,” *IEEE Transactions on Pattern Analysis and Machine Intelligence*, vol. 18, no. 9, pp. 884–900, Mar. 1996.

[73] P. Yushkevich, J. Piven, H. Hazlett, R. Smith, S. Ho, J. Gee, and G. Gerig, “User-guided 3D active contour segmentation of anatomical structures: significantly improved efficiency and reliability,” *NeuroImage*, vol. 31, no. 3, pp. 1116–1128, 2006.

[74] S. Osher and R. Fedkiw, *Level set methods and dynamic implicit surfaces*, vol. 153. 2003.

[75] W. E. Lorensen and H. E. Cline, “Marching cubes: a high resolution 3D surface construction algorithm,” *Computer Graphics*, vol. 21, no. 4, pp. 163–169, Jul. 1987.

[76] P. Schneider and D. Eberly, *Geometric tools for computer graphics*. 2003.

[77] J. R. Shewchuk, “Mesh generation for domains with small angles,” presented at the Proceedings of the sixteenth annual symposium on Computational Geometry, 2000, pp. 1–10.

[78] M. Botsch, L. Kobbelt, M. Pauly, P. Alliez, and B. Lévy, “Polygon mesh processing,” 2010.

[79] A. McIvor and R. Valkenburg, “A comparison of local surface geometry estimation methods,” *Machine Vision and Applications*, vol. 10, no. 1, pp. 17–26, 1997.

[80] M. Vieira and K. Shimada, “Surface mesh segmentation and smooth surface extraction through region growing,” *Computer aided geometric design*, vol. 22, no. 8, pp. 771–792, 2005.

[81] J. Koenderink and A. van Doorn, “Surface shape and curvature scales,” *Image and Vision Computing*, vol. 10, no. 8, pp. 557–564, Apr. 1992.

[82] L. Chen and N. D. Georganas, “An efficient and robust algorithm for 3D mesh segmentation,” *Multimed Tools Appl*, vol. 29, no. 2, pp. 109–125, Jun. 2006.

[83] L. Shapira, A. Shamir, and D. Cohen-Or, “Consistent mesh partitioning and skeletonisation using the shape diameter function,” *Visual Comput*, vol. 24, no. 4, pp. 249–259, Jan. 2008.

[84] E. Zhang and K. Mischaikow, “Feature-Based Surface Parameterization and Texture Mapping,” *ACM Transactions On Graphics*, vol. 24, no. 1, pp. 1–27, Jan.

2005.
[85] K. R. Khabbaz, F. Mahmood, O. Shakil, H. J. Warraich, J. H. Gorman, R. C. Gorman, R. Matyal, P. Panzica, and P. E. Hess, "Dynamic 3-dimensional echocardiographic assessment of mitral annular geometry in patients with functional mitral regurgitation," *The Annals of Thoracic Surgery*, pp. 1–6, Oct. 2012.
[86] N. Otsu, "A Threshold Selection Method from Gray-Level Histograms," *IEEE Transactions on Systems, Man and Cybernetics*, vol. 9, no. 1, pp. 62–66, Jan. 1979.
[87] K.-S. Chuang, H.-L. Tzeng, S. Chen, J. Wu, and T.-J. Chen, "Fuzzy c-means clustering with spatial information for image segmentation," *Computerized Medical Imaging and Graphics*, vol. 30, no. 1, pp. 9–15, Jan. 2006.
[88] G. Taubin, T. Zhang, and G. Golub, *Optimal surface smoothing as filter design*. Springer, 1996.
[89] P. Karasev, J. Malcolm, M. Niethammer, R. Kikinis, and A. Tannenbaum, "User-driven 3D mesh region targeting," *Society of Photo-Optical Instrumentation Engineers (SPIE) Conference Series*, vol. 7625, p. 37, 2010.
[90] A. Frangi, W. Niessen, K. Vincken, and M. Viergever, "Multiscale vessel enhancement filtering," *Medical Image Computing and Computer-Assisted Interventation—MICCAI'98*, pp. 130–137, 1998.
[91] L. N. Bohs and G. E. Trahey, "A novel method for angle independent ultrasonic imaging of blood flow and tissue motion," *Biomedical Engineering, IEEE Transactions on*, vol. 38, no. 3, pp. 280–286, Apr. 1991.
[92] S. T. Nevo, M. van Stralen, A. M. Vossepoel, J. H. C. Reiber, N. de Jong, A. F. W. van der Steen, and J. G. Bosch, "Automated tracking of the mitral valve annulus motion in apical echocardiographic images using multidimensional dynamic programming," *Ultrasound in Medicine and Biology*, vol. 33, no. 9, pp. 1389–1399, Sep. 2007.
[93] F. Maffessanti, R. M. Lang, J. Niel, R. Steringer-Mascherbauer, E. G. Caiani, H.-J. Nesser, and V. Mor-Avi, "Three-dimensional analysis of regional left ventricular endocardial curvature from cardiac magnetic resonance images," *Magn Reson Imaging*, vol. 29, no. 4, pp. 516–524, May 2011.
[94] *VTK - Visualization Toolkit*. [Online]. Available: http://www.vtk.org/. [Accessed: 30-May-2013].
[95] *Qt Project*. [Online]. Available: http://qt-project.org/. [Accessed: 30-May-2013].
[96] *Matlab: the language of technical computing*. [Online]. Available: http://www.mathworks.com/products/matlab/. [Accessed: 30-May-2013].
[97] A. Argento, "Validazione di un software per la misura di dimensioni anatomiche di valvole mitrali tramite esperimenti su campioni porcini espiantati," Politecnico di Milano, Scuola di Ingegneria dei Sistemi - Corso di Laurea Magistrale in Ingegneria Biomedica, 2012.
[98] A. M. Leopaldi, R. Vismara, M. Lemma, L. Valerio, M. Cervo, A. Mangini, M. Contino, A. Redaelli, C. Antona, and G. B. Fiore, "In vitro hemodynamics and valve imaging in passive beating hearts," *Journal of Biomechanics*, vol. 45, no. 7, pp. 1133–1139, Apr. 2012.
[99] F. Maffessanti, N. A. Marsan, G. Tamborini, L. Sugeng, E. G. Caiani, P. Gripari, F. Alamanni, V. Jeevanandam, R. M. Lang, and M. Pepi, "Quantitative analysis of mitral valve apparatus in mitral valve prolapse before and after annuloplasty: a three-dimensional intraoperative transesophageal study," *Journal of the American Society of Echocardiography*, vol. 24, no. 4, pp. 405–413, Apr. 2011.
[100] M. Vergnat, A. S. Jassar, B. M. Jackson, L. P. Ryan, T. J. Eperjesi, A. M. Pouch, S. J. Weiss, A. T. Cheung, M. A. Acker, J. H. Gorman, and R. C. Gorman, "Ischemic mitral regurgitation: a quantitative three-dimensional

echocardiographic analysis," *The Annals of Thoracic Surgery*, vol. 91, no. 1, pp. 157–164, 2011.

[101] J. Grewal, R. Suri, S. Mankad, A. Tanaka, D. W. Mahoney, H. V. Schaff, F. A. Miller, and M. Enriquez-Sarano, "Mitral annular dynamics in myxomatous valve disease: new insights with real-time 3-dimensional echocardiography," *Circulation*, vol. 121, no. 12, pp. 1423–1431, Mar. 2010.

[102] I. S. Salgo, J. H. Gorman, R. C. Gorman, B. M. Jackson, F. W. Bowen, T. Plappert, M. G. St John Sutton, and L. H. Edmunds, "Effect of annular shape on leaflet curvature in reducing mitral leaflet stress," *Circulation*, vol. 106, no. 6, pp. 711–717, Aug. 2002.

[103] S. Nielsen, H. Nigaard, A. A. Fontaine, J. M. Hasenkam, S. He, and A. P. Yoganathan, "Papillary muscle misalignment causes multiple mitral regurgitant jets: an ambiguous mechanism for functional mitral regurgitation," *The Journal of heart valve disease*, vol. 8, no. 5, pp. 551–564, Apr. 1999.

[104] G. T. Wilkins, A. E. Weyman, V. M. Abascal, P. C. Block, and I. F. Palacios, "Percutaneous balloon dilatation of the mitral valve: an analysis of echocardiographic variables related to outcome and the mechanism of dilatation," *British Heart Journal*, vol. 60, no. 4, pp. 299–308, Nov. 1988.

[105] P. Lancellotti, L. Moura, L. A. Pierard, E. Agricola, B. A. Popescu, C. Tribouilloy, A. Hagendorff, J. L. Monin, L. Badano, J. L. Zamorano, on behalf of the European Association of Echocardiography, Document Reviewers:, R. Sicari, A. Vahanian, and J. R. T. C. Roelandt, "European Association of Echocardiography recommendations for the assessment of valvular regurgitation. Part 2: mitral and tricuspid regurgitation (native valve disease)," *European Journal of Echocardiography : the journal of the Working Group on Echocardiography of the European Society of Cardiology*, vol. 11, no. 4, pp. 307–332, Apr. 2010.

[106] S. H. Little, B. Pirat, R. Kumar, S. R. Igo, M. McCulloch, C. J. Hartley, J. Xu, and W. A. Zoghbi, "Three-dimensional color Doppler echocardiography for direct measurement of vena contracta area in mitral regurgitation: in vitro validation and clinical experience," *JACC Cardiovasc Imaging*, vol. 1, no. 6, pp. 695–704, Nov. 2008.

[107] S. H. Little, "The Vena Contracta Area," *JCMG*, vol. 5, no. 7, pp. 677–680, Jul. 2012.

[108] S. H. Little, S. R. Igo, B. Pirat, M. McCulloch, C. J. Hartley, Y. Nosé, and W. A. Zoghbi, "In Vitro Validation of Real-Time Three-Dimensional Color Doppler Echocardiography for Direct Measurement of Proximal Isovelocity Surface Area in Mitral Regurgitation," *The American Journal of Cardiology*, vol. 99, no. 10, pp. 1440–1447, May 2007.

[109] X. Zeng, R. A. Levine, L. Hua, E. L. Morris, Y. Kang, M. Flaherty, N. V. Morgan, and J. Hung, "Diagnostic Value of Vena Contracta Area in the Quantification of Mitral Regurgitation Severity by Color Doppler 3D Echocardiography," *Circulation: Cardiovascular Imaging*, vol. 4, no. 5, pp. 506–513, Sep. 2011.

[110] P. T. P. C. D. T. D. F. H. Marwick, "Quantitative Assessment of Mitral Regurgitation," *JCMG*, vol. 5, no. 11, pp. 1161–1175, Nov. 2012.

[111] P. A. Grayburn, "The Importance of Regurgitant Orifice Shape in Mitral Regurgitation∗ ∗ Editorials published in JACC: Cardiovascular Imaging reflect the views of the authors and do not necessarily represent the views of JACC: Cardiovascular Imaging or the American College of Cardiology.," *JCMG*, vol. 4, no. 10, pp. 1097–1099, Oct. 2011.

[112] S. Chandra, I. S. Salgo, L. Sugeng, L. Weinert, S. H. Settlemier, V. Mor-Avi, and

R. M. Lang, “A three-dimensional insight into the complexity of flow convergence in mitral regurgitation: adjunctive benefit of anatomic regurgitant orifice area,” *AJP: Heart and Circulatory Physiology*, vol. 301, no. 3, pp. H1015–H1024, Aug. 2011.

[113] H. Zhang, Y. Jiao, Y. Zhang, and K. Shimada, “Automated Segmentation of Cerebral Aneurysms Based on Conditional Random Field and Gentle Adaboost,” *Lecture Notes in Computer Science*, vol. 7599, pp. 59–59, Aug. 2012.

[114] S. Baloch, E. Cheng, Y. Zhu, A. Mohamed, H. Ling, and T. Fang, “Shape Based Conditional Random Fields for Segmenting Intracranial Aneurysms,” *Proceedings of the MICCAI Workshop on Mesh Processing in Medical Image Analysis*, pp. 39–50, Aug. 2011.

[115] J. Zhang, C. Wu, J. Cai, J. Zheng, and X. Tai, “Mesh snapping: Robust interactive mesh cutting using fast geodesic curvature flow,” *Computer Graphics Forum*, vol. 29, no. 2, pp. 517–526, 2010.

[116] S. Katz, G. Leifman, and A. Tal, “Mesh segmentation using feature point and core extraction,” *Visual Comput*, vol. 21, no. 8, pp. 649–658, Sep. 2005.

[117] F. Bookstein, “Principal Warps: Thin-Plate Splines and the Decomposition of Deformations,” *IEEE Transactions on Pattern Analysis and Machine Intelligence*, vol. 11, no. 6, pp. 567–585, Jun. 1989.

[118] *iGraph*. [Online]. Available: http://igraph.sourceforge.net/. [Accessed: 13-Jun.-2013].

[119] *ImageJ*. [Online]. Available: http://rsbweb.nih.gov/ij/. [Accessed: 13-Jun.-2013].

[120] Y. Lee and S. Lee, “Geometric Snakes for Triangular Meshes,” *Computer Graphics Forum (Eurographics)*, vol. 21, no. 3, pp. 229–238, Aug. 2002.

[121] Y. Lee, S. Lee, A. Shamir, D. Cohen-Or, and H. Seidel, “Intelligent mesh scissoring using 3d snakes,” 2004.

[122] F. Maffessanti, P. Gripari, G. Pontone, D. Andreini, E. Bertella, S. Mushtaq, G. Tamborini, L. Fusini, M. Pepi, and E. G. Caiani, “Three-dimensional dynamic assessment of tricuspid and mitral annuli using cardiovascular magnetic resonance,” *European Heart Journal - Cardiovascular Imaging*, Jan. 2013.

[123] R. Sukmawan, N. Watanabe, Y. Ogasawara, Y. Yamaura, K. Yamamoto, N. Wada, T. Kume, H. Okura, and K. Yoshida, “Geometric changes of tricuspid valve tenting in tricuspid regurgitation secondary to pulmonary hypertension quantified by novel system with transthoracic real-time 3-dimensional echocardiography”, *Journal of the American Society of Echocardiography*, vol. 20, no. 5, pp. 470–476, Jun. 2007.

[124] L. P. Badano, E. Agricola, L. P. de Isla, P. Gianfagna, and J. L. Zamorano, “Evaluation of the tricuspid valve morphology and function by transthoracic real-time three-dimensional echocardiography,” *European Journal of Echocardiography : the journal of the Working Group on Echocardiography of the European Society of Cardiology*, vol. 10, no. 4, pp. 477–484, May 2009.

[125] H. Baumgartner, J. Hung, J. Bermejo, J. B. Chambers, A. Evangelista, B. P. Griffin, B. Iung, C. M. Otto, P. A. Pellikka, and M. Quinones, “Echocardiographic assessment of valve stenosis: EAE/ASE recommendations for clinical practice,” *European Journal of Echocardiography : the journal of the Working Group on Echocardiography of the European Society of Cardiology*, vol. 10, no. 1, pp. 1–25, Jan. 2009.

[126] A. Vahanian, O. Alfieri, F. Andreotti, M. J. Antunes, G. Baron-Esquivias, H. Baumgartner, M. A. Borger, T. P. Carrel, M. De Bonis, A. Evangelista, V. Falk, B. Iung, P. Lancellotti, L. Pierard, S. Price, H. J. Schafers, G. Schuler, J. Stepinska, K. Swedberg, J. Takkenberg, U. O. Von Oppell, S. Windecker, J. L. Zamorano, M. Zembala, ESC Committee for Practice Guidelines (CPG), J. J. Bax, H. Baumgartner, C. Ceconi, V. Dean, C. Deaton, R. Fagard, C. Funck-

Brentano, D. Hasdai, A. Hoes, P. Kirchhof, J. Knuuti, P. Kolh, T. McDonagh, C. Moulin, B. A. Popescu, Z. Reiner, U. Sechtem, P. A. Sirnes, M. Tendera, A. Torbicki, A. Vahanian, S. Windecker, Document Reviewers:, B. A. Popescu, L. Von Segesser, L. P. Badano, M. Bunc, M. J. Claeys, N. Drinkovic, G. Filippatos, G. Habib, A. P. Kappetein, R. Kassab, G. Y. H. Lip, N. Moat, G. Nickenig, C. M. Otto, J. Pepper, N. Piazza, P. G. Pieper, R. Rosenhek, N. Shuka, E. Schwammenthal, J. Schwitter, P. T. Mas, P. T. Trindade, and T. Walther, "Guidelines on the management of valvular heart disease (version 2012): The Joint Task Force on the Management of Valvular Heart Disease of the European Society of Cardiology (ESC) and the European Association for Cardio-Thoracic Surgery (EACTS)," *European Heart Journal Cardiovascular Imag*, vol. 33, no. 19, pp. 2451–2496, Oct. 2012.

[127] D. Velayudhan, T. Brown, N. Nanda, V. Patel, A. Miller, F. Mehmood, S. Rajdev, L. Fang, E. Frans, S. Vengala, P. Madadi, P. Yelamanchili, and O. Baysan, "Quantification of tricuspid regurgitation by live three-dimensional trans- thoracic echocardiographic measurements of vena contracta area," *Echocardiography-A Journal Of Cardiovascular Ultrasound And Allied Techniques*, vol. 23, no. 9, pp. 793–800, Sep. 2006.

[128] J.-M. Song, M.-K. Jang, Y.-S. Choi, Y. J. Kim, S.-Y. Min, D.-H. Kim, D.-H. Kang, and J.-K. Song, "The Vena Contracta in Functional Tricuspid Regurgitation: A Real-Time Three-Dimensional Color Doppler Echocardiography Study," *Journal of the American Society of Echocardiography*, vol. 24, no. 6, pp. 663–670, Apr. 2011.

[129] Y. Mori, T. SHIOTA, M. Jones, S. Wanitkun, T. Irvine, X. Li, A. Delabays, N. G. Pandian, and D. J. Sahn, "Three-Dimensional Reconstruction of the Color Doppler Imaged Vena Contracta for Quantifying Aortic Regurgitation : Studies in a Chronic Animal Model," *Circulation*, vol. 99, no. 12, pp. 1611–1617, Mar. 1999.

[130] P. Lancellotti, C. Tribouilloy, A. Hagendorff, L. Moura, B. A. Popescu, E. Agricola, J. L. Monin, L. A. Pierard, L. Badano, J. L. Zamorano, on behalf of the European Association of Echocardiography, Document Reviewers:, R. Sicari, A. Vahanian, and J. R. T. C. Roelandt, "European Association of Echocardiography recommendations for the assessment of valvular regurgitation. Part 1: aortic and pulmonary regurgitation (native valve disease)," *European Journal of Echocardiography : the journal of the Working Group on Echocardiography of the European Society of Cardiology*, vol. 11, no. 3, pp. 223–244, Apr. 2010.